Solidification Behaviour of Al-Sn-Cu Immiscible Alloys and Al-Si Cast Alloys Processed under Intensive Shearing

By

Hiren R. Kotadia

BCAST (Brunel Centre for Advanced Solidification Technology),

Brunel University, Uxbridge, UB8 3PH, UK

A thesis submitted for the degree of

Doctor of Philosophy

at the Brunel University

January 2010

This thesis is dedicated to

my grandmother and parents

for their love, endless support and encouragement.

"Once you start working on something, don't be afraid of failure and don't abandon it. People who work sincerely are the happiest."

-Chanakya quotes (Indian politician, strategist and writer, 350 BC-275)

Abstract

Alloy castings are usually solidified with a coarse columnar grain structure under normal casting conditions unless the mode of the solidification is carefully controlled. It is desirable for the grain structure to be fine and equiaxed to improve their mechanical performance as finished castings. It is possible to develop a fine and equiaxed grain structure either by increasing the number of nucleation sites or by grain multiplication. Immiscible alloys with a microstructure in which a soft phase is dispersed homogeneously in a hard matrix have significant potential applications in advanced bearing systems, especially for the automotive industry.

Despite considerable efforts made worldwide, including extensive space experiments, no casting techniques so far can produce the desired immiscible microstructure of alloys. Experimental results on Al-Sn-Cu immiscible alloys have confirmed that intensive shearing using melt conditioning by an advanced shearing technology (MCAST) unit, is an effective way to achieve a fine and uniform dispersion of the soft phase without macro-demixing, and that such a dispersed microstructure can be further refined in alloys with precipitation of the primary Al phase prior to the demixing reaction. In addition, it was found that melt shearing at 200 rpm for 60 s will be adequate to produce a fine and uniform dispersion of the Sn phase, and that a higher shearing speed and prolonged shearing time can only achieve further minor refinement.

A study of Al-Si hypoeutectic and hypereutectic alloys presents the effects of the processing temperature and intensive shearing on the microstructural and mechanical properties which have been investigated systematically. Attempts have been made to explain the solidification mechanism with intensive melt shearing. The sheared melt was cast into tensile test samples by high pressure die caster (HPDC) to examine the microstructures and mechanical properties. The experimental results reveal that significant grain refinement and uniformity of grains was achieved by the intensive shearing and also a considerable increase in mechanical properties with pouring temperature by changing intermetallic particles morphology, the position of defect band and reduced microscopic defects.

Preface

This thesis is a description of work that I performed in the Brunel Centre for Advanced Solidification Technology, Brunel University, West London from 13th May 2006 to 30th April 2009. To the best of my knowledge, this work is original, except where suitable references are made to previous work. Neither this, nor any substantially similar dissertation has been submitted to any other institution. It is the result of my own work and includes a thermodynamic calculation that is the outcome of collaboration. The content of the dissertation does not exceed 60,000 words.

Related Publications

International Journal Papers

- Kotadia HR, Patel JB, Fan Z, Doernberg E, Schmid-Fetzer R.: "Processing of Al-45Sn-10Cu Based Immiscible Alloy by a Rheomixing Process", *Solid State Pheno.*, 2008, 141-143: 529.
- Kotadia HR, Doernberg E, Patel JB, Fan Z, Schmid-Fetzer R.: "Solidification of Al-Sn-Cu based immiscible alloys under intense shearing", *Metall. Mater. Trans. A*, 2009, 40 (9): 2202-2211.
- Kotadia HR, Hari Babu, Fan Z.: "Microstructural refinement of Al–10.2%Si alloy by intensive shearing", *Materials Letters*, 2010, 64 (6), 671-673.
- Kotadia HR, Hari Babu N, Zhang H, Fan Z.: "Microstructure and mechanical properties of Al-9.3%Si alloys under intensive shearing", to be submitted *Metall. Mater. Trans. A*.
- Kotadia HR, Hari Babu N, Zhang H, Fan Z.: "Solidification Behaviour of Al-Si High Pressure Die Castings" to be submitted *Journal of Materials Processing Technology*.

Conference Papers

- Kotadia HR, Patel JB, Fan Z, Doernberg E, Schmid-Fetzer R.: "Solidification and processing of aluminium based immiscible alloys", *Aluminium Alloys: Fabrication, Characterization and Applications II 2009,* San Francisco, CA, 2009, W. Yin, S. K. Das, and Z. Long, ed., TMS, Warrendale, PA, 2009, pp. 81-86.
- Kotadia HR, Patel JB, Fan Z.: "Processing of Al-Sn-Cu ternary alloys by the rheomixing process", *research conference*, 2008, Brunel University.

Poster

- Kotadia HR, Patel JB, Fan Z.: "Al-Sn-Cu based immiscible alloys process by rheomixing", Brunel University, West London, 2007 (Best poster prize award)

Acknowledgements

I am grateful to the EPSRC, UK and DTI for funding this project. I would like to express my sincere gratitude to my supervisor, Prof. Z. Fan, for his guidance and encouragement. I am grateful to Dr. N. Hari Babu for his encouragements and useful discussion throughout my PhD programme and also I would like to thank my collaborators Miss. E. Doernberg and Prof. R. Schmid-Fetzer for important pioneering thermodynamic calculations and useful discussion.

I have received technical help/suggestions from many other people from BCAST during the course of this work. I want to specially mention Dr. J. Patel, Dr. A. Das, Dr. M. Xia, Dr. H. Zhang, Dr. S. Arumuganathar, Dr. S. Kumar, Mr. S. Cook, and other BCAST members for their technical support and scientifically helpful and discussions. I have received much help from fellow PhD students Mr. S. Tzamtzis and Dr. H. Li.

My family have sacrificed the most during my studies but they have always been with me and never lost faith in me. The support I have got from my parents cannot be expressed in words. My parents, Manjulaben and Ramnikbhai always wanted me to become successful in all my endeavours and it is their blessings that took me this far. I am also grateful to my brothers Yagnesh and Samir for their support. The help from my friends Alpesh and Manoj and their family have been outstanding and unforgettable during my life in London.

I have obtained much encouragement and support from my friends here at Brunel University. I am indebted to Miss. Htaik Htar and many others for their friendship and support. I have always enjoyed the company of my friends. Many thanks to my flat mates, especially for the kitchen discussions.

Table of Contents

Nomenclature

A list of symbols is given with a brief description

Symbol	Definition
$\alpha - Al$	Primary aluminium Phase
$\alpha_1 - Al$	Primary aluminium particles formed in short sleeve of the HPDC process or ESCs
$\alpha_2 - Al$	Primary aluminium particles formed in the die cavity of the HPDC process
$\dot{\gamma}$	Shear rate
γ_{lv}	Interfacial energy between the liquid and vapour phases
γ_s	Specific surface energy
γ_{sl}	Interfacial energy between the solid and liquid phases
γ_{sv}	Interfacial energy between the solid and vapour phases
ΔG	Free energy change
ΔG_{hom}	Free energy change for homogeneous nucleation
ΔG_v	Volumetric free energy change for solidification
ΔS_v	Volumetric entropy of fusion
ΔT_{fg}	Undercooling required for achieving the state of free growth
ΔT_{L-S}	Temperature range between the liquidus and solidus
ΔT_{SS-S}	Freezing range
∇T	Temperature gradient
ε	Strain
η	Viscosity of slurry or liquid melt (Eq. 3.2)
η'	Viscosities of the liquid droplets (Eq. 2.4 and 2.5)

θ	Contact angle
λ	Viscosity ratio between two liquids
μm	Micrometer
$\Delta\rho$	Density difference between two liquids
σ	Stress
σ_f	Fracture strength
σ_p	Internal stress of various different phase particles
σ_v	Stress, required for micro-void nucleation
ρ	Absolute density of alloy
τ	Shear force
φ	The crossing angle (Eq. 2.5)
χ	Centre distance between the two spheres (Eq. 2.6)
$d\sigma/dT$	Variation of the interfacial energy between the two liquid phases with a change in temperature
dT/dx	Temperature gradient
$\lvert df_s/dT \rvert$	Slope of the solid fraction versus temperature curve
A	Area
C	Parameter related to the thermal conductivity and the sphere's radius (Eq. 2.5)
D	Outer diameter of the screw (Eq. 3.1 and 3.2)
D	Diameter of particle (Eq. 6.4)
E	Eutectic structure
E	Young modules (Eq. 6.4)
F	Shape factor
G	Gap between the screw flight and barrel surface
H_v	Vickers hardness
κ	Thermal conductivities of the liquid matrix
κ'	Thermal conductivities of the droplets
L	Liquid

L_1	Liquid 1
L_2	Liquid 2
L'	Liquid 1
L''	Liquid 2
L_T	Total length of the test lines
N	Rotation speed of the screw
N_i	Total number grain boundary intersections on line
N_q	The number of the particles per quadrant
N_v	Number of grains per unit volume
P	Applied load
P	Peripheral length of the grains/or particles
R	Radial distance
$\dot{T}$	Cooling rate
T_E	Eutectic temperature
T_C	Critical temperature
T_f^A	Melting temperature of component A
T_f^B	Melting temperature of component B
T_{LC}	Temperature of liquidus of intermetallics phase
$T_{L\alpha}$	Liquidus of the primary solid solution phase
T_m	Monotectic temperature
T_p	Pouring temperature
T_{Sh}	Superheating temperature
T_{SS}	Semi-solid processing temperature
U_1	Velocities of spheres with radius r_1 (Eq. 2.5)
U_2	Velocities of spheres with radius r_2 (Eq. 2.5)
U_M	Velocity due to Marangoni motion
U_S	Velocity due to Stocks motion
X_m	Monotectic composition
X_0	Gross composition of alloy

d	Equivalent diameter (Eq. 3.4)
d	Diagonal length (Eq. 3.8)
d	Diameter of the potent inoculants particles (Eq. 6.3)
f_s	Solid fraction
f_s^{peak}	Peak of solid fraction
g	Gravitational force
h	height of die-cast sample
k	Constant (Eqs. 3.3 and 6.5)
l	length of die-cast sample
$\bar{l}$	Mean intercept length
n	Constants (Eq. 3.3)
q	Quadrant
r	Radius of the liquid droplet
r_1	Spheres with radius r_1 (Fig. 2.4)
r_2	Spheres with radius r_2 (Fig. 2.4)
r^*	Critical nuclei size
r^*_{hom}	Critical nuclei size for homogeneous nucleation
s	Dimensionless distance
v	Volume of mould
z	Half thickness of the wedge shape Cu mould

Abbreviations

BCAST	Brunel Centre for Advanced Solidification Technology
BF	Bright Field
CALPHAD	CALculation of PHAse Diagrams
DSC	Differential Scanning Calorimetric
EDX	Energy-Dispersive X-ray analysis
ESCs	Externally solidified crystals
HPDC	High Pressure Die-Casting
Ma	Marangoni motion

MCAST	Melt Conditioning by Advanced Sheared Technology
MC-HPDC	Melt Conditioned-High Pressure Die-Casting
OM	Optical Microscope
PP	Plane Polarized light
SEM	Scanning Electron Microscopy
St	Stokes motion
TP-1	Test Process-1
WAS	Worldwide Analysis System

Chapter 1
Introduction

1.1 General Introduction

Aluminium alloy castings represent a significant proportion of worldwide metal usage. Al is a low density metal that is advantageous in many applications due to a high stiffness-to-weight ratio. In a pure state, however, it is reasonably soft; its strength can be increased by the inclusion of alloying elements that cause both precipitation and solution hardening resulting in a high strength-to-weight ratio. Thus, Al alloys are in demand for structural and architectural applications, for food packaging, e.g. foil and cans, and in automotive and aerospace industries. An increasing demand for reduced emission levels is expected to continue the growth of Al in the coming years.

Control of the solidification microstructure is one of the most important and widely investigated areas in Al alloys as the morphology, distribution, and chemical identity of the microstructure directly and indirectly influence the mechanical performance and the need for further solid-state processing of components. In the majority of cases, a fine, equiaxed and well-distributed microstructure is beneficial, improving mechanical properties and surface finish. Therefore, grain-refinement in Al alloys has recently raised considerable interest from the research community. It has been recognised that columnar dendritic grains in Al alloys can be modified to equiaxed grains by three main approaches, namely (i) chemical modification, which produces a fine-grain structure through the addition at the trace-level of several elements, such as Al-Ti-B and Al-Ti-C, with research continuing into Al-Sc grain refiners, Al-Zr and Al-Cr are also capable of grain refinement, through rarely used (Quested 2004a, Quested *et al.* 2004b, Murty *et al.* 2002); (ii) physical grain refinement through the external force applied to induce fluid flow during solidification in order to refine the grain size, such as rotation of the mould,

mechanical or electromagnetic stirring of the melt, ultrasonic, and shearing; and (iii) superheating the melt to at a high temperature about 180 to 260 °C above the melting temperature of the alloy (Cao *et al.* 2007). Under all these conditions, grain structures of castings and ingots can be changed from columnar dendrites to equiaxed or globular grains when they solidify in the presence of a sufficiently intensive forced convection, which generally promotes both the homogenization of both temperature and composition of the melt. A more conventional grain refining approach to Al alloys during solidification gives results which are still unsatisfactory.

1.2 Rheomixing of Al-Sn-Cu immiscible alloys

Solidification studies of various immiscible alloy systems are important from both scientific and technical points of view. Al-Sn based alloys have been commonly accepted as having excellent tribological and mechanical properties (Ratke 1993, Ratke and Diefenbach 1995, Davish 1993). Therefore, this type of alloy system is suitable for engineering applications, particularly as self-lubrication bearing materials (Kong *et al.* 2005). Owing to the lower solubility, the parent liquid is decomposed into two distinct immiscible liquid phases when it passes through the immiscibility gap, and this is followed by severe segregation due to the large density difference between the two liquid phases (Ratke and Diefenbach 1995, Yuan *et al.* 2002). To overcome the segregation problem in immiscible alloys many methods have been proposed, such as rapid solidification, stir casting, ultrasonic, and rheocasting. Recently, Fan *et al.* (1999) developed the MCAST (melt conditioning by advanced shearing technology) process to create a fine and homogeneous liquid dispersion within the miscibility gap and then the viscous force offered by the semi-solid slurry counterbalances the gravity force and the Marangoni effect.

Aim and Objectives: The aim of this study was to study immiscible Al-Sn-Cu alloys. Guided by the recently thermodynamically-assessed Al-Sn-Cu system, two model immiscible alloys, Al-45Sn-10Cu and Al-20Sn-10Cu were selected to investigate the effects of intensive melt shearing provided by the novel MCAST process on the uniform dispersion of the soft Sn phase in the hard Al matrix. Our experimental results have confirmed that intensive melt shearing is an effective way to achieve a fine and uniform

dispersion of the soft phase without macro-demixing, and that such a dispersed microstructure can be further refined with precipitation of the primary Al phase prior to the demixing reaction. In addition, it was found that melt shearing at 200 rpm for 60 s will be adequate to produce a fine and uniform dispersion of the Sn phase, and that a higher shearing speed and a prolonged shearing time can only achieve minor further refinement.

1.3 Intensive shearing of Al-Si cast alloys

As an alternative to a chemical approach, physical means have been explored for microstructural modification of Al-Si alloys usually applying low-frequency mechanical mould vibration (Kocatepe and Burdett 2000, Abu-Dheir *et al.* 2005), electromagnetic stirring (Nafisi *et al.* 2006, Hernández and Sokolowski 2006) or ultrasonic irradiation (Eskin 2001, Abramov *et al.* 1998, Jian *et al.* 2005, Xian *et al.* 2006) with varying degrees of success. A successful development of the intensive shearing microstructural modification technique can address several limitations of the chemical method namely, wider applicability irrespective of the alloy constitution, no fading or poisoning effects, and benefits with regards to mechanical and corrosion properties. Intensive shearing during solidification appears to be a promising method for microstructural refinement of Al-Si alloys due to the reported ability in refining Al and Si primary grain structures. However, the origin of grain refinement observed under the application of shearing is still not clear and opens a debate between different nucleation mechanisms. More systematic research effort is necessary to fully investigate the influence of shearing on the evolution of the solidification microstructure and to develop comprehensive knowledge on the microstructural modification mechanisms.

Aim and objectives: The present study investigated the effects of intensive shearing on the solidification microstructure in high Si contenting hypoeutectic and hypereutectic Al-Si alloys and attempted to address the debated issues, namely, the mechanism of grain refinement and the exact nature and origin of the primary α-Al modification and defects. Significantly refined globular primary α-Al grains solidified under intensive shearing were found with supportive evidence towards enhanced heterogeneous nucleation, as the grain refinement mechanism.

1.4 Layout of thesis

The literature review in chapter 2 presents the current status of related research fields. It includes previous studies and understanding regarding solidification of Al based immiscible and Al-Si alloys. An overview of these studies is given in this section, and a detailed review presented in the related chapters.

In the course of this work, an attempt has been made to understand the changes in mechanical and microstructural behaviour of experimental Al alloys as a result of variations in composition. The experimental work in chapter 3 focuses on analyzing the effects of shearing temperature, shearing speed and shearing time on the particle size, grain size and distribution resulting from the melt conditioning by the advanced shear technology (MCAST) unit. Finally, the cast samples examined have similar compositions with the exceptions of intensive shearing in most cases. Microstructural investigations were carried out using different characterization techniques ranging from low resolution methods such as optical microscopy (OM) to high resolution methods such as scanning electron microscopy (SEM). The Al alloys were tested mechanically using tensile testing, and hardness testing. Through this work, an understanding was gained on how intensive shearing and solidification changes, the Al alloys microstructure and mechanical properties.

An understanding of the solidification of complex ternary Al-Sn-Cu immiscible alloys is presented in chapters 4 and 6. The investigation combined two approaches: computational thermodynamics has been used to design alloys; and an experimental approach using both conventional casting methods (without treatment with an external force) and casting under intensive shearing using the newly-developed MCAST process. The phase transformation and mechanisms of immiscible alloys and casting process have been studied. The characteristics of the MCAST unit have been reviewed and the explained fundamental mechanism of the rheomixing process by the MCAST unit explained and quantified in terms of the shearing speed, shearing time, and composition of the alloy.

Chapters 5 and 6 give detailed explanation about the solidification of Al-Si cast alloys under the high pressure die-casting (HPDC) and melt conditioned high pressure die-

casting (MC-HPDC) processes. The effect of pouring temperature on the microstructural and mechanical properties of Al-Si hypoeutectic and hypereutectic alloys have been investigated systematically. Attempts have made to explain the solidification mechanism during the HPDC process and to establish a correlation between the microstructural observations and mechanical properties. In order to explain these results a detailed qualitative as well as quantitative understanding of HPDC and MC-HPDC solidified samples and an investigation of mechanical properties under different processing conditions have highlighted the benefit of the MC-HPDC process over HPDC process.

The results from chapters 4 and 5 are drawn together in a discussion in chapter 6. The aim of this chapter is to explain the subject of the thesis and why the intensive shearing method is important for synthesizing Al alloys with the mechanisms correlated through the experimental results. This will enable Al producers to control, modify and optimize their casting processes, resulting in better products and economic savings in addition to facilitating more rapid development of new alloy compositions and casting techniques.

Chapter 7 summarises the thesis, and the main conclusions and chapter 8 suggestions for future research are given.

Chapter 2
Literature Review

2.1 Immiscible alloys

2.1.1 Introduction

Immiscible alloys are systems with a *miscibility gap* in the liquid state and are of fundamental interest to the scientific community (Ratke 1993, Ratke and Diefenbach 1995, Ratke *et al.* 1996). Up to now, more than 500 binary immiscible systems are known (Yuan *et al.* 2002) and many other multi-component systems are known to exhibit a miscibility gap in the liquid state. The phase separation in most of these alloys has, however, not been investigated in sufficient detail. Immiscible alloys have been used for many years for the production of self-lubricating bearing materials. These materials consist of a dispersion of a lubricating soft phase, such as graphite, Sn or Pb, in a hard matrix (e.g., Al, Al-Cu, Al-Si) for mechanical support (Ratke 1993, Ratke and Diefenbach 1995, Yuan *et al.* 2002).

Before 1970, limited studies relating to immiscible alloys were carried out due to a lack of experimental means. After 1970, the development of aerospace science and technology made it possible to study immiscible alloys even under microgravity conditions (Yuan *et al.* 2002). Experimental and theoretical researchers have investigated extensively the factors influencing the phase separation process under gravity and microgravity conditions (Langbein 1984, Regel 1989). Besides gravity, a large number of possible additional mechanisms have been identified theoretically which may influence the phase separation (Tegze *et al.* 2005). However, a lack of a complete scientific understanding of the phase separation process both experimentally and theoretically still attracts worldwide researchers (Zhao and Ratke 2004). In addition, the need for immiscible

alloys with specific properties for engineering applications demands the development of novel fabrication processes (Peng and Fan 2001).

One of the major challenges for the processing of immiscible alloys is that the liquid becomes separated quickly due primarily, to the *Stokes motion* and *Marangoni motion* (Fang and Fan 2006). This technical processing problem limits their applications. Component separation due to nucleation and growth of the new liquid phase makes it difficult to produce fine dispersions (Ratke and Diefenbach 1995, Ratke *et al.* 1996). The quality of the final products is determined by the microstructure, which, in turn, is largely determined by complex phenomena taking place when the homogeneous liquid existing above the *binodal* line is cooled through the two-phase region (Ratke and Diefenbach 1995, Ratke *et al.* 1996, Tegze *et al.* 2005,Yuan *et al.* 2002). Therefore, dispersions are of interest for a variety of practical applications.

So far immiscible alloys have not been applicable for solidification processing of components because of the rapid separation of the liquid during cooling under the influence of gravity. Usually layer structures or coarse dispersions are obtained. Even under microgravity conditions, productions of fine and uniform dispersed structures have not been achieved (Ratke *et al.* 1996, Yuan *et al.* 2002). These unexpected results have spurred both theoretical and experimental activities in order to identify the mechanisms that cause coarsening and component separation even when sedimentation and buoyancy is largely eliminated.

2.1.2 Solidification characteristics of immiscible alloys

The solidification processes occur in immiscible alloys during continuous cooling from the single–phase liquid regime above the binodal line into the two-phase regime (Ratke and Diefenbach 1995, Ratke *et al.* 1996, Tang 2003a, Yuan *et al.* 2002, Yuan 2001,). The solidification can be summarized as follows.

The binary phase diagram for an immiscible alloy has a miscibility gap in which the homogenous melt rapidly decomposes into two distinct immiscible liquids. Fig. 2.1a illustrates a typical binary phase diagram of an immiscible alloy. Above a critical temperature, T_c, both components are completely soluble in each other. On cooling an alloy with a gross composition X_0 from a temperature $T > T_c$ the homogeneous liquid L

will decompose into the liquids L_1 and L_2 when crossing the binodal line, path "mcb", (i.e. the curve of coexistence) and can be written as:

$$L \rightarrow L_1 + L_2 \tag{2.1}$$

The direct observation of the kinetics of the phase separation from liquid L to L_1 + L_2 which coexist in equilibrium is not possible, i.e. alloys with a gross composition between X_m and X_{L2} will then be in a two-phase liquid state, this is interesting but the mechanism appears to be complicated (Ratke and Diefenbach 1995, Ratke *et al.* 1996, Tang 2003a,Walter 1986).

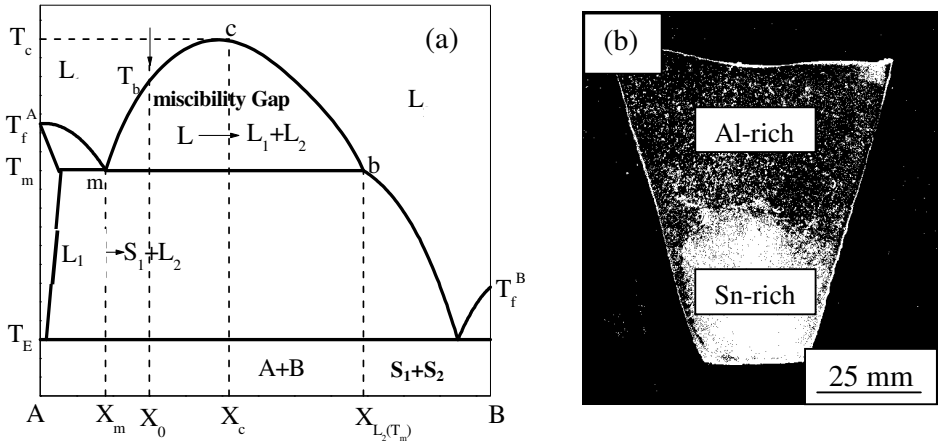

Fig. 2.1. (a) Schematic diagram of a typical binary phase diagram with a miscibility gap in the liquid state. T_c – critical temperature; T_f^A – melting temperature of component A; T_f^B – melting temperature of component B; T_b – melting temperature at X_0 composition; T_m - monotectic temperature; X_m – monotectic composition; X_0 – gross composition of the alloy considered; L_1, L_2 designate the two different liquids being in equilibrium below the critical temperature (Walter 1986) and (b) Structure of Al-45Sn-10Cu sample solidified in a gravity field at 3.5 Ks^{-1} cooling rate showing coarse segregation of the Sn-rich phase (bottom) and Al-rich phase (top).

On further cooling, the liquid L_1 decomposes at the monotectic temperature T_m into the solid phase S_1 and the liquid L_2 of composition $X_{L2(Tm)}$. This reaction is known as a

monotectic reaction, which is similar to a formal eutectic reaction except that one of the product phases is a second liquid phase, L_2, as follows:

$$L_1 \rightarrow S_1 + L_2 \tag{2.2}$$

The alloy is now a mixture of solid S_1 and liquid L_2 which will completely solidify, if it is cooled below the eutectic temperature T_E. The third reaction is the *eutectic reaction* in which the liquid L_2 decomposes to give two solids as:

$$L_2 \rightarrow S_1 + S_2 \tag{2.3}$$

In a normal gravity field, serious gravity segregation occurs and also leads to a layered structure due to the sedimentation of the heavier phase. The layered structure of an Al-45Sn-10Cu sample solidified in earth's gravity condition with a 3.5 Ks^{-1} cooling rate can be seen in Fig. 2.1b.

2.1.3 Liquid-liquid phase separation of immiscible alloys

It was believed before 1970 that in the early stages of cooling, the large density difference of the alloying elements leads to rapid spatial separation resulting in two layer structures (Yuan *et al.* 2002). However, a recent microgravity experiment shows that phase separation still occurs without the effect of the gravitational force, due to wetting phenomena, *Ostwald ripening* and *thermo-capillary* migration (Marangoni motion).

The phase separation process includes nucleation of the minority phase, growth of the nuclei, and coarsening. It has been generally accepted that fluid flow also plays an important role in this process. The various physical processes that are used to explain the phase separation in an immiscible liquid are (Tegze *et al.* 2005):

- *Diffusion-related processes*
  i) Coagulation due to Brownian motion of the droplets (Binder–Stauffer (BS) mechanism) (Binder and Stauffer 1976).
  ii) Evaporation–condensation type interaction (Lifshitz–Slyozov–Wagner (LSW) mechanism) (Lifshitz and Slyozov 1961, Wanger 1961).

iii) Diffusion coupling, where the iso-concentration lines include two or more droplets, which then attract or repel each other depending on the composition gradient (Tanaka's first (T1) mechanism) (Tanaka 1995).

- *Hydrodynamic effects*

  iv) Flow-assisted coagulation (FA).

  v) Collision-induced collision, where the flow field of two coagulating droplets induces further coagulation events (Tanaka's second (T2) mechanism) (Tanaka 1996).

  vi) Hydrodynamic coarsening driven by capillary instability (Siggia's (S) mechanism) relevant for bicontinuous phase separation (Siggia 1979).

- *Hydrodynamic effects coupled to external fields*

  vii) Marangoni motion (*Ma*): Thermo-capillary forces drive the droplets with a velocity increasing with size, thus large droplets capture smaller droplets.

  viii) Stokes motion (St): Buoyancy forces drive the droplets with a velocity increasing with the square of the linear size, thus large droplets capture smaller droplets.

Three of these main phenomena are discussed below.

2.1.3.1 Marangoni migration

Marangoni motion of the drops and/or bubbles in a temperature gradient can lead to undesirable spatial separation of the phases both on the Earth and in low-gravity environments. The first detailed research of the thermo-capillary motion of a bubble in a temperature gradient was carried out by Young *et al*. 1959. In brief, Marangoni migration described as the temperature gradient around the bubble causes a surface tension differential along the bubble surface (Young *et al.* 1959, Takahashi *et al.* 1999). The surface tension gradient leads to a tangential stress at the bubble interface, which drags the neighbouring liquid from the cold (low-surface-tension) region to the warm (high-surface-tension) region. This surface tension gradient caused by the temperature variation (thermo-capillary) is responsible for drop migration, as shown in Fig. 2.2 (Takahashi *et al.* 1999).

Marangoni motion can also be higher when compared to solid particles or very viscous drops approaching the solidification front. The drop will be rippled even if it is

characterised by a very low viscosity. Since the magnitude of the surface Marangoni flow is a decreasing function of the drop viscosity, the lower the viscosity, and the larger will be a repulsive force. In particular, this force increases as a function of the drop diameter and is an inverse function of its viscosity. The velocity of a drop caused by Marangoni motion (U_m) can be described by the following equation (Young *et al.* 1959):

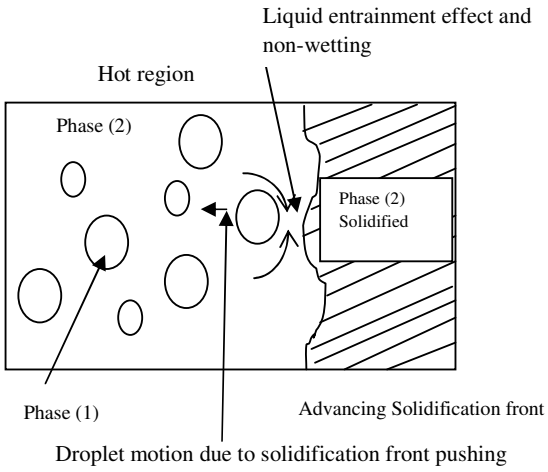

Fig. 2.2. Schematic illustration of drop pushing due to solidification and non-wetting behaviour (Lappa 2004).

$$U_m = \frac{2\left|\frac{dT}{dx}\right|\left|\frac{d\sigma}{dT}\right|\kappa}{(2\eta + 3\eta')(2\kappa + \kappa')} r, \tag{2.4}$$

where $d\sigma/dT$ is the variation of the interfacial energy between the two liquid phases with a change in temperature, dT/dx is the temperature gradient, r is the radius of the liquid droplet, κ and κ' are the thermal conductivities of the liquid matrix and droplets respectively, and η , η' are the viscosities of the liquid matrix and droplets respectively.

2.1.3.2 Collision and coagulation

Liquid droplets that form during phase separation collide with each other so that they mutually reduce surface energy by joining to form a single one (Fig. 2.3). This can serve to demonstrate the coarsening and coagulation of liquid droplets. When two drops

become sufficiently close, they are assumed to interact with each other due to hydrodynamic disturbances. Moreover, their motion may be influenced by the presence of neighbouring particles. The shape of the droplets also plays an important role and can substantially alter the migration and sedimentation velocity (Lappa 2004, Ratke and Diefenbach 1995). Drops with lower viscosity align and coalesce due to shape deformation and drops with higher viscosity become stretched and may break as a result of the hydrodynamic interaction. Smaller drops with a larger viscosity tend to be swept around the larger ones.

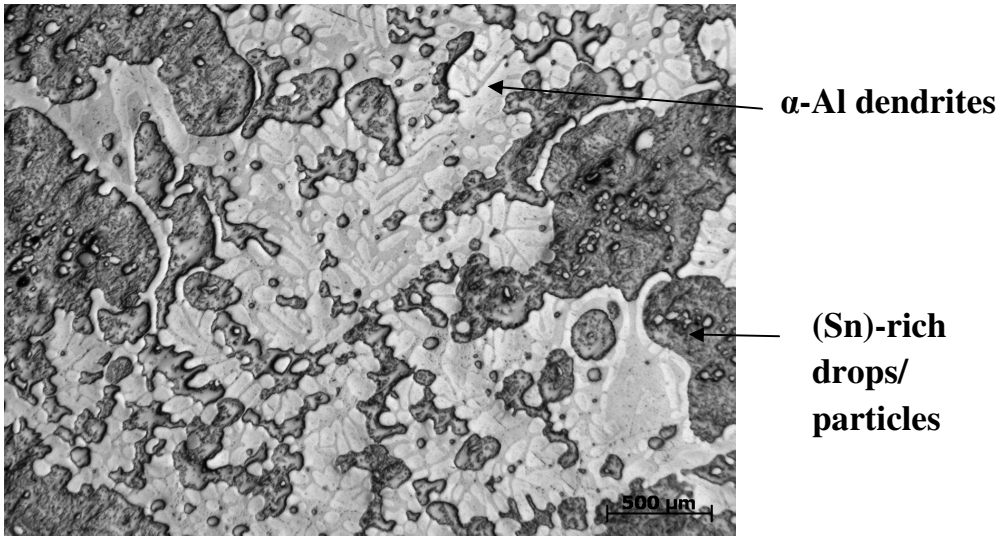

Fig. 2.3. Optical micrograph of Al-45Sn-10Cu alloy showing the collision and coagulation of Sn droplets. The sample solidified in a gravity field in a steel mould from 650 °C.

The details of the collision and coalescence between droplet spheres may be explained as follows. Two spheres with radius r_1 and r_2 move in the radial direction in the atomized droplet at the velocities U_1 and U_2, respectively, as illustrated in Fig. 2.4a. The crossing angle between the two velocity vectors is defined as φ and the curve length (l). Based on the geometry shown in Fig. 2.4b, the collision kernel $K(r_1, r_2)$ can be calculated by (He *et al.* 2006):

$$K(r_1, r_2) = \pi E(r_1, r_2) \cdot [U_1(r_1) \cdot \sin\varphi + r_1 + r_2]^2 \times \left| U_2(r_2) - U_1(r_1) \cdot \cos\varphi \right| \tag{2.5}$$

The collision efficiency $E(r_1, r_2)$ is given by:

$$E(r_1, r_2) = \exp\left(-2\int_2^{\infty} \frac{12C}{s(s^3 - 8C)} ds \right) \tag{2.6}$$

where C is a parameter related to the thermal conductivity and the sphere's radius, and dimensionless distance $s = 2\chi/(r_1, r_2)$ with χ being the centre distance between the two spheres. Because the crossing angle φ is very small, it can be approximately written as:

$$\varphi = \frac{l}{R} \approx \frac{r_1 + r_2}{R} \tag{2.7}$$

where l is curve length and R is radial distance.

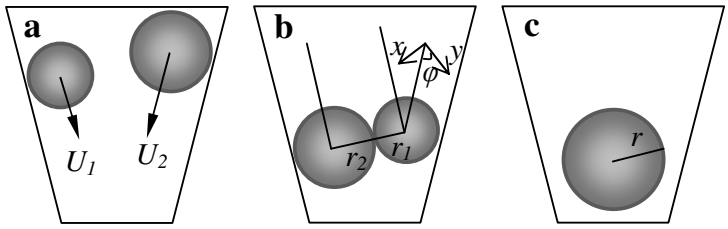

Fig. 2.4. Collision and coagulation between two migrating spheres: (a) two spheres with radius r_1 and r_2 move towards the centre of the atomized droplet at velocities U_1 and U_2, respectively; (b) the large sphere overtakes the small one, and they combine with each other. The velocity U_1 is divided into x-axis (vertical direction of U_2) and y-axis (parallel direction of U_2) to calculate the collision kernel; (c) the two spheres form a new, larger sphere with radius r (He *et al.* 2006).

2.1.3.3 Droplet sedimentation

It is difficult to control the stability of the solidification process as well as it is difficult in controlling the sedimentation or floatation of the second phase droplets before they grow up to their critical sizes. Therefore, it is still difficult to produce homogeneous ingots under a normal gravitational condition (Clift *et al.* 1978).

The drops of different sizes will be in relative motion due to their different settling velocities induced by gravity, or their different migration velocities induced by the internal surface tension gradient (Lappa 2004) as explained in the previous section. Above T_c, the liquid composition is more uniform and at the initial stages below T_c, the nucleated droplets are most likely to be uniformly suspended throughout the volume of liquid. According to Stokes motion as solidification progresses, particular in a metallic system, droplet sedimentation takes place (assuming the drop density is higher than the parent liquid, e.g. Sn drops in an Al-Sn binary system). When the drops reach the bottom of the container, they coalesce into an overlying, segregated layer of liquid phase. This layer grows with time until all the dispersed drops have coalesced into it. The problem becomes worse when drops also collide and coalesce with each other as explained in the previous section. This gravitational force is an increasing function of the drop diameter and an inverse function of its viscosity. The velocity of the Stokes motion (U_s) of a droplet in the matrix phase can be described by:

$$U_s = \frac{2g\Delta\rho(\eta+\eta')}{3\eta(2\eta+3\eta')}r^2, \tag{2.8}$$

where, $\Delta\rho$ is the density difference between the two liquids, and g is the acceleration due to gravity.

A review article by Langbein (1984) on immiscible alloys, concludes that the phase separating process is a three-stage-process (Fig. 2.5):

(i) *Nucleation stage*: When the original melt is cooled down to the critical temperature, a large number of nuclei or droplets will form quickly in the melt through energy and concentration fluctuations.

(ii) *Growth and coarsening stage*: The second phase droplets grow up or shrink by diffusion (namely Ostwald ripening). At the same time, they coarsen continuously through collisions including Marangoni and Stokes collisions.

(iii) *Sedimentation stage*: When the droplets coarsen up to a considerable value, sedimentation arises due to the density difference between L_1 and L_2. In addition to sedimentation, the second phase droplets (L_2) also coarsen continuously by Marangoni coagulation and predominantly by Stokes coagulation.

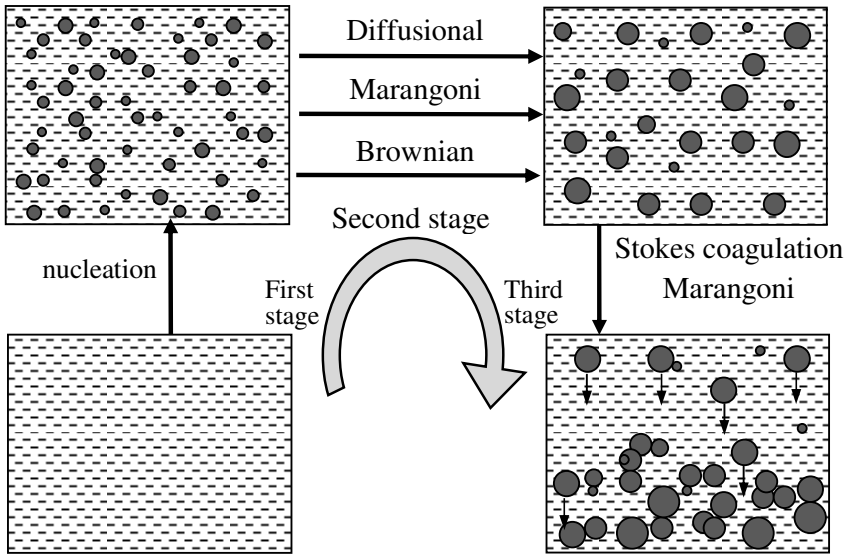

Fig. 2.5. Schematic diagram illustrating the liquid-liquid decomposition process of an immiscible alloy (Langbein 1984, Yuan *et al.* 2002).

2.1.4 Possible techniques to produce a well-dispersed microstructure

Applications for immiscible alloys were not identified before 1970 due to the processing difficulty associated with the limited understanding of the liquid-liquid phase separation mechanism. After that, the development of aerospace science and technology made it possible to study immiscible alloys in microgravity conditions. Recently, with the development of preparation techniques as well as the need to develop immiscible alloys for specific properties, researchers have paid more attention to further research work on immiscible alloys. Several preparation technologies such as powder metallurgy, directional solidification, casting under microgravity conditions, stir casting, controlled casting, and rapid solidification, etc. have been applied for their processing (Tang 2003a). A brief introduction to a few newly-developed and commonly-used methods are discussed below and Table. 2.1 tabulated the principles and limitations of these fabrication techniques.

Table. 2.1. Fabrication methods for immiscible alloy (Tang 2003a)

Fabrication			Principles	Problems	
Powder metal method			Well mixed in powder	Complex, powder oxide	
Directional solidification			Aligned monotectic growth	Difficult to control, expensive	
microgravity	Space station		Eliminated *g*	*Ma* motion, inhomogeneous	Very expensive
	artificial	Parabolic flight	Reduced *g*		Expensive
		Drop from the tower			Limited time
		Orthogonal electromagnetic	Current force balance g		inhomogeneous
Stirring	Mechanical		Break up	coagulation	
	Ultrasonic vibration		Avoid coagulation	Pb<1-wt% in Al-Pb	
	Magnetic vibration		Avoid coagulation	inhomogeneous	
Orientating temperature gradient			Marangoni force balance gravity	Difficult to control direction	
Rapid solidification	Spray		Disperse particles/ droplets		
	Mould cooling		Avoid coagulation	Small quantity or In <30 wt.% in Al-In, 4 mm thickness	
	Coating		Disperse particles	Conflict between temperature of cohesive bonding and eutectic	
	planar		Film forming	Size and surface finish, Pb <10wt.% in Al-Pb	
Particle centrifuging molten			Disperse particles		
Rheomixing			Mixing by MCAST, stabilized in SSM state by the viscosity counterbalance *g, Ma*	Simple, fine particle, uniform size, homogeneous dispersion	

2.1.4.1 Rapid solidification/ cooling techniques

Duwez *et al.* (1960) at the California Institute of Technology developed rapid solidification technology. Rapid solidification using piston and anvil techniques and more recently melt spinning allowing for cooling rates from 10^5 Ks^{-1} have been used to freeze the early stages of separation and achieve a better dispersion.

It has been recognized that the segregation of the second phase is dependent on the dynamical processes (i.e. the growth, the coagulation as well as the movement of the

second phase droplets). In rapid solidification, due to its negligible duration, the dynamically coarsening process is suppressed; as a result, the second-phase droplets will be entrapped within the matrix phase. With this method, immiscible alloys with a fine dispersed structure have been achieved. Fig. 2.6 shows several rapid solidification processes often used to prepare immiscible alloys.

2.1.4.2 Stir casting

Vigorous stirring is not only used for to disperse minority phase droplets in the matrix but also used to avoid the further coalition, coagulation, and settling of the second-phase particles. It is important to note that dispersion of the minority particles also depends on the type of stirrer used for mixing (Harnby *et al.* 1985) and other related parameters such as stirring temperature, stirring time, and the viscosity of the liquid are important (Mohan *et al.* 1989a, Mohan *et al.* 1991). These techniques generally include mechanical stirring (Ichikawa and Ishizuka 1987, Mohan *et al.* 1989a, Mohan 1989b, Mohan *et al.* 1991, Pathak *et al.* 1979), ultrasonic stirring (Lee 1984, Mohan *et al.* 1990), and induction stirring (Ashok and Rajan 1996).

2.1.4.3 Controlled casting

This is designed for some particular alloys in such a way that the temperature gradient is imposed in the opposite direction to the Stokes motion so as to make the Marangoni motion direction opposite to the Stokes motion. It is important to counteract both motions to produce a uniform microstructure. Again it is worth mentioning that these motions have a direct relation with droplet sizes. As shown in Fig. 2.7 in which U_s and U_M are the Stokes migration rate and Marangoni migration rate, respectively, when the size of the droplets is very small, Marangoni migration will be predominant. Otherwise Stokes motion will be predominant. When the droplet grows up to a critical size, its net velocity will reach zero. A uniform distribution of the second-phase particles can be obtained, by controlling the stability of the solidification by using an external force or temperature gradient (Uffelmann *et al.* 1996).

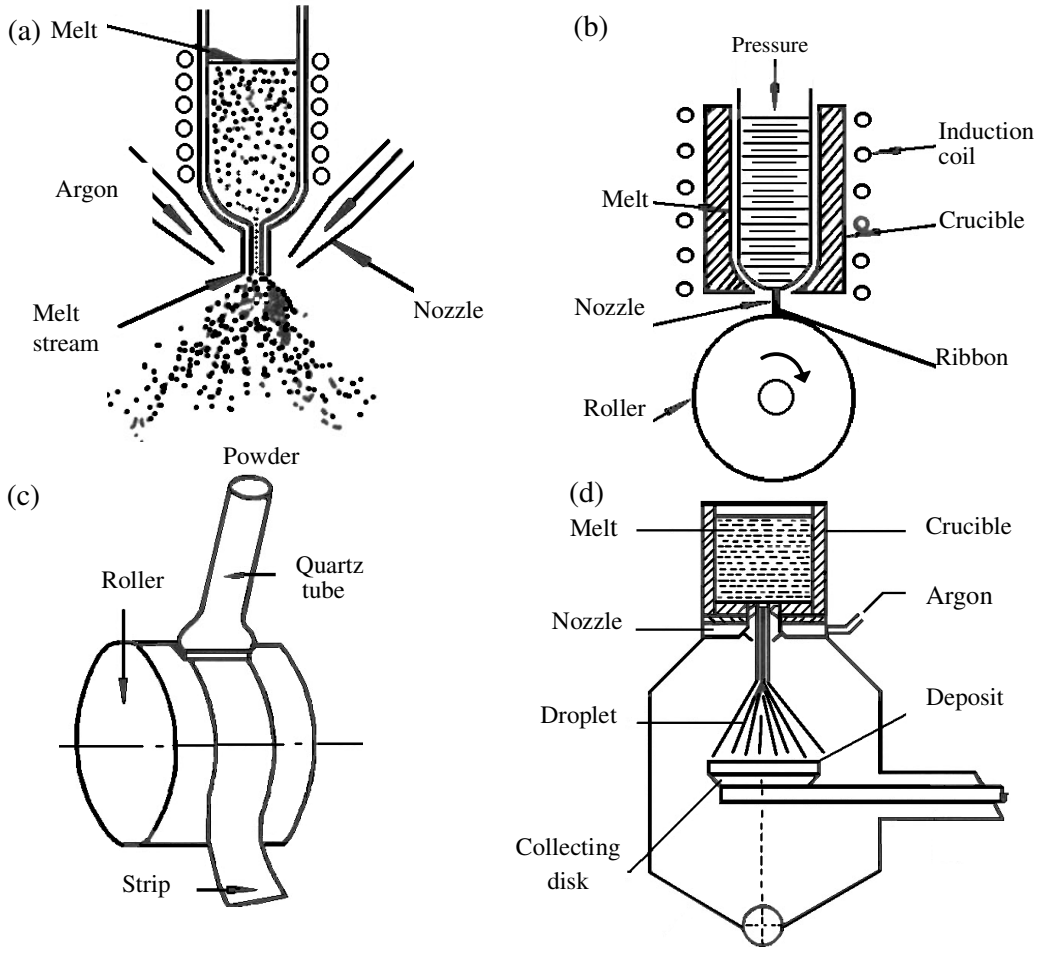

Fig. 2.6. Schematics illustration of several typical rapid solidification processes employed to prepare homogeneous immiscible alloys (a) Inert gas atomization (Li *et al.* 1998), (b) Melt spinning (Kim *et al.* 1991), (c) Plane flow casting (PFC) (Wei *et al.* 1993), and (d) Spray deposition (Zhang *et al.* 1988).

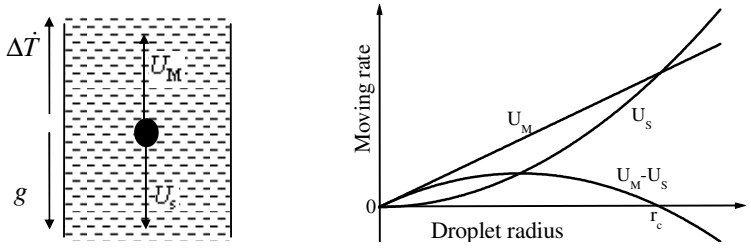

Fig. 2.7. Sketch of the controlled casting principle (Yuan 2001).

2.1.4.4 Drop tube technique

A drop tube technique consists of a column of few metres high with an induction furnace at the top; a sample can be melted in a crucible positioned in the furnace and then ejected with a high gas pressure from a small hole at the bottom of the crucible. Falling in the column, the melt separates into small droplets which solidify rapidly because of their small size. Several authors have processed Cu-Co alloys by drop a tube and produced fine Co-rich droplets (Cao *et al.* 1999, Cao *et al.* 2000, Cao *et al.* 2002, Cao *et al.* 2003, Lu *et al.* 2003, Kolbe and Gao 2005, Munitz and Abbaschian 1991). This can be useful method to study the growth of Co-rich liquid droplets after the liquid phase separation.

2.1.4.5 Rheomixing

The twin screw rheomixing process is a promising technology in the polymer processing industry. In this process, co-rotating twin-screws provide the high shear rate and turbulence. Recently, this process has been applied to the processing of various metallic alloys at an enhanced temperature (Fan 2002) and successfully produced superior microstructures. Since the rheomixing process based on a twin-screw machine can offer a high degree of turbulence with intensive shearing, investigating the droplet formation under such conditions in the immiscible liquids will be of fundamental interest. Drop formation and rupture is shown to take place under shear flow (Scardovelli and Zaleski 1999) and it can have a direct effect on the microstructure of immiscible alloys.

The hydrodynamic behaviour of a single drop in shear flow and the breakup transient process have been investigated by various numerical methods. The single viscous drop deformation in a steady laminar shear flow has been studied by Tylor (1932 and 1934). More recently, experimental observations of drop deformation and breakup have been reported by Bentley and Leal (1986), Loewenberg and Hinch (1996), Mason and Bibette (1997), Siegel (1999), and Stone (1994). The deformation and rupture in a simple shear flow is the most common feature in emulsions, and occurs widely in various industrial processes, such as food processing, pharmaceuticals, biomedicines, as well as in materials processing. A numerical study of an immiscible drop in a turbulent flow has been studied using numerical simulation tools by Hagiwara *et al.* (1997), which show the

shape of the drop to be dependent on the local flow regime classified by four turbulence structure types.

A rheomixing process is carried out in a MCAST unit or twin-screw machine (Fan 1999). The MCAST technology has been extensively used to process Al and Mg based alloys with fine and uniform grain structures.

The main characteristics of a rheomixing process are;

- Size of particles: fine and uniform diameter.
- Morphology of particles: close to spherical shape.
- Dispersion of particles: homogeneous distribution.
- Suspension of particles: stable state for solidification

2.1.4.5.1 Droplet breakdown

Below the binominal line the minority phase or drop forms and is suspended in the matrix. During further solidification the minority phase (the denser phase) segregates to the bottom of the mould in conventional casting. Therefore a droplet dispersion mechanism is required with appropriate temperature and enough external force to fully breakup, refinement and stop further coalescence during solidification. The immiscible liquid drops breakup into small droplets in shear-induced flow, with small daughter drops forming under shear (Tang 2003a). The shear rate in the twin screw rheomixing process is distributed in the flow field with an area of high shear rate located between the top of the screw and barrel wall, in addition to an area located near the tip of the two flights and a low shear rate area in the middle of screw channel. Furthermore, from previous research (Fan *et al.* 2001, Utracki and Shi 1992) it was noted that the drop deformations and their shape was strongly influenced by the viscosity ratio λ. The viscosity ratio is defined as the ratio of drop viscosity and matrix phase viscosity. One is the viscous shear stress $\dot{\gamma}\eta$ of the matrix phase, which causes drop deformation, and the other is the characteristic Laplace pressure σ / r, which resists the deformation. The capillary number $\mathrm{Ca} = \dot{\gamma}\eta r / \sigma$, is defined as the ratio between these two forces and provides a useful measure of the efficiency of the shear flow to deform the drop. Tang (2003a) suggested that, binary Pb-Zn immiscible alloy breakup should be completed in the fluid state with low viscosity of the matrix phase in order to obtain fine droplets and short

processing time and according to the computational simulation droplet break a "*millisecond*" during the shearing under rheomixing process.

During intensive shearing of the liquid, droplets are in constant movement within the matrix phase fluid. The material transfer direction is opposite to the direction of screw rotation in the rheomixing process, which means that the shear rate direction is reverse to the direction of fluid velocity. After full breakup, refinement and coalescence occur through the interaction between daughter droplets. However, the mixing behaviour of daughter droplets in shear-induced flow has not been reported in the literature. The rupturing, interaction and dispersions of droplets is the essential microscopic mechanisms of the twin-screw unit (Fan 2002).

2.1.5 Application of immiscible alloys

The central applications of immiscible alloys are as bearing materials (Cu-Sn-Pb), power switch contact materials (Ni-Ag), and superconducting materials (Al-Sn, Cu-V) or materials for filters (Ratke 1993). The plain bearing application is the most attractive one and it helps to reduce fuel consumption for automobiles and air pollution. It is widely accepted that an immiscible alloy-based bearing material can fulfil the following requirements (Kingsbury 1992);

- Embeddability - to allow hard particles to embed in the bearing material.
- Compatibility - to avoid damaging or roughening the counter face.
- Conformability - to accommodate slight misalignment in the bearing system.
- High strength - to support applied loads.
- Fatigue resistance and corrosion resistance for a longer service life.

Generally microstructures of the plain bearing materials are a combination of soft and hard phases in a matrix. The soft phase provides good embedding characteristics (for example, for dirt particles in a lubricant); whereas the hard phase considerably reduces material wear (Davis 1993). However, the final tribological property depends on the volume fraction of such hard phases and their size and distribution (Prinz and Romero 1993, Ratke 1993,). The soft phases, which are responsible for good embedding performance, should be of a compact structure. However, with traditional bearing

materials, these phases are the ones to crystallise as eutectic phases, which by their nature is not of a compact structure.

Monotectic alloys, such as ternary Al-Sn-Cu, Al-Si-Pb and Al-Si-Bi alloys offer better bearing applications (Prinz and Romero 1993). The challenge for process engineers is to synthesise these monotectic alloys with good dispersion of the soft phase by using a reliable and economical technique. In addition, dispersion of the soft phase is difficult due to the considerable density difference between hard and soft phase alloys.

2.2 Al-Si Alloy

2.2.1 Introduction

Al and its alloys are some of the most simple and common class of metallic materials used in the foundry world. About 20% of Al is consumed as cast products. The most commonly used methods of processing are sand casting, permanent mould (gravity die) casting, and high pressure die-casting (HPDC). Apart from light weight, the attractive feature of Al alloys for casting include the relatively low melting temperature, negligible solubility with gases except hydrogen, and the good surface finish that is usually achieved in final products (Davis 1993, Polmear 1995).

Al alloys with Si as the major alloying addition are the most important group of the Al casting alloys mainly because of the high fluidity imparted by the presence of a relatively large volume of Al-Si eutectic. Al-Si alloys are noted for their unique combination of desirable characteristics, including excellent castability, good weldability, high resistance to corrosion, and good mechanical properties. In addition, the presence of Si reduces both shrinkage during solidification and the coefficient of thermal expansion of the cast products (Davis 1993).

The Al-Si binary alloy system is a simple *eutectic system* with the eutectic composition at 12.7%Si (all compositions in this study are given in weight percent unless otherwise stated). The *hypoeutectic* alloys consist of a soft, ductile primary Al phase and a very hard, brittle Si phase associated with the eutectic reaction (Davis 1993, Elliott 1984, Polmear 1995,). This Si phase contributes to very good wear resistance of these alloys (Crosley and Mondolfo 1966, Dash and Makhlouf 2002, Davis 1993, Elliott 1984,

Makhlouf and Guthy 2002, Polmear 1995, Yilmaz and Elliott 1989). The *hypereutectic* alloys are most commonly used as wear resistant alloys and contain coarse primary Si particles as well as eutectic Si (Elliott 1984, Kyffin *et al.* 2001, Makhlouf and Guthy 2002). These primary Si particles impart excellent wear resistance to the alloys. Typical micrographs of the hypo and hyper eutectic alloys are shown in Fig. 2.8.

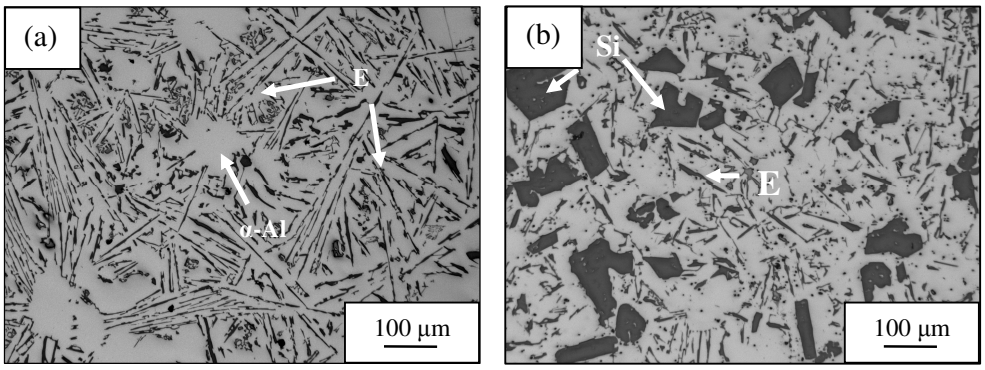

Fig. 2.8. Optical micrographs showing typical microstructures of (a) hypoeutectic and (b) hypereutectic Al-Si alloys. Where E = Eutectic Si; α-Al = Primary Al; and Si = Primary Si phase. Samples were allowed to solidify in a graphite crucible from 650 °C.

2.2.2 Effect of alloying elements on binary Al-Si alloys

Because of the good fluidity and hot tearing resistance, Al-Si alloys are used in the HPDC process. The equilibrium maximum solid solubility of Si in Al is 1.9% at 567 °C (Davis 1993). A commercial Al-Si alloy generally contains other alloying elements to further enhance the mechanical properties of these alloys. These alloying elements at a level between 5-20wt.% impart a significant improvement in casting characteristics relative to other Al alloys. As a result, these high Si alloys are generally used as casting alloys rather than for the manufacture of wrought products. The addition of other alloying elements to an Al-Si alloy provides better mechanical properties such as improved tensile properties and corrosion resistance. The major Al-Si alloy groups used commercially are (Street 1986):

- Al-Si-Cu alloys: provide good casting properties with moderate strength and hardness.

- Al-Si-Mg alloys: offer good permanent mould casting properties and are amenable to heat treatment to give improved strength and hardness.
- Hypereutectic Al-Si-Cu-Mg alloys: offers good wear resistance and are commonly used as engine parts.

Iron is the most common alloying element, which can be tolerated up to level of 1.5 to 2.0%Fe. The presence of Fe in Al-Si alloys introduces as many as six different Al-Fe-Si base *intermetallic* phases. Commercial Al-alloys always contain Fe, often as an undesirable impurity and occasionally as a useful minor alloying element (Mondolfo 1976, Fang *et al.* 2007). As a minor alloying element, Fe has been used occasionally in Al-Cu-Ni alloys to enhance the high temperature mechanical properties, in Al-Mg alloys to reduce coarsening, in Al-Fe-Ni alloys to enhance corrosion resistance by steam (Mondolfo 1976), and in high pressure die-cast (HPDC) Al-alloys to facilitate ejection and to help die-release (Wang *et al.* 1995, Winkelman *et al.* 2004). In industrial practice, the Fe pickup results mainly from the use of steel tools during melting and casting, and the use of scrap material (Davis 1993, Street 1986). For the vast majority of Al-alloys such as Al-Si based cast alloys, the presence of Fe is detrimental to the mechanical properties (Davis 1993), and Fe pickup is thus a major problem for industrial use and the recycling of Al-alloys. The most common intermetallics are hexagonal α-AlFeSi (Al_8Fe_2Si) and monoclinic β- AlFeSi (Al_5FeSi) phases. Fig. 2.9 shows typical micrographs of a hypoeutectic alloy with α and β phases. Other iron-bearing phases such as Al_6Fe and Al_3Fe can also be found in these alloys (Fang *et al.* 2007).

Magnesium is added to provide strengthening through precipitation of Mg_2Si in the matrix. In an Al-Fe-Si-Mg alloy, the Al-Fe-Si phase will not be affected by the addition of Mg. However, Mg can combine with insoluble Al-Fe phases, resulting in a loss of strengthening potential (Davis 1993).

The maximum solid solubility of Mg in Al is up to 15.4% at 450 °C, falling to about 2% at 100 °C. The combination of Mg and Si in the alloys gives rise to the formation of a Mg_2Si intermetallic phase (Street 1986). The solution heat treatment separates Mg and some Si from the solid solution phase, which is retained by quenching. Subsequent aging,

with both time and temperature being variables, allows controlled precipitation of Mg_2Si in the Al matrix resulting in significant increased strength.

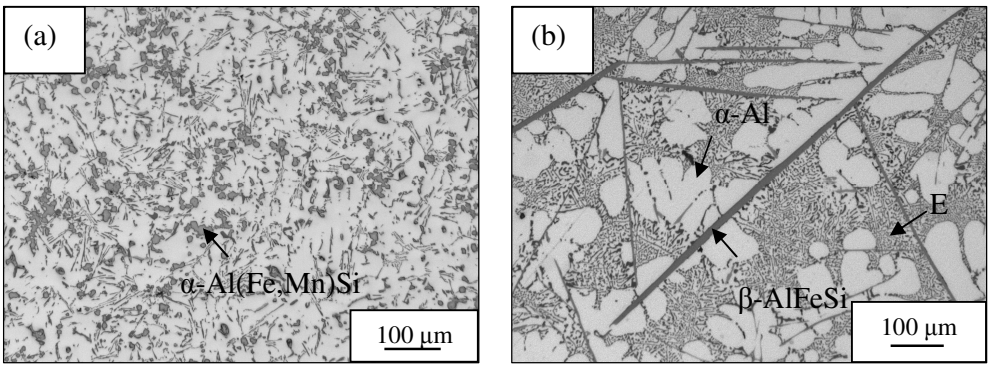

Fig. 2.9. Optical micrographs of a Al-9.4Si alloy with 2.04 wt.% Fe (pouring temperature 640 °C) (a) General view to show the presence of primary intermetallics phases – the compact α-Al(Fe,Mn)Si compound and the needle-shaped β-AlFeSi compound and (b) Higher magnification to show the dendritic α-Al (white in contrast), the interdendritic eutectic regions (indicated as "E") and the large primary β-AlFeSi needles.

Copper is the most common alloying element for improved wear resistance Al-Si alloys. The maximum equilibrium solid solubility of Cu in Al is up to 6% at 546 °C (Davis 1993). Cu additions impart additional strengthening of the matrix through precipitation hardening process (Al_2Cu phase) (Polmear 1995) or through the modification of the hard, brittle Al-Fe-Si phases by substitution in these intermetallics phases. As the strength of these alloys increase with the addition of Mg and Cu, some sacrifice in ductility and corrosion resistance occurs (Davis 1993). The Al_2Cu precipitation is controlled by heat treatment. To obtain optimum corrosion resistance in a Al based HPDC alloy, less than 0.1% of Cu is added.

Magnesium is commonly added to commercial Al-Si alloys, typically at addition levels of <1%**.** The presence of Mn can reduce the solubility of Fe and Si in Al and alter the composition and morphology of the Fe constituent phases. For example, a Mn addition favours the formation of intermetallics such as $Al_{15}(Fe,Mn)_3Si_2$ rather than the $Al_9Fe_2Si_2$ type. The $Al_{15}(Fe,Mn)_3Si_2$ intermetallics is typically cubic in structure, and as a result

gives improved mechanical properties (Fig. 2.9) (Fang *et al.* 2007). Mn additions also improve the elevated temperature properties of the Al-Si alloys.

2.2.3 Microstructural control

The Al-Si alloys are categorized into three categories based on the concentration of Si. These are hypoeutectic (<12.7%Si), eutectic (around 12.7%Si), and hypereutectic (>12.7%Si). The hypoeutectic alloys solidify with primary α-Al followed by the Al-Si eutectic. The hypereutectic alloys solidify in similar manner, but Si, not α-Al is the primary phase in these alloys. The microstructure of the eutectic structure in an Al-Si eutectic alloy is shown in Fig. 2.8.

The solidification mechanism is explained by how homogeneous nucleation occurs in an idealised pure material, where the only source of nucleation, in an undercooled melt, is due to fluctuation phenomena (Auer and Frenkel 2001, Kurz and Fisher 1998). On the other hand, *heterogeneous* nucleation occurs in "impure" materials, where walls or some agents, usually particles substantially larger than the atomic scale introduced in the melt (either intentionally or not) facilitate nucleation by reducing the energy barrier to the formation of the stable phase (Warren *et al.* 2009). Heterogeneous melting can be explained by the thermodynamic relation between the interfacial energies, $\gamma_{sv} \geq \gamma_{sl} + \gamma_{lv}$, where *s* ,*l* and *v* stand for solid, liquid, and vapour phases, respectively. The decrease in the total (interfacial) energy is the cause for heterogeneous melting.

Homogeneous and *heterogeneous* nucleation can be explained by the Vollmer and Weber (1925) theory. In pure metal solidification, the critical nucleation size for survival is described by:

$$r^*_{\text{hom}} = \frac{-2\gamma_{sl}}{\Delta G_v} \tag{2.9}$$

The free energy barrier given by:

$$\Delta G_{\text{hom}} = \frac{16\pi\gamma^3_{sl}}{3\Delta G^2_v} \tag{2.10}$$

where, ΔG_v is the driving force for solidification in heterogeneous nucleation, the critical nucleation size is described by Eq. 2.9 and the free energy barrier is:

$$\Delta G_{\text{hom}} = \frac{16\pi\gamma^3{}_{sl}}{3\Delta G^2{}_v} f(\theta), \tag{2.11}$$

where $f(\theta)$ is a function of the contact angle, θ is the contact angle on the substrate on which nucleation takes place.

During the solidification of a hypoeutectic alloy, grains and/or particles form and this structure can be refined to equiaxed grains and fine particles by two main approaches, namely (i) chemical modification, which produces a fine grain structure through the addition of trace-levels of several elements, such as Al-Ti-B and Al-Ti-C, and research is continuing for Al-Sc grain refiners, Al-Zr and Al-Cr are also capable of grain refinement of primary α-Al grains in hypoeutectic Al-Si alloys (Quested 2004a, Quested 2004b) and Al-P, Cu-P, Al-Cu-P, and Al-Fe-P for primary Si particles in hypereutectic Al-Si alloys (Faraji 2005, Jiang 2005, Kyffin 2001, Zuo 2009); and (ii) physical grain refinement through the externally applied force to induced fluid flow during solidification in order to refine the grain size, such as rotation of the mould, mechanical or electromagnetic stirring of melt, and rheomixing (Fan 2002).

For primary Si refinement, in Al-Si hypereutectic alloys, Al-P master alloys are commonly used. According to the literature (Faraji 2005, Jiang 2005, Kyffin 2001, Zuo 2009), Al and P elements dissolve in the melt and during the solidification, as the temperature decreases, AlP intermetallic particle precipitate. Than these AlP intermetallic particles nucleates Si with a cube–cube orientation relationship and result in fine faceted Si particle in the solidified microstructure. Due to the similar lattice parameters, AlP intermetallic particle is considered as an excellent refiner for primary Si phase in Al-Si hypereutectic alloys.

In addition, mechanical properties of Al-Si alloys directly relate to the size and shape of the eutectic Si flakes and primary Si phases (Elliott 1984, Makhlouf and Guthy 2002). In hypoeutectic Al-Si alloys, coarse eutectic Si flakes give low strength and poor ductility. Chemical and physical refining methods can be used to modify both the eutectic and primary Si. Chemically Si particles are modified by the addition of several elements from

the periodic table groups IA and IIA and the lanthanide series (Makhlouf and Guthy 2002). However, sodium and strontium are widely accepted by the scientific community. The addition of small quantities (0.005-0.015%) of sodium to the melt modifies the eutectic Si (Elliott 1984). However, controversy still remains about whether the sodium effect is on the nucleation and/or growth of the eutectic. The literature shows that sodium may depress the eutectic temperature by about 12 °C, which allows obtaining a finer microstructure by giving a higher rate of nucleation in the undercooled condition. As the sodium affects the fluidity and disadvantages a caused by the rapid loss of the element by evaporation or oxidation. The addition of strontium at about 0.03-0.05% is achieved by Al-Sr or Al-Si-Sr master alloy. The strontium effects the nucleation and restricts the growth of the eutectic Si flakes. A second approach to refine the eutectic Si and primary Si phase is physical refining by applying external force and many processes such as ultrasonic treatments (Kotadia *et al.* 2010).

In recent years, mechanical refiner, including ultrasonic, electromagnetic mixing and mechanical vibration has been successfully developed and applied to refine primary Si particles and eutectic Si flakes. In ultrasonic technique, the compression and relaxation of high frequency ultrasonic wave have effect on melt. The transient cavitations could produce an impact strong enough to break up the clustered fine particle and disperse them to more uniformly in entire matrix without forming any clusters. In addition, acoustic cavitations accelerated the heat and mass transfer processes such as diffusion, dispersion, emulsification, etc., which would helps local undercooling during the solidification and further helps to refine primary Si particles (Das and Kotadia 2010).

2.2.4 High Pressure Die-Casting process

Doehler (1910) was among the first to patent die casting-related technology. High pressure die-casting (HPDC) is a process in which molten metal is injected into a precisely dimensioned steel mould, within which pressure is maintained until solidification has been completed. It offers good surface finishing of components with accurate dimensions. The initial machines produced Al castings in re-usable metal moulds, where a manually powered pull bar transmitted the force required to fill the mould. In 1927, the horizontal cold chamber die casting machine was developed, which represents the basis of today's technology (Laukli 2004). The HPDC process is mainly

used for four principal metals with different alloy compositions which are: Al, Mg, Cu and Zn. This process has been developed to meet the demands of industries for efficient production and low cost (Street 1986). The global production of Al and Mg casting alloys has therefore increased, and the consumption of Al concurrently exceeds the existing production capacity of the primary metal. It is therefore necessary to exploit, or invent, economically sustainable processes that can give light-weight products with integrated functions that fulfil the requirements for recycling and fuel consumption regulations. HPDC is well suited for those demands. In industry, this is a fully-automatic, large-volume, high-productivity process for the production of complex, thin-walled, near-net shape castings, with part weights ranging from a few grams to 40 kg or more (Street 1986).

In the HPDC process the short die filling time and thin walls provides high cooling rates (typically 100-1000 Ks^{-1}) (Lauki *et al.* 2002) for solidification. This promotes a fine grain size which provides decent mechanical properties. In addition, the properties can be improved by intimate interrelationship between the product and process design through amended metal handling, accurate process control, and optimized runner and die design. Furthermore, suitable timing, good dimensional stability and a correct assessment of the fluid and heat flow are pre-requisites for better castings. Apparently minor factors such as the amount of lubrication, its composition and application procedures can turn out to be of the utmost importance for the final casting characteristics. However, the microstructures formed by HPDC process are very complex. It is influenced by many factors associated with liquid and semi-solid melt processing, flow, and heat transfer phenomena (Dahle and StJohn 1999, Dahle *et al.* 2001, Gourlay *et al.* 2007, Helenius *et al.* 2005, Laukli *et al.* 2005).

2.3 Summary

The topics discussed in this chapter provide the background for the study in this thesis. First, we have reviewed solidification, and the different phenomena for segregation and application of immiscible alloys. It is well known that it is important to have a uniform distribution of the minority phase during the solidification of immiscible alloys. The importance of an understanding of solidification and the distribution of the minority

phase by using a melt conditioning by advanced shearing technology (MCAST) unit will be discussed in detail in later chapters 4 and 6. In addition, we briefly reviewed advanced processes, and the application, and requirements of immiscible alloys. Second, we described the Al-Si high pressure die-casting (HPDC) process and the effect of different alloying elements on the morphology of Al-Si based die cast alloys. Detailed results and discussion will be given of the experiments performed here in chapters 5 and 6.

Chapter 3
Experimental Techniques and Procedures

3.1 Introduction

In this chapter, the procedure for preparation of the Al alloys, for alloy processing by the MCAST (melt conditioning by advanced sheared technology) unit, different gravity casting processes, characterisation and mechanical property measurement techniques will be presented.

3.2 Materials preparation

In this study different Al alloys, as given in Table 3.1, have been used to investigate the intensive shearing effect on the solidification process and microstructural evolution. Among them, the first set consisted of the following two ternary Al-Sn-Cu bearing alloy compositions (in wt. %):

- Al-20Sn-10Cu
- Al-30Sn-10Cu
- Al-45Sn-10Cu

These alloys were prepared from commercially pure Al and 99.99 wt. % pure Sn and Cu.

The second set of experiments were performed on three different Al-Si based cast alloys with the following compositions (in wt. %),

- Al-9.4Si (LM24)
- Al-10.3Si (Silafont)

- Al-14Si

In this second set of alloys, Al-9.4Si (LM24) and Al-10.3Si (Silafont) alloys were supplied by *Norton Aluminium Ltd.* and the Al-14Si alloy was prepared in the laboratory from a commercially pure Al ingot and an Al-50Si master alloy.

All the alloys were prepared in clay graphite crucibles using an electrical resistance furnace. The furnace was set approximately to a temperature ~150 °C above the melting temperature of the alloy and was held isothermally for ~2 hours with intermediate stirring at regularly intervals to ensure chemical homogeneity before being cast for chemical composition analysis and/ or further investigation. Depending on the requirement of the experiments, such as mould size, number of samples, various processing parameters, the quantity of the melt was varied from 100 gm to 18 kg.

To avoid die sticking problem in HPDC experiments, it is important to note that a few cast alloys compositions were modified by the addition of Fe up to 0.5wt.%. The iron was added in the form of an Al-46Fe master alloy addition, supplied by *KBM Affilips Ltd*, Alcester, UK.

Table 3.1. Alloy composition (wt.%)

				1st set of Alloys					
Al-20Sn-10Cu	20Sn	10Cu							Al Rem
Al-30Sn-10Cu	30Sn	10Cu							Al Rem
Al-45Sn-10Cu	45Sn	10Cu							Al Rem.
				2nd set of Alloys					
Al-9.4Si (LM 24)	9.38Si	0.80Fe	2.31Cu	0.26Mn	0.49Mg	1.02Zn	0.05Ti	0.001B	Al Rem.
Al-10.3Si (Silafont)	10.26Si	0.21Fe	0.03Cu	0.51Mn	0.30Mg	0.03Zn	0.06Ti	0.001B	Al Rem.
Al-14Si	14 Si	0.01Fe							Al Rem.

3.3 Melt conditioning by advanced shear technology (MCAST) unit

The recently developed 'MCAST' machine is an in-house development at BCAST, *Brunel University, UK*, patented by a research group lead by Prof. Fan (Fan *et al.* 1999). The melt conditioning unit consists of specially-designed profiles of closely intermeshing screws, which are self-wiping and co-rotating as shown in Figs. 3.1 and 3.2. The screws deign allow liquid melt lifting into the barrel. The flow inside the MCAST unit is characterised by a high shear rate and a high intensity of turbulence which ensures powerful dispersive mixing at a very fine level. The highly intensive shear also provides a uniform temperature and chemical composition and well-dispersed nucleation sites in the melt. An intermediate shear rate, $\dot{\gamma}$, is found in the gap between the tip of the screw flight and barrel surface, and is given by the following equation:

$$\dot{\gamma} = N\pi\left(\frac{D}{G} - 2\right) \tag{3.1}$$

where N is the rotation speed of the screw, D is the outer diameter of the screw (36 mm), and G is the gap between the screw flight and barrel surface (1 mm). The twin screw process capacity is about 1 Kg and screw barrel diameter and length are 100 mm and 740 mm, respectively. Tabulated in Appendix-I are the shear rates as a function of rotation speeds. A detailed explanation of fluid flow in the MCAST unit is described elsewhere (Fan 2002, Ji *et al.* 2001, Tang 2003a, Tang *et al.* 2003b). The combination of MCAST and HPDC is called MC-HPDC. It should be noted that the HPDC process gives high cooling rates (up to ~1000 Ks^{-1}) (Gourlay *et al.* 2004). The fluid inside the MCAST machine is subjected to a cyclic variation of shear rate due to the continuous change of the gap between the screws and barrel. The exact shear rate cannot be calculated due to the complexity of the screw geometry but based on the viscous flow, the shear stress between the screw and the barrel can be estimated from the following equation (Rauwendaal 1994):

$$\tau = \eta N\pi\left(\frac{D}{G} - 2\right) \tag{3.2}$$

where η is the viscosity of the slurry or liquid melt.

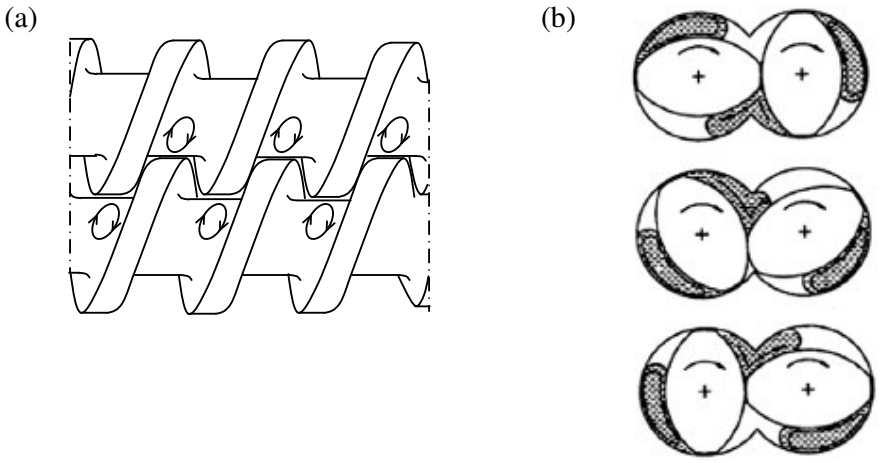

Fig. 3.1. Schematics illustration the fluid flow of twin-screw process (a) longitudinal view and (b) transverse view.

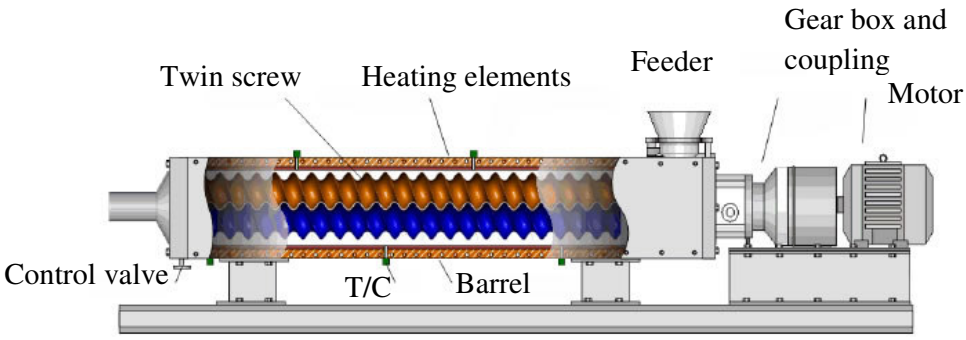

Fig. 3.2. Schematic illustration of the MCAST (melt conditioning by advanced shearing technology) unit.

Experimental procedure for the MCAST process:

a) Melt was prepared in a large graphite-clay crucible and was manually stirred to maintain homogeneity. Initially, an appropriate amount of melt was taken from this crucible and its temperature was monitored prior to pouring the liquid metal into the MCAST unit at the required pouring temperature.

b) Melt was poured into the inlet of the MCAST unit whilst the screws were rotated at the required rotations per minute.

c) After completing the shearing process at a given shearing rate, time and temperature, a transfer valve was opened and the conditioned melt was discharged into the casting mould or HPDC. During the operation MCAST unit set at 15° to the HPDC shot sleeve for transferred slurry to the HPDC machine.

The main aim of the application of the MCAST process for processing immiscible alloys is to use intensive shearing to disperse the Sn-rich phase in the matrix which would lead to a homogeneous dispersion throughout the conditioned melt. Based on numerical modelling, a detailed explanation about droplets breaking down through the intensive shearing is explained elsewhere (Tang 2003a, Tang *et al.* 2004, Tang and Wrobel 2005a, 2005b, Tang *et al.* 2006). In the case of Al-Si alloys, the intensive shearing process was used to produce fine and homogeneous microstructures by providing a uniform temperature and chemical composition through very high level of shearing and turbulence forces. In Table 3.2 reported twin-screw experimental operation condition.

Table 3.2. MCAST experiments operating condition. Note that the all experiments were carried out without using any protective gas.

Alloy	Pouring temperature (°C)	Barrel temperature(°C)	Screw rotation time (s)	Screw rotation speed (rpm)	Liquid volume (gm)
Al-20Sn-10Cu	650	600	60, 120, 180	200,400,600,800	750, 500
		590	60, 120, 180	200,400,600,800	750, 500
		585	60, 120, 180	200,400,600,800	750, 500
		580	60, 120, 180	200,400,600,800	750, 500
Al-30Sn-10Cu	650	580	60	800	750
Al-45Sn-10Cu	650	585	60, 120, 180	200,400,600,800	750, 500
		558	60, 120, 180	200,400,600,800	750, 500
		545	60, 120, 180	200,400,600,800	750, 500
		535	60, 120, 180	200,400,600,800	750, 500
Al-9.4Si (LM 24)	660	650	60	500	750, 500
		635	60	500	750,500
		615	60	500	750,500
		600	60	500	750,500
Al-10.3Si(Silafont)	660	650	60	500	750,500
		640	60	500	750,500
		630	60	500	750,500
		620	60	500	750,500
		610	60	500	750,500
		600	60	500	750,500
		590	60	500	750,500
Al-14Si	660	650	60	800	750
		640	60	800	750
		630	60	800	750
		620	60	800	750
		610	60	800	750
		600	60	800	750
		590	60	800	750

3.4 Casting processes

Various casting processes were used to produce ingots, samples for microstructural analysis, shaped samples for mechanical tests and for the purpose of comparing results. The types of moulds used to obtain samples for preliminary studies include: a steel mould for ingot casting after preparing exact amounts of alloys; a cylindrical shaped steel mould and wedge shaped copper mould (to understand solidification and the effect of cooling rate on segregation), TP-1 mould, shrinkage mould, and high pressure die-casting (HPDC) mould. All these processes were conducted with an aim of understanding the solidification paths in various alloys.

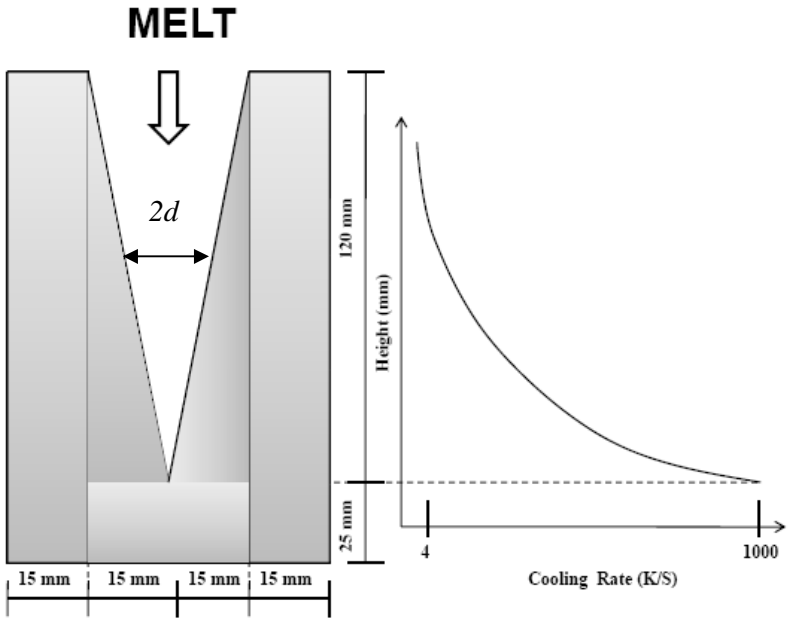

Fig. 3.3. Schematic illustration of the Cu wedge mould, showing the dimensions and typical cooling rate as a function of height of the mould.

3.4.1 Copper mould

The main objective for using a wedge shaped copper mould was to investigate the cooling rate effect on the size and distribution of the Sn-rich droplets. From the temperature and time measurements, the cooling rates throughout the solidification temperature range were determined at the measurement positions. An empirical

relationship between the cooling rate ($\dot{T}$ in Ks^{-1}) was then plotted as a function of height (Fig. 1), and the following empirical relationship was found (Pryds and Huang 2000):

$$\dot{T} = \frac{926\,(\mathrm{K\,mm^2}/s)}{d^2} \tag{3.3}$$

where *d* stand for the half thickness of mould cavity. The cooling rate at the tip of the mould is approximately 1000 Ks^{-1}. The cooling rate as a function of height has been experimentally measured by placing thermocouples at various points along the wedge and measuring their respective cooling curves.

3.4.2 High Pressure Die-Casting (HPDC)

As discussed in chapter 2, the high pressure die casting (HPDC) process is well established and widely used as a rapid manufacturing technology especially in the automotive industry. The HPDC machine used in this study was manufactured by *L.K. Machinery Co. Ltd., Hong Kong*. A schematic diagram of the cold chamber high pressure die-casting machine is shown in the Fig. 3.4. The diameter of the plunger was 60 mm, and it has a maximum shot speed of 6.22 ms^{-1}. In this investigation, 60% of the maximum slot pressure and pressure onset position were kept constant at 120 bar and 200 mm, respectively. The dies were clamped at a load of 280 tons and pre-heated using 8 cartridge heaters embedded symmetrically inside the two halves of the die block providing a uniform temperature across the die-cavity. A thermocouple was also embedded inside the die block to feed the heating controller unit on the machine with a temperature reading and an external thermocouple was used to measure the temperature of the die-cavity surface prior to any casting. The processing parameters of the HPDC process are given in Table 3.3.

The melt for the die-casting was prepared at the required temperature and die heating was switched on and the procedure for the die casting operation was in the sequence of:

a) Die surfaces were cleaned of any material left over from previous casting runs and coated with lubricant (graphite + oil) to aid ejection of cast samples.

b) Using a preheated clay-graphite crucible, an adequate amount of melt was taken from the melt crucible and poured into the shot sleeve at the desired temperature measured by an external thermocouple.

c) Prior to pouring into the shot sleeve the dross is removed from the liquid metal.

d) The machine was activated to apply the shot according to the set profile of the plunger speed, position and pressure. The machine automatically runs through the cycle of; injection, intensifying, dwell (while the casting fully solidifies), and finally ejects the cast component.

The intensifier was set to trigger at a pressure drop of 65% with an intensifying pressure of 70 bar and with a 30-45 s dwell time until ejection. The cast pre-form produced is shown in Fig. 3.5 which consists of two tensile samples and two fatigue samples along with the runner system.

Table 3.3. 280 tonne cold chamber HPDC process parameters used for each alloy.

Feeding pressure	Intensive pressure	Pressure trigger	Filling time	Die temperature	Cooling time	Releasing time
84 bar	119 bar	70 bar	3 s	220 °C	30 s	30 s

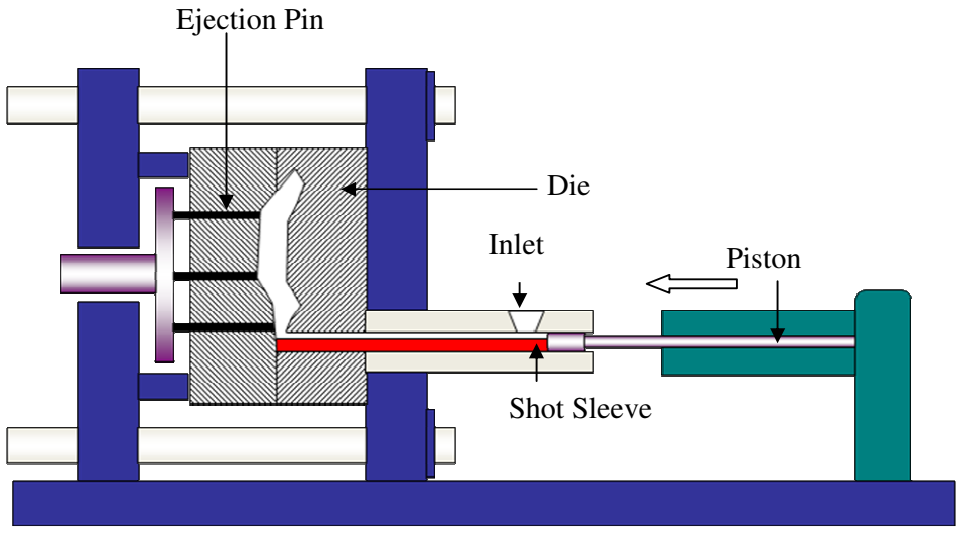

Fig. 3.4. A schematic illustration of the 'high pressure die-casting' (HPDC) machine.

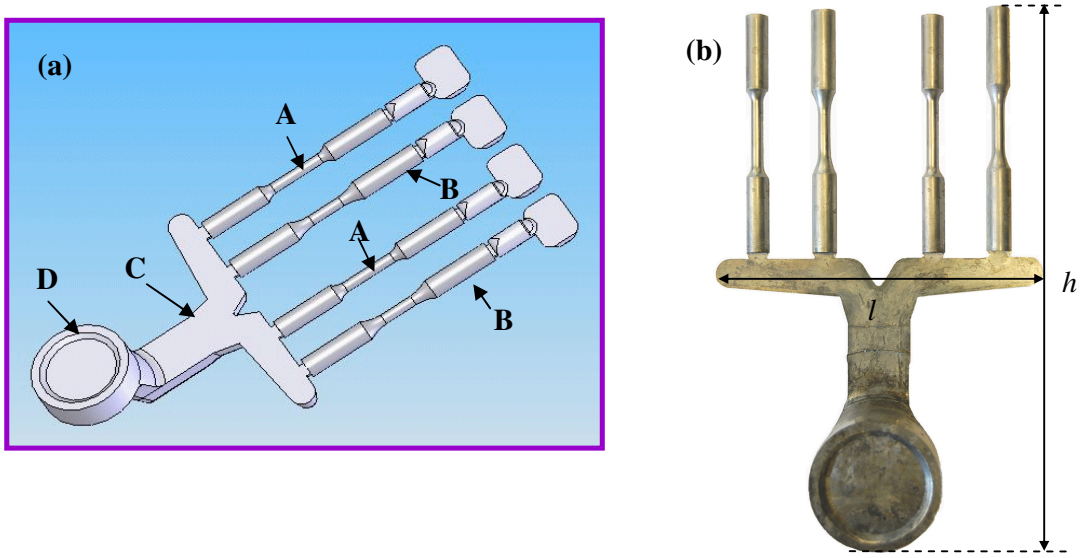

Fig. 3.5. (a) Schematic illustration of a die-cast component with runner system produced from the HPDC machine and (b) Al-Si alloy die-cast component, (A) Tensile sample (diameter 6.4 mm), (B) Fatigue sample (diameter 6.3 mm), (C) Runner, and (D) Biscuit. Full dimension of test specimen is 23 cm length (*l*) and 32 cm height (*h*).

3.4.3 Test Procedure -1 (TP-1) mould

The grain size for a given alloy depends on the cooling rate. In order to study the grain size for a given alloy as a function of various processing parameters, it is important to keep the cooling rate constant. To maintain a constant cooling rate, a standard test procedure-1 (TP-1) mould technique was used. The experimental steps are as follows:

a) The alloy was melted in the electrical resistance furnace at ~150 °C above its melting temperature and was held for 2 hours to homogenize the melt
b) The TP-1 mould ladle (Fig. 3.6) was placed in the oven for preheating to 350 °C.
c) The prepared melt was stirred using a graphite rod for 30 s and poured into the TP-1 mould ladle at the desired temperature and then placed on a quench tank until final solidification was complete.
d) The water flow rate in the quench tank was set at 3.8 l/min. This flow rate resulted in 25 mm submersion from the bottom of ladle.

e) For the purpose of the microstructural examination: A test sample was removed from the TP-1 conical mould and was cut according to the standard procedure (38 mm above the base) as illustrated in Fig. 3.6a. The cooling rate at this position corresponds to 3.5Ks^{-1}.

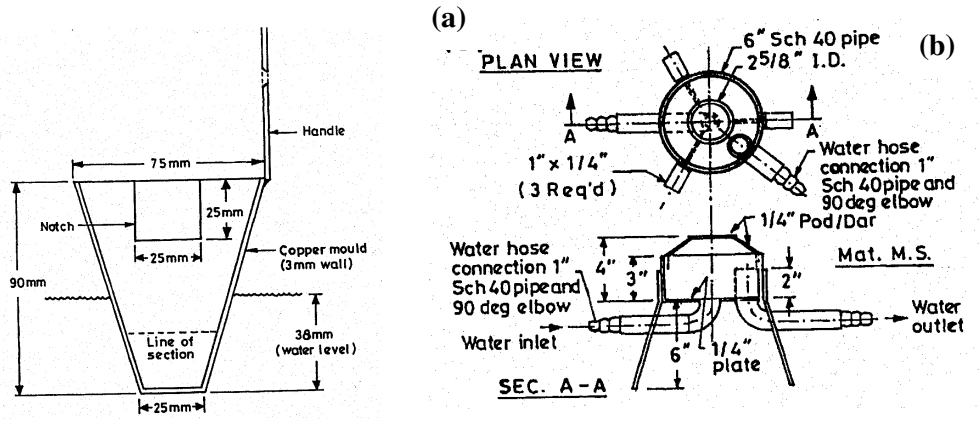

Fig. 3.6. Schematic illustration of TP-1 grain refining test moulds (a) ladle (b) plan and side view of mould design (Aluminium Association 1987).

3.4.4 Shrinkage mould (Tatur test)

To study the effect of melt conditioning on the shrinkage of Al-9.4Si alloy, a Tatur test mould was utilised (Fig. 3.7). The mould parts were pre-heated in a furnace at 300 °C and reassembled on a hot plate which was also heated at 300 °C. The melt was poured at the chosen pouring temperature and allowed to solidify. Three different types of porosity can be measured from a Tatur test. Fig. 3.8 shows the three different types of porosity in a prepared Tatur test sample. The detailed calculations regarding the shrinkage porosities are explained in Appendix-II.

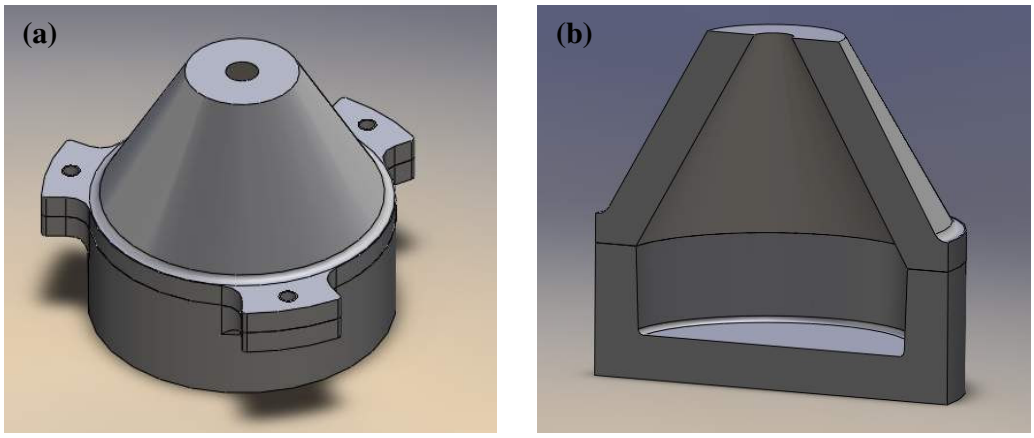

Fig. 3.7. Tatur shrinkage mould (a) assembled (b) cross section

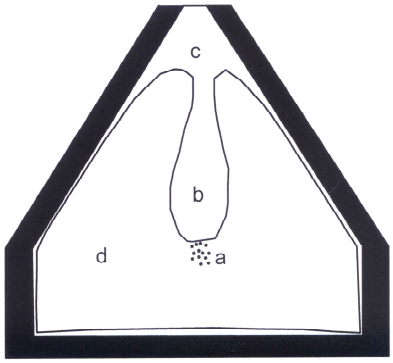

Fig. 3.8. Sketch showing three different types of porosity present in the sample cast in Tatur mould (a) micro-shrinkage cavities, (b) macro-shrinkage pipe, (c) slumping and contraction, and (d) casting.

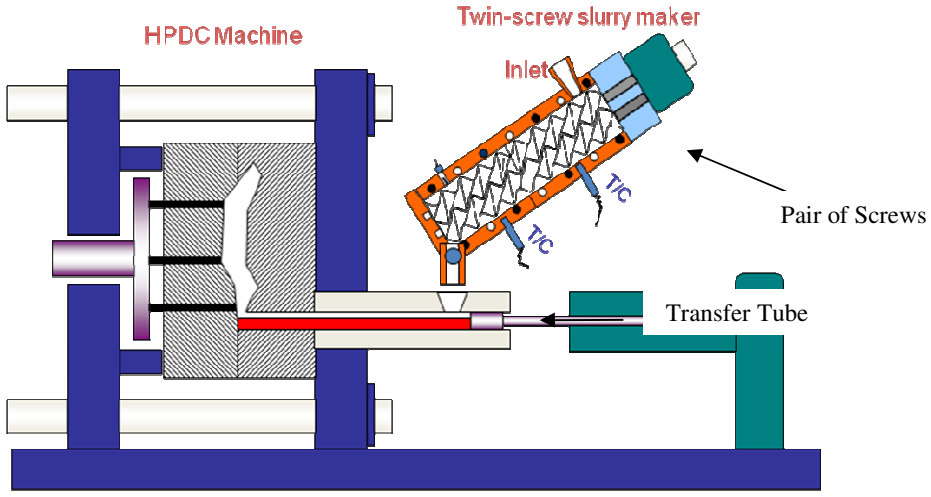

Fig. 3.9. Schematic illustration of the MC-HPDC process.

3.5 The 'Melt Conditioned High Pressure Die-Casting' (MC-HPDC) process

The 'melt conditioning high pressure die-casting' (MC-HPDC) process is a combination of the MCAST unit and the 'high pressure die-casting' (HPDC) process (Fig. 3.9) (described in section 3.3 and 3.4.2, respectively).

The MC-HPDC processing conditions are tabulated in Table 3.2 and experiment was carried out without using any protecting gas. The MCAST unit is adapted to receive liquid alloy through an inlet located towards one end and to discharge well conditioned alloy or semi-solid slurry through an outlet located at the other end. The barrel of MCAST unit is made of a few separate zones. The temperature control of each individual zone is achieved by balancing the heating power input by a central control unit, giving rise to a control accuracy of ± 1°C in the barrel. The thermocouples in each zone are fitted in the barrel liner perpendicular to its axis ensuring the nearest temperature reading of the inside. Thermocouples are also fitted on the feeder and the transfer valve area. The MCAST unit is connected to the 'high pressure die-casting' machine via a heated steel transfer tube which is shown in Fig. 3.9. The transfer tube is heated to the same temperature as the processing temperature set in the "twin-screw". A discharge time of 5-7 s allows the liquid or semi-solid slurry produced from the MCAST unit to flow along the heated transfer tube and accumulate in the shot sleeve of the HPDC machine, before applying the plunger to cast a component. The MC-HPDC process allows the slurry produced from the MCAST to be cast into any component or shape. In this work, the liquid and semi-solid slurry was cast in the same manner, as shown in Fig. 3.9.

The central control unit consists of temperature controls for all the heating zones, a dial to indicate screw rotations per minute (rpm), a torque reading of the screws, a timer, and switches for opening and closing the transfer valve. The rotation speed of the screws can be set at the desired rpm with the desired running time until discharge of the alloy melt. The entire sequence can be set on an automatic mode, including opening and closing of the transfer valve where the discharge time can also be set. The MCAST unit heaters are switched on and set to the preferred temperature. It takes about 3 hours for the machine to reach the set temperature from room temperature. The transfer tube is heated to the same temperature as the processing temperature set in the MCAST unit. The conditioned

alloy melt is directly discharged in the shot sleeve of the HPDC machine, before applying the plunger to cast a component.

An electronic connection between the control panel of the MCAST machine and that of the die caster allows the operation to be fully automated, from pouring the conditioned alloy melt into the MCAST machine to the ejection of the component after die-casting. The cycle time of the entire experiment is mainly dictated by the shearing time allowed in the MCAST machine and dwell time allowed for complete solidification of the die-cast component during the die-casting process. The discharge time is dependent on the amount of melt processed inside the MCAST machine. In current study, all experiments carried out under without using any protective gas.

3.6 Characterisation methods

3.6.1 Chemical composition analysis

It is essential to check chemical composition of prepared alloys to verify whether their composition is close to that of the targeted composition. In this work chemical composition for all alloys was analysed using a "Worldwide Analysis System (WAS) AG, Foundry master". A spark is produced on the surface of the sample to allow the surface to emit photons, which are detected by the optical spectrometer. This has a reciprocal relationship to wavelength. A detailed explanation about "spark source spectrometry" is given in Gill (1997). A spectrometer is used for producing spectral lines and measuring their wavelengths and intensities. WASLAB software compares the measured data with standard data and gives the final results in wt.% of chemical compositions. To produce flat surfaces for this analysis, samples were polished with 120 grit SiC paper. Several tests were performed on a single sample and an average result was recorded as the final composition. Prior to measurements, a calibration procedure was performed using a standard test piece and CITZAF correction package.

3.6.2 Sample preparation for metallographic studies

Samples for microstructural examination were cut from the solidified castings and were mounted in Bakelite. The mounted samples were ground using SiC abrasive papers with

various grits (120, 800, 1200, 2400 and 4000). Samples of Al-Sn-Cu alloys were polished with a 0.25 μm diamond suspension and all other alloys were polished with a silica suspension.

3.6.3 Optical microscopy (OM)

The microstructures, either with or without etched surfaces, were observed using a Zeiss Optical Microscope (OM) equipped with a digital camera and a computer. A software application "Axioshop 2 MAT0" was used to acquire images from the camera and to perform image analysis. The microscope was sufficient to measure topographic parameters such as grain size, shape factor, volume fraction etc.

In the bright field (BF) mode, a polished surface appears bright in contrast and the surface irregularities such as grain boundaries appear dark in contrast. The reason for grain boundaries and intermetallics appearing dark in contrast, is that the intensity of the reflected light is reduced due to light scattered from grain boundaries and the interfaces between intermetallics and matrix.

Plane polarised light (PP) is most commonly used for measuring the grain size. PP is achieved by inserting a polarising filter into the incoming light path. This filter suppresses the wave component vibration in all directions except in one direction, which corresponds to that of the filter orientation. PP light reflects from the samples (differently orientated grains) with doubly reflecting waves, which produced individual wave components. These components are different and vary with the propagation direction through the sample. This enhances the contrast and the quality of the image. This characterisation technique has been used in this study for quantitative metallographic analysis.

3.6.4 Scanning electron microscopy (SEM)

A scanning electron microscope (SEM) is in principle a microscope with an electron beam scanning back and forth over a sample. Due to the interaction between the beam and the sample several different signals are produced providing the user with detailed information about the surface structure, differences of atomic number within the sample or information about the elemental content (Goodhew *et al.* 2001). A signal is measured

individually from each point, with the use of advanced detectors, which collects a range of X-rays and electrons from different depths of the surface. The SEM used in this study has primary electron imaging, secondary electron imaging or back scattered electron (BSE), and energy-dispersive X-ray analysis (EDX) operational modes.

Some of the samples used for optical microscopy were subsequently carbon-coated and examined in a JEOL model JXA-733 SEM. The advantage of SEM over optical microscopy is the large depth of field and higher resolution, thus producing high resolution images at high magnification (up to 50,000 times).

3.6.5 Differential scanning calorimetry (DSC)

Differential scanning calorimetry (DSC) is a thermal analyses method. DSC is a technique for measuring the energy necessary to establish a nearly zero temperature difference between a substance and an inert reference material, as the two samples are subjected to identical temperature regimes in an environment heated or cooled at a controlled rate. In DSC, the sample and reference are connected by a low resistance heat flow path (a metal disc). The assembly is enclosed in a single furnace. Enthalpy or heat capacity changes in the sample cause a difference in its temperature relative to the reference; the resulting heat flow is small compared with that in differential thermal analysis because the sample and reference are in good thermal contact. The temperature difference is recorded and related to the enthalpy change in the sample using calibration experiments.

The phase transition temperatures of Al-Sn-Cu alloys were investigated using a DSC (NETZSCH STA 409PC instrument). The temperature range was from 200 to 700 °C. Various scanning rates from 1-20 K/min were employed and both heating and cooling processes were tested. Each sample mass was between 15-20 mg, which was placed in an alumina crucible (12.5 mm outer diameter and 7.5 mm height) with an Ar flow for testing in order to avoid oxidation. Each alloy was tested three times with different scanning rates.

3.6.6 Electro-etching

After polishing samples as described in section 3.6.2, they were cleaned in an ultrasonic bath for 20 minutes to remove dirt from the sample surface and then electro-etched in Barker's etching reagent (7 ml HBF_4 48%, 93 ml H_2O) at 20 V for 70 s using a stainless steel cathode (Fig. 3.10). Electro-etching was performed for set 2 alloys (described in section 3.2) to reveal the grain boundaries. An anodic film grows on Al alloys depending on the crystallographic orientation of the grains. After electro-etching, the surface topography of samples varies significantly from grain to grain thus resulting in brightness variation across grains. The variations in colour show differences in orientation between the grains under the plane polarised light mode in OM. Basically the colours arise from the interface and unbalanced reflection of certain wavelengths of light caused by thin anodic films on different morphologies of grain (Davis 1993, Zhou *et al.* 2008).

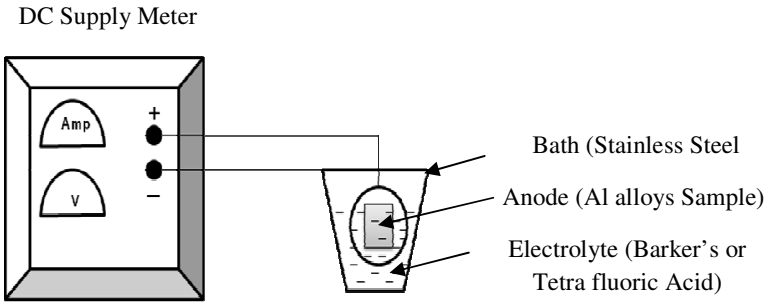

Fig. 3.10. Schematic showing the set-up of electro-etching unit.

3.7 Quantitative metallography

Quantitative metallographic analysis was carried out on OM images using image processing software Axioshop 2 MAT0. The equivalent diameter (d) and shape factor (F) of the grains/particles were calculated by:

$$d = \sqrt{4A/\pi} \tag{3.4}$$

$$F = 4\pi A / P^2 \tag{3.5}$$

where, A is the total area and P is the perimeter length of the grains/particles. When F is equal to 1, it represents a perfectly spherical grain/or particle. The grain size measurements were carried out on electro-etched samples using the simplest procedure

called the mean line intercept method (depicted in Fig. 3.11). The mean intercept length, $\bar{l}$, is then calculated from using equation:

$$\bar{l} = \frac{L_T}{N_i} \tag{3.6}$$

where L_T is the total length of the test lines and N_i the total number of grain boundary intersections on line L_T. The measured standard deviation from the average grain size measurements is considered as the "error" in grain size measurements (Kurzydlowski and Ralph 1995).

All grain diameters quoted are values of the mean linear intercept $\bar{l}$. The numerical model calculates the number of grains per unit volume N_v. In comparing experimental measurements with model predictions, the values of N_v and $\bar{l}$ are inter converted using (see Appendix-III):

$$N_v = \frac{0.5}{\bar{l}} \tag{3.7}$$

In the present study effort has been made to identify the influence of different processing variables on the resultant Sn and α-Al(Si,Mn)Fe particle distribution in the Al matrix. For a quantitative analysis of the distribution of the Sn and α-Al(Si,Mn)Fe particles, the simplest and effective, Quadrat method was used (Karnezis *et al.* 1998). The image to be studied was divided into a grid of square cells where the cell size (Quadrat size) was approximately twice the size of the mean area per particle (Curtis and McIntosh 1950). To minimize the edge effects, particles that are inside and in contact with the left and bottom side of each Quadrat were counted. Thus, particles on the Quadrat edge were not counted more than once. A schematic illustration of the Quadrat method is presented in Fig. 3.12.

In this method, the image to be studied was divided into number of square cells, the number of the particles per quadrant *Nq*, was measured (Fig. 3.12). The Quadrat method was performed on 15 images of different areas of each sample. Generally, five different regions from a large cast component were randomly selected for the microstructural and quantitative analysis. In mathematical terms a random, a spatial and a clustered spatial

distribution of particles can be expressed by a Poisson, a binomial and a negative binomial distribution respectively (Rogers 1974).

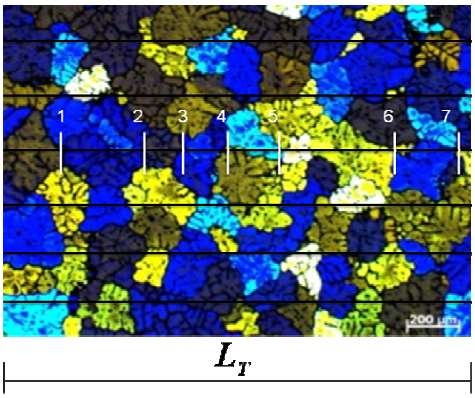

Fig. 3.11. Optical Micrographs under polarised light taken from an electro-etched sample.

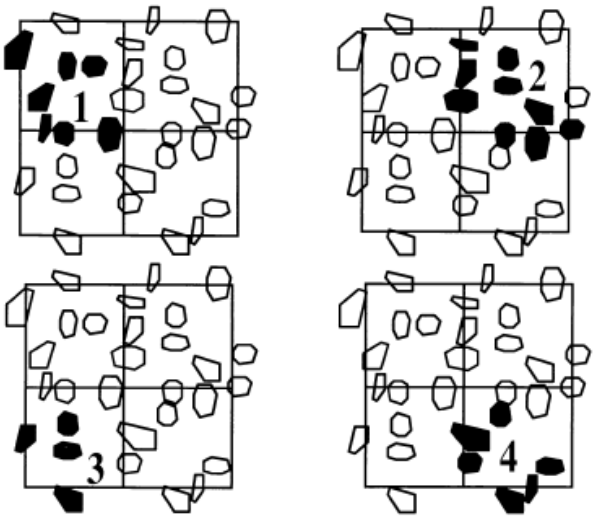

Fig. 3.12. Schematic representation of the Quadrat method, using four Quadrats. Particles counted are denoted in black (Karnezis *et al.* 1998).

3.8 Mechanical property tests and method

3.8.1 Hardness tests

Hardness is usually defined as the resistance of a material to plastic penetration of its surface. A Vickers indenter (Vickers hardness H_v) was used for measuring micro-hardness. The Vickers hardness test uses a square base diamond pyramid as the indenter.

The included angle between the opposite faces of the pyramid is l36°. The Vickers hardness values are calculated by the formula (Kuhn and Medlin 2000):

$$HV = \frac{2P\sin(\alpha/2)}{d^2} = 1.8544\left(\frac{P}{d^2}\right) \tag{3.8}$$

where P is the applied load in kg, and d is the diagonal length in mm. The indentation diameter was measured at two places at right angles to each other, and the average of the two readings taken. An average of at least 7 indentions was performed to obtain an average hardness. The microhardness was taken at a load of 0.2 kg and macro-hardness was measured at load of 20 kg.

3.8.2 Tensile tests

A die (as per ASTM standards) attached to the HPDC machine was used to produce tensile test samples. The dimensions of the test samples were 6.4 mm in gauge diameter, 25 mm in gauge length and 12 mm diameter in the grip section. The stress-strain curves were measured using an universal materials testing machine (Instron® 5569) at a cross head speed of 2 mm/min. (strain rate: 1.33×10^{-3} s^{-1}). The 'Instron® 5569' system was connected to a PC for automated testing and calculation of tensile test results such as yield stress, ultimate tensile strength and Young's modulus. The stress (σ) (calculated from the load) and strain (ε) (calculated from the extension) can either be plotted as nominal stress against nominal strain, or as true stress against true strain.

An external extensometer of 25 mm gauge length was manually attached to each test piece to get accurate elongation results. The yield strength was measured as the 0.2% proof stress on the stress-strain curve. All samples were tested at room temperature.

3.8.3 Heat treatment

Heat treatments, including controlled heating and cooling operations to achieve the desired microstructures and required properties were performed for set 1 alloy. An age hardening heat treatment was conducted to grow Al_2Cu precipitates inside the Al rich or Sn-poor matrix for the Al-Sn-Cu based immiscible alloys. The heat treatment temperature was selected as 200 °C (which is below the eutectic temperature).

Chapter 4
Rheomixing of Al-Sn-Cu Immiscible Alloys
Results

4.1 Introduction

The newly developed MCAST process was used to study solidification behaviour of ternary Al-Sn-Cu immiscible alloys. In order to better understand the solidification of Al-Sn-Cu alloys as well as their behaviour during MCAST processing two approaches have been combined. Computational thermodynamics has been used to identify alloys which are promising for the production of bearing materials using the MCAST process. This study includes thermodynamic calculations based on the results of previous work described elsewhere (Mickovic *et al.* 2008a, Mickovic *et al.* 2008b). By using the MCAST process, the two most promising alloys, Al-45Sn-10Cu and Al-20Sn-10Cu were successfully synthesized with well-dispersed microstructures throughout the entire volume of the samples. The influence of the viscosity of the system as well as the shear force on the nature of primary α-Al and Sn phase particles was investigated for these alloys. In this chapter we refer to “droplets” and “particles” as liquid phases and solidified liquid phases, respectively. The phase transformations of both alloys during solidification were also followed using differential scanning calorimetry (DSC), complementing the calculated results.

4.2. Thermodynamics of the Al-Sn-Cu system

Thermodynamic calculations are widely used in the development of new alloys for specific engineering applications and optimum processing conditions. From these thermodynamic calculations, much useful information can be obtained such as a phase diagram, thermodynamic properties, phase distribution, and phase composition.

4.2.1 Phase equilibrium in the Al-Sn-Cu alloys

A CALPHAD type study of the Al-Sn-Cu system has previously been performed by Mirkovic *et al.* 2008a. Recently, Mirkovic *et al.* (2008a) have critically assessed the *ternary* Al–Sn–Cu system. They studied the complex features of the Al-Sn-Cu phase diagram, dominated by ternary liquid demixing, using a combination of a CALPHAD thermodynamic modelling (Lukas *et al.* 2007) approach and DSC experimental studies as well as microstructural analysis. Their results showed that the addition of the third component, Cu, to Al-Sn alloys causes a pronounced liquid demixing, forming an isolated miscibility gap in the ternary system. It was also shown how seemingly small changes in alloy composition can result in drastically different microstructures. CALPHAD originally stands for CALculation of PHAse Diagrams. The "Calphad method" now means the use of all available experimental and theoretical data to assess the parameters of the *Gibbs energy* models selected for each phase (Lukas *et al.* 2007). To describe the use of these models and parameters stored in thermodynamic databases for various applications the term "computational thermodynamics" has been adopted. Such work in the Al-Sn-Cu system is presented in this chapter, and dealt with in section 4.2.2.

The Gibbs energy functions of all phases in the Al-Sn-Cu system have been determined using all available data in the literature as well as carefully-designed new experimental work by Mirkovic *et al.* (2008a). In order to rely on these functions for further calculations it is crucial that they are carefully checked for accuracy and reliability. The Gibbs energy functions can be used to calculate the ternary phase diagram as well as all thermo-chemical properties for each phase or for the system as a whole, for all compositions and temperatures.

Fig. 4.1a shows the calculated liquidus surface for the Cu-poor section of the Al-Sn-Cu alloy system. A large ternary stable liquid miscibility gap marked L′+L″ has developed from the metastable liquid miscibility gaps in both the Al-Sn and Cu-Sn binary systems. Alloys with an overall composition within the miscibility gap will separate into two distinct liquids upon cooling below a critical temperature (Fig. 4.1b). The L″ liquid is rich in Sn and therefore has a much higher density than the L′ liquid which is rich in Al. Upon further cooling these two-phase alloys will begin solidifying by precipitating an Al-rich solid solution, from both liquids. The solidification stages which then follow are discussed in chapter 6. Another set of alloys with a total composition lying within the region marked by grey shading on the liquidus surface, will first undergo precipitation of Al before the residual liquid reaches a composition on the surface of the miscibility gap, causing subsequent demixing. After demixing the solidification of L′ and L″ in these samples are similar to that of samples which experience primary demixing.

4.2.2 Semi-solid processing temperature and temperature sensitivity of solid fraction

Accurate evaluation of the temperature sensitivity (slope of the solid fraction versus temperature curve, $|dfs/dT|$) of the solid fraction (f_s) at a semi-solid processing temperature is a critical factor to ensure a wide and stable semi-solid processing window. This parameter controls the rheological behaviour and the evolution of the microstructure in the semi-solid state to a large extent (Tzimas and Zavaliangos 2000). The minor decrease in temperature can lead to a considerable increase in *fs*, and therefore a non-favourable microstructure for semi-solid processing due to inhomogeneous deformation and liquid segregation during mould filling (Patel 2005).

4.2.3 Solidification range

The solidification range is usually defined as the temperature range between the liquidus and solidus of a given alloy, $\Delta T_{L\text{-}S}$. A pure metal and a eutectic alloy are not suitable for semi-solid processing because of a lack of the solidification range. In contrast, alloys with a wide solidification range such as wrought alloys are also not suitable for a semi-solid process. The semi-solid freezing ranges ($\Delta T_{SS\text{-}S}$), defined as the temperature

difference between the semi-solid processing temperature T_{SS} and solidus T_S, play an important role in semi-solid processing. It should be 10 °C< ΔT_{SS-S} < 150 °C for good process ability and a high resistance to hot tearing (Wang *et al.* 1995).

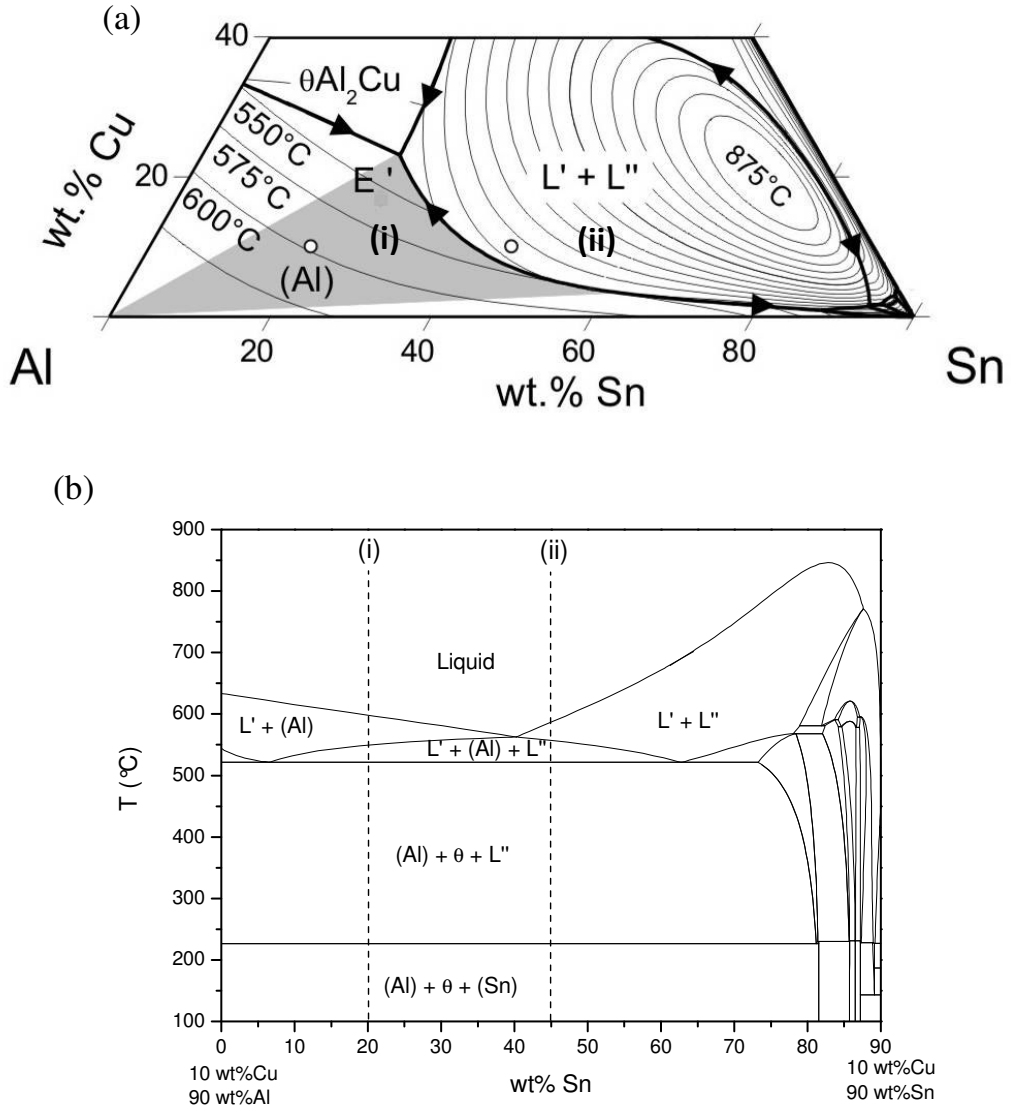

Fig. 4.1. (a) Cu-poor section of the calculated Al-Sn-Cu liquidus surface (Mickovic *et al.* 2008a) and (b) Calculated vertical section at constant 10wt.% Cu. Liquid phase notation is distinguished where appropriate, L′ = Al-rich and L″ = Sn-rich liquid and (i) and (ii) stand for Al-20Sn-10Cu and Al-45Sn-10Cu alloys, respectively.

4.2.4 Alloy selection using computational thermodynamics

Alloys should be identified which show promising properties for the production of Al-Sn-Cu bearing alloys using the MCAST process. These are alloys which undergo some demixing in the liquid phase so that soft Sn-rich particles can be found in a hard Al matrix in the final solidified microstructure. The exact amount of each phase present in the final microstructure strongly affects the mechanical properties of the alloy. For optimal processing using the MCAST unit, an alloy should be chosen with a relatively low temperature sensitivity of the solid fraction during cooling, i.e. a change in temperature over an easily controllable interval should invoke only a relatively small change in the solid fraction of the alloy. In this way the effective viscosity of the melt can be easily controlled and chosen for optimal processing. In order to explore the possible advantages of increasing the effective viscosity of the melt before demixing in the liquid phase begins, one alloy out of the grey area in Fig. 4.1a should be chosen which shows Al solid solution precipitation and then liquid demixing and one alloy with primary demixing, i.e. an overall composition within the miscibility gap in Fig. 4.1a. In addition, the alloy compositions should be selected for ease of processing using the MCAST unit. Based on the above consideration, the following two alloys have been selected for this work: Al-20Sn-10Cu and Al-45Sn-10Cu. These alloys have been marked (i) and (ii), respectively, in Figs. 4.1a and b.

Using Pandat^{TM} (Ref. Pandat 7.0, 2000-2007), a commercial software package for thermodynamic calculations, the solidification paths of a large range of alloys were investigated in order to find just a few alloys which fit all of the above criteria. The development of the phases present at each stage of solidification in the two chosen alloys can be seen in the ternary phase diagram section at 10 wt.% Cu shown in Fig. 4.1b. In this diagram, however, no information can be gained about the amount of each phase present, since the lever rule cannot be applied in such sections. The results of further thermodynamic calculations are shown in Fig. 4.2, where the phase evolution in the microstructure during cooling of the two chosen alloys is shown in the form of the calculated phase fraction as a function of temperature. These diagrams are best read from right to left, and the final phase distribution in the microstructure can be read from the left hand axes.

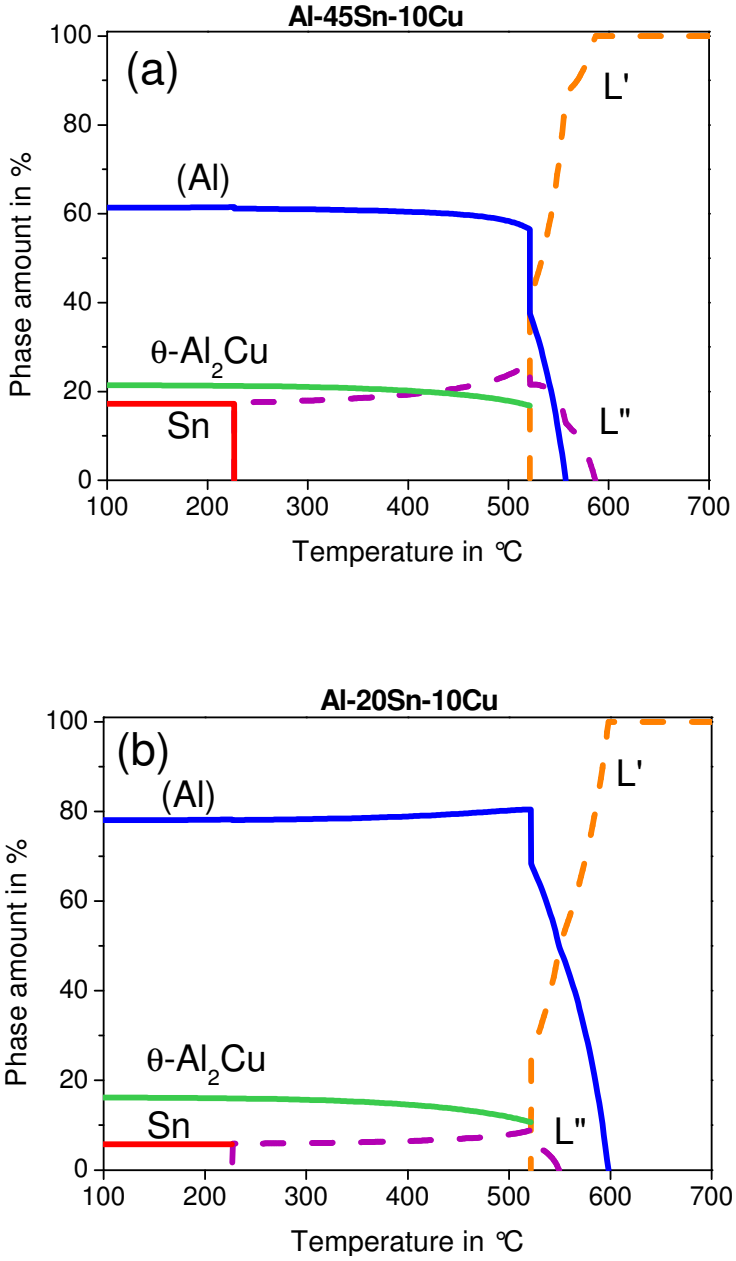

Fig. 4.2. Calculated equilibrium phase amounts (at.%) vs temperature (°C) for the samples (a) Al-45Sn-10Cu alloy and (b) Al-20Sn-10Cu alloy, calculated under Scheil conditions (100% mixing in the melt, no diffusion in the solid state, and local equilibrium at all phase boundaries).

The Al-45Sn-10Cu alloy (ii) lies within the liquid miscibility gap (Figs. 4.1a and b), and therefore shows primary demixing before the primary (Al) phase precipitates from the L′. This alloy shows a final amount of Sn of 17 at.% and the temperature sensitivity of the solid fraction during cooling is ~ 1 %/K. The Al-20Sn-10Cu alloy shows primary precipitation of (Al) before demixing and a final Sn fraction of 6 at.% and the temperature sensitivity of solid fraction is also ~ 1%/K.

4.3 Confirmation of the phase transformations with DSC

In this section the phase transformation of Al-45Sn-10Cu and Al-20Sn-10Cu alloys has been investigated by DSC (Differential Scanning Calorimetry). The alloys have been cycled with different heating and cooling rates between 1-20 K/min. and the DSC signal was measured in order to determine the phase transformation temperature. The main aim of the DSC studies was to determine the solidification path for Al-45Sn-10Cu and Al-20Sn-10Cu alloys.

The samples to be investigated by DSC have been prepared in an electric resistance furnace and cast at above a cooling rate of 1000 Ks^{-1}. In Fig. 4.3a, DSC curves for Al-45Sn-10Cu and Al-20Sn-10Cu alloys showing the various transitions are given as examples of the full processing cycle. In the insert of Fig. 4.3a, the calculated Al-Sn-10Cu phase diagram, and the transformations of the alloy during the DSC experiment can be followed along the vertical line at compositions of 20% and 45%Sn. The microstructures of Al-Sn-Cu alloys were analysed by SEM and OM. In the following the microstructural formation in each sample will be discussed with respect to the equilibrium solidification path which is also shown in the phase fraction diagrams in Fig. 4.2.

Finding the liquidus temperature and the demixing temperature for the Al-45Sn-10Cu alloy has been more difficult than that for the Al-20Sn-10Cu alloy. During cooling, when demixing occurs, liquid-liquid separation takes place instantaneously, because of the coalescence of the droplets of the minority phase. Then, the L′ phase solidifies and the L″ phase remains as a liquid phase at higher temperatures (>230 °C). Fig. 4.3b shows the signals of demixing for the Al-45Sn-10Cu alloy; which has been detected by

employing a slow cooling rate, 1K/min. Phase transformation temperatures of both alloys, measured by DSC are tabulated in Table 4.1.

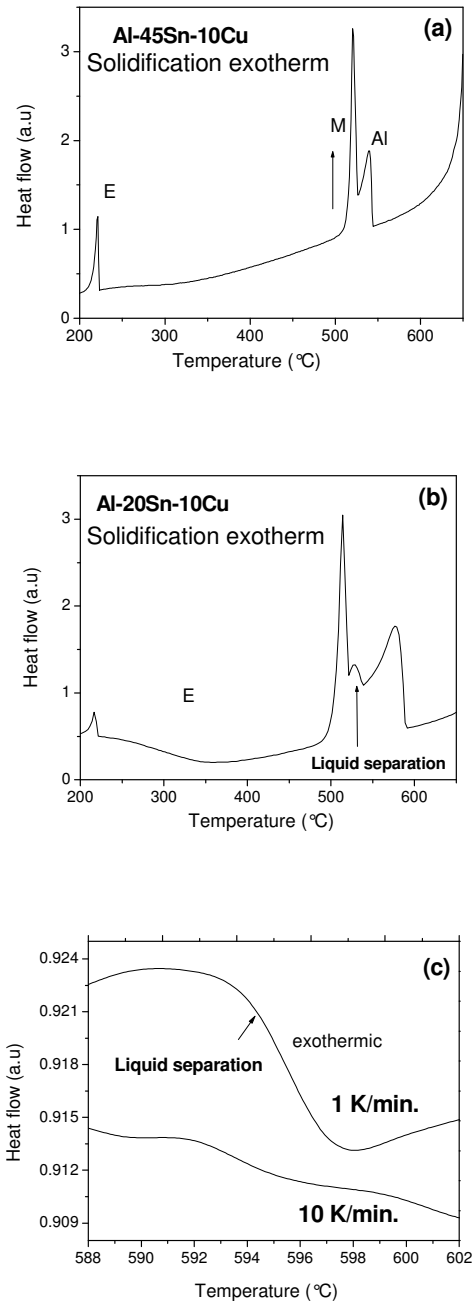

Fig. 4.3. DSC trace of (a) Al-45Sn-10Cu, (b) Al-20Sn-10Cu alloys at a cooling rate of 10 K/min; and (c) section of the DSC trace of Al-45Sn-10Cu at two different cooling rates, 1 K/min and 10 K/min.

Table 4.1. Temperatures extracted from the DSC traces for the Al-Sn-Cu alloys and compared with the calculated temperatures by CALPHAD. Note, the error in the temperatures has been considered to be equal to the standard deviation of the values obtained with the fit at the intersection with the *y* axis.

Sample composition in wt.%	Thermal signal		Calculated Temperature (°C)	Phase transformation
	Heating (°C)	Cooling (°C)		
Al-45Sn-10Cu	587.5	590	587	$L \rightarrow L' + L''$
	558.63	559.55	558	$L' \rightarrow (Al) + L''$
	525.66	526.8	523.8	$L' \rightarrow (Al) + \theta\text{-}Al_2Cu + L''$ $L'' \rightarrow (Al) + \theta\text{-}Al_2Cu$
	220	228.32	226.74	$L'' \rightarrow (Al) + \theta\text{-}Al_2Cu + (Sn)$
Al-20Sn-10Cu	605	592	600	$L \rightarrow (Al) + L$
	555	546	550	$L \rightarrow L' + (Al) + L''$
	521	526	523.8	$L' \rightarrow (Al) + \theta\text{-}Al_2Cu + L''$ $L'' \rightarrow (Al) + \theta\text{-}Al_2Cu$
	221.8	223	226.74	$L'' \rightarrow (Al) + \theta\text{-}Al_2Cu + (Sn)$

4.4 Microstructural evolution

4.4.1 Phase identification

For any new alloys, it is essential to note that all these thermodynamically-predicted phases should be confirmed with an experimental study. For this purpose, Al-20Sn-10Cu and Al-45Sn-10Cu alloys were prepared using a gravity cast method (Fig. 4.4), their

microstructures investigated using optical, SEM with EDX analysis and the main phases present identified. The EDX analysis identifies that the solidified samples consist of three main phases, namely, primary α-Al, θ-Al_2Cu and a Sn-rich. The corresponding measured EDX spectra are shown in Fig. 4.5.

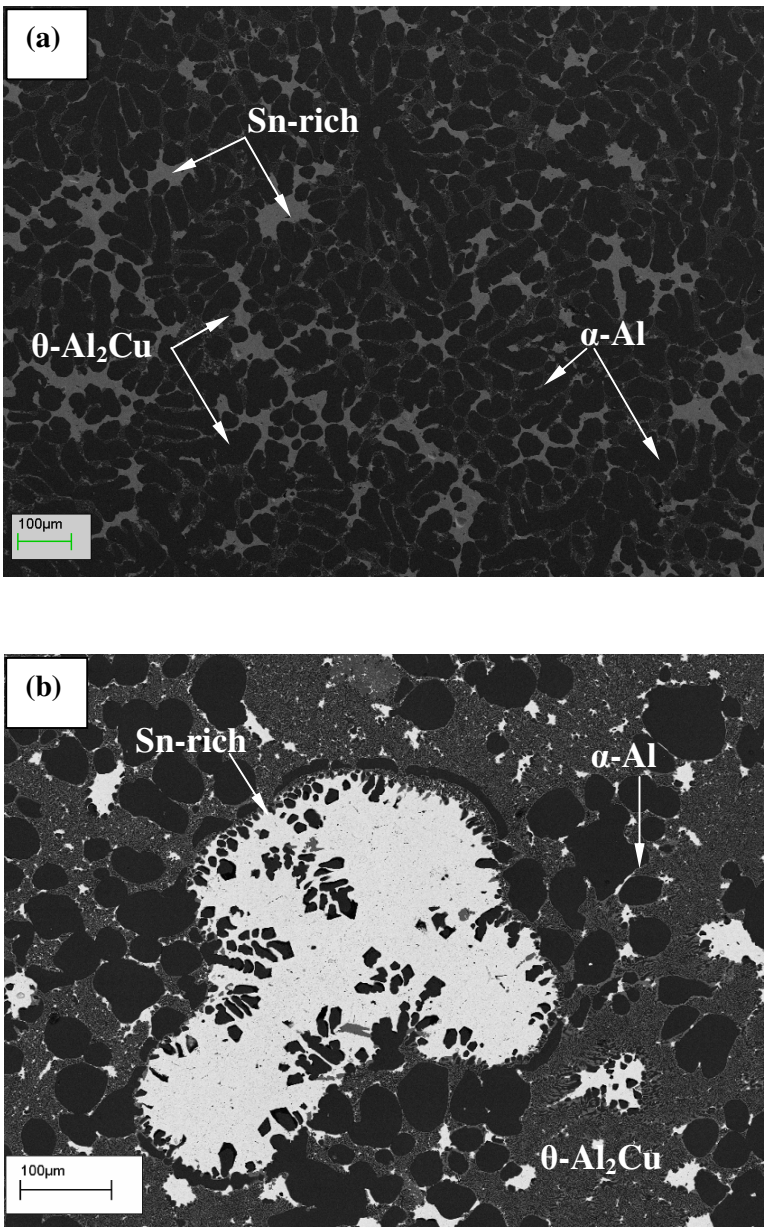

Fig. 4.4. Back scattered SEM micrographs of (a) Al-20Sn-10Cu alloy and (b) Al-45Sn-10Cu alloys, showing the Sn-rich phase, primary α-Al, and θ-Al_2Cu. The samples were prepared by gravity casting with the, liquid melt poured at 650 °C.

- The EDX spectrum obtained from the primary α-Al particles shows 2.5% Cu in the solid solution.
- The eutectic phase, θ-Al_2Cu (dark grey in contrast), is located in the matrix or between the primary α-Al dendrites. The measured EDX spectrum shows two major peaks corresponding to 59.4% Cu and 35.4% Al. The small peak is related to 5.2% Sn.

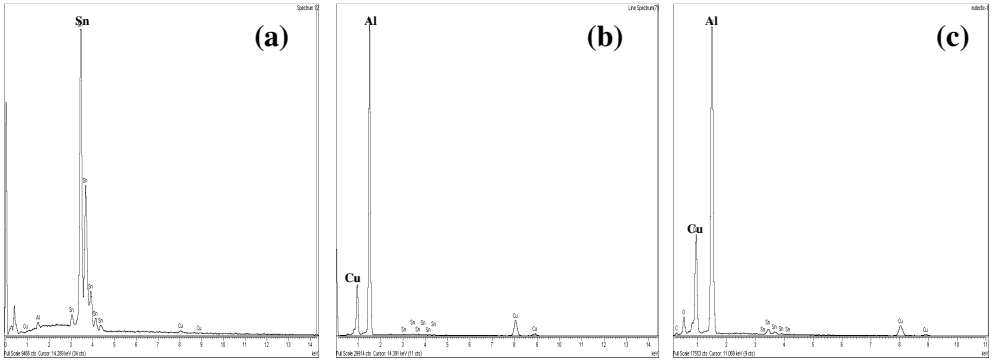

Sn-rich phase Al-rich phase θ-Al_2Cu

Fig. 4.5. EDX spectrum resulting from the microstructure of the gravity cast Al-45Sn-10Cu alloy (a) Sn-rich phase, (b) primary α-Al phase, and (c) θ-Al_2Cu.

4.4.2 Microstructural evolution in gravity casting

As mentioned in section 4.2, the solidification paths of the two chosen alloys are expected to differ significantly in the first stages. While Al-45Sn-10Cu shows demixing of the liquid phase before commencement of solidification, Al-20Sn-10Cu first shows precipitation of solid Al before demixing occurs. This can be seen in the microstructures of each alloy after conventional casting which is shown in Fig. 4.6. The most significant difference between these two micrographs is the agglomeration of Sn (white in contrast) in the Al-45Sn-10Cu sample (Fig. 4.6a) while Sn in the Al-20Sn-10Cu sample (Fig. 4.6b) is regularly distributed between the other phases in the microstructure, indicating that liquid separation occurred after primary solidification.

As seen in high magnification in Fig. 4.7, a typical microstructure of ternary Al-45Sn-10Cu alloy shows primary α-Al particles and Sn particles in a θ-Al_2Cu eutectic matrix,

the phases identified by using the SEM equipped with EDX analysis in the previous section 4.4.1. The microstructure of solidified L′ consists mostly of dendritic grains (Fig. 4.7). The solidified L″ microstructure, on the other hand contains Sn particles surrounded by the primary α-Al small dendritic. The primary α-Al dendrites structure of the solidified L″ phase indicates that Al-rich particles solidified first. Evidence for this is shown in Fig. 4.7b by the dendrites that have grown from the L′/L″ boundary into L″ (Munitz and Abbaschian 1996). Similar microstructures have been observed in the ternary Al-20Sn-10Cu alloy.

Solidification and segregation behaviour of Sn drops at a high cooling rate (~1000 Ks^{-1}) (HPDC and a wedge shaped Cu mould) were also investigated. In addition, the influence of intensive shearing on the phase separation has been extensively studied using the MCAST unit as described in section 3.3.

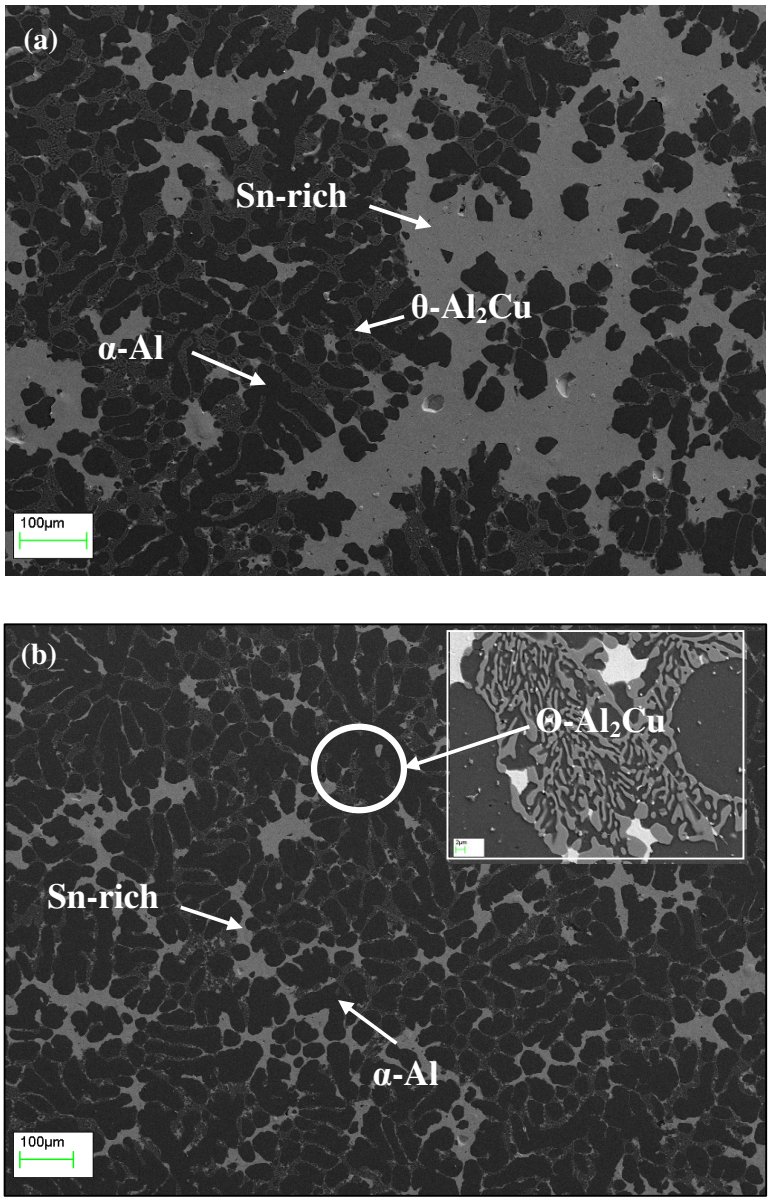

Fig. 4.6. SEM micrographs from (a) Al-45Sn-10Cu alloy and (b) Al-20Sn-10Cu alloy. The samples were cast in a steel mould directly from 650 °C. Inset in (b), shows a eutectic region at higher magnification. Note that substantial Sn-rich phase segregation occurred in the Al-45Sn-10Cu alloy, whereas in the Al-20Sn-10Cu alloy the Sn-rich phase is trapped between the primary α-Al dendrites.

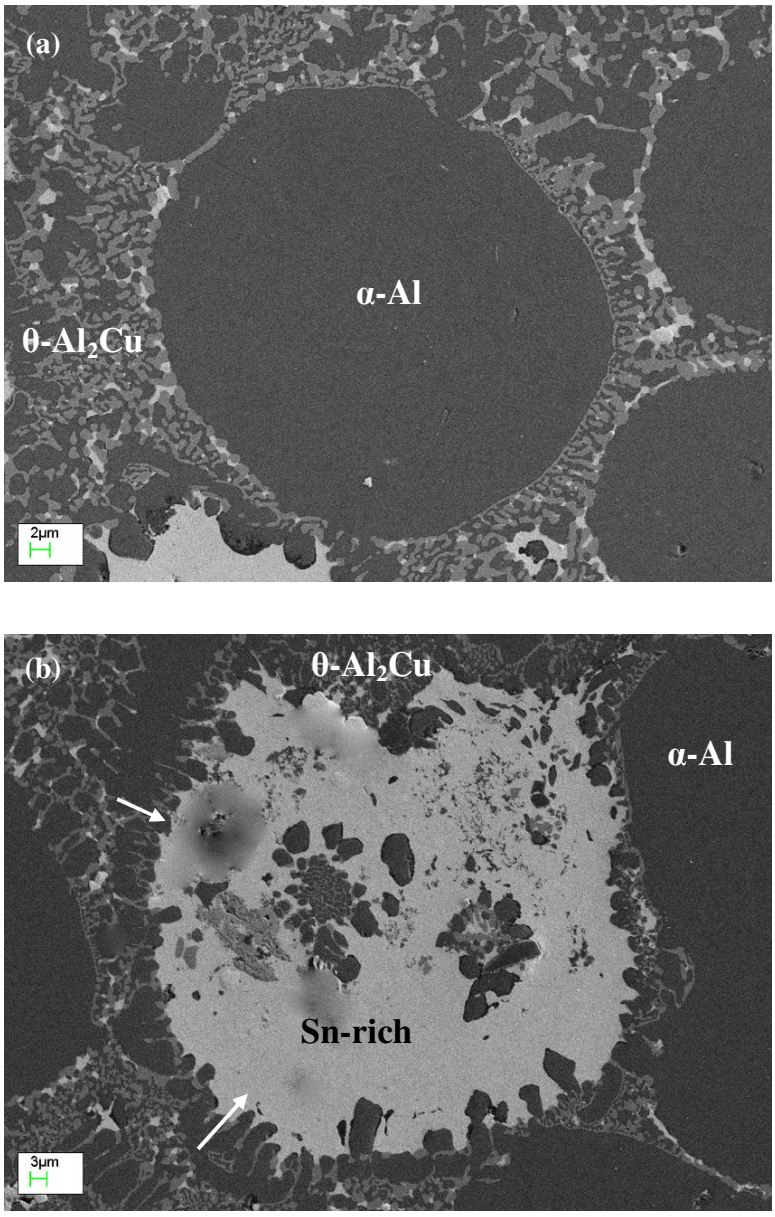

Fig.4.7. High magnification SEM images of the Al-45Sn-10Cu alloy showing (a) primary α-Al particle and (b) Sn-rich particle surrounded by α-Al dendrites that have grown from the L′/L″ boundary into L″, as marked by arrows.

4.4.3 Microstructure of HPDC and MC-HPDC samples

The most significant difference when comparing Figs. 4.8a and c (microstructures after the conventional HPDC process) with Figs. 4.8b and d (microstructures after the MC-HPDC process) is that a much finer microstructure is achieved with the MC-HPDC process. The distribution of the soft Sn particles (dark grey in contrast) is also much more uniform, particularly for the Al-45Sn-10Cu alloy sample. This indicates that intensive shearing affects the microstructure of immiscible alloy castings through droplet interaction, including rupturing, coalescence and suspension (Tang 2003a, Tang and Wrobel 2005a).

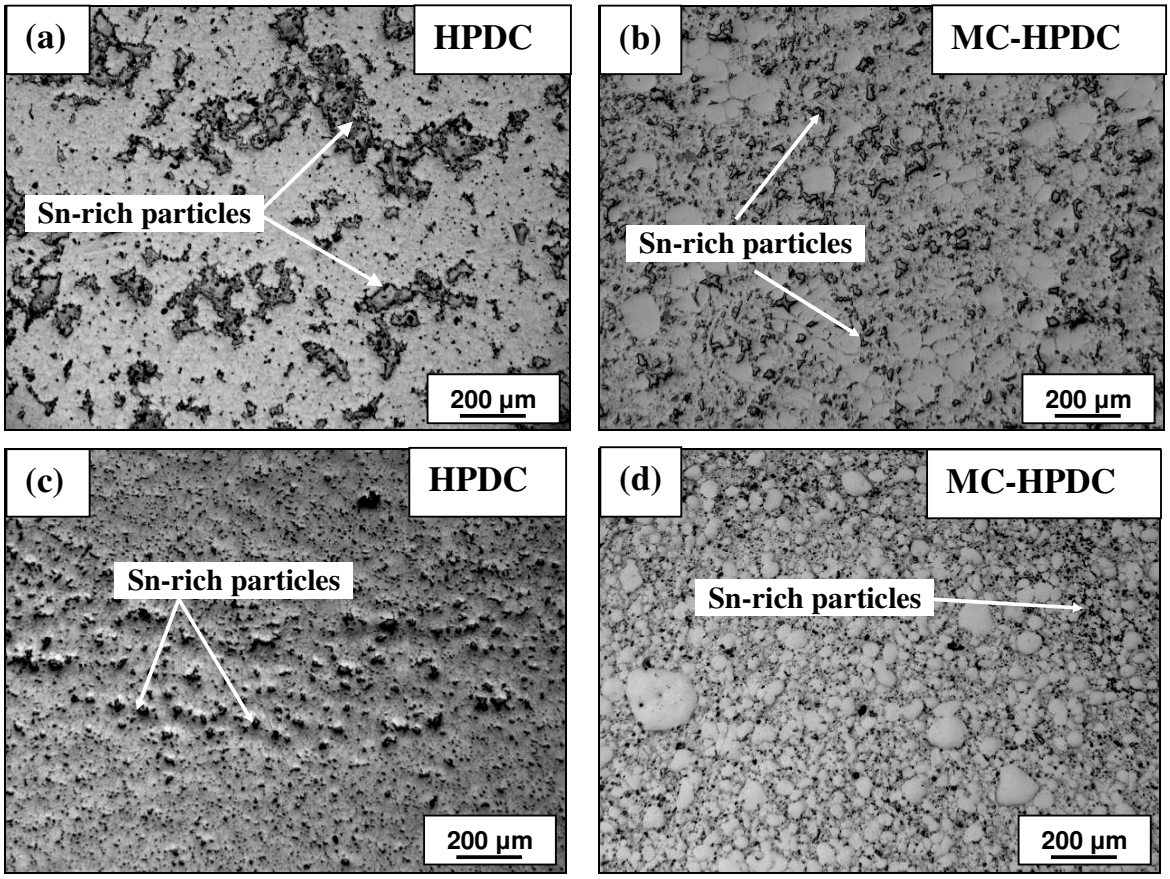

Fig.4.8. Typical OM images of HPDC and MC-HPDC tensile samples (a) and (b) Al-45Sn-10Cu alloy (T_p = 535 °C; shearing speed 800 rpm for 180 s) and (c) and (d) Al-20Sn-10Cu alloy (T_p = 580 °C; shearing speed 800 rpm for 60 s).

The microstructures produced after shearing with a variation of time and intensity were also characterised for their respective volume fractions of Sn and primary α-Al particles.

4.4.3.1 Effect of shearing time

Experiments were carried out to investigate the effect of shearing time on the size of the Sn particles in Al-45Sn-10Cu alloy. The melt at 650 °C (>T_c) was fed into the MCAST machine and was sheared at 535 °C and 800 rpm for 60 s, 120 s and 180 s. Fig. 4.9 shows the average Sn particle size as a function of shearing time, where the value corresponding to 0 rpm stands for the conventional HPDC processed sample. It can be seen from Fig. 4.9 that the average Sn particle size significantly decreased from 1 mm to 33 μm by applying shearing for just 60 s. A further increase in the shear time from 60 s to 180 s, resulted in very little further refinement of the Sn particle size. No significant segregation has been observed in the tensile sample as shown in Figs. 4.8b and d. Both Sn and primary α-Al particle volume fractions are observed to be fairly constant with different shearing times and also there was no apparent variation observed with shearing time for the primary α-Al particles size and shape factor. For the Al-20Sn-10Cu alloy, Fig. 4.8b shown that 60 s is the optimised shearing time, when processing at 585 °C and 800 rpm.

4.4.3.2 Effect of shearing speed

The intensity of shearing measured by the screw rotation speed (Eq. 3.1) had a strong effect on the formation of Sn particles. It is observed that solidification under a high shearing speed and a high intensity of turbulence produces fine and spherical Sn particles with a uniform distribution in the whole volume of sample as shown in Figs. 4.8b and d. In the present investigation the shearing speed range selected for both alloys varied from 200 rpm to 800 rpm, and the value corresponding to 0 rpm represents the conventional HPDC processed sample in Fig. 4.10. The shearing temperatures of 535 °C and 580 °C and shearing times of 180 s and 60 s were selected for the Al-45Sn-10Cu and Al-20Sn-10Cu alloys, respectively. Under such experimental conditions the average Sn particle size and shape factor for both alloys are presented in Fig. 4.10. For both alloys the Sn particle size decrease and the shape factor of Sn particles increases with increasing screw rotation speed, particularly when the speed is less than 200 rpm.

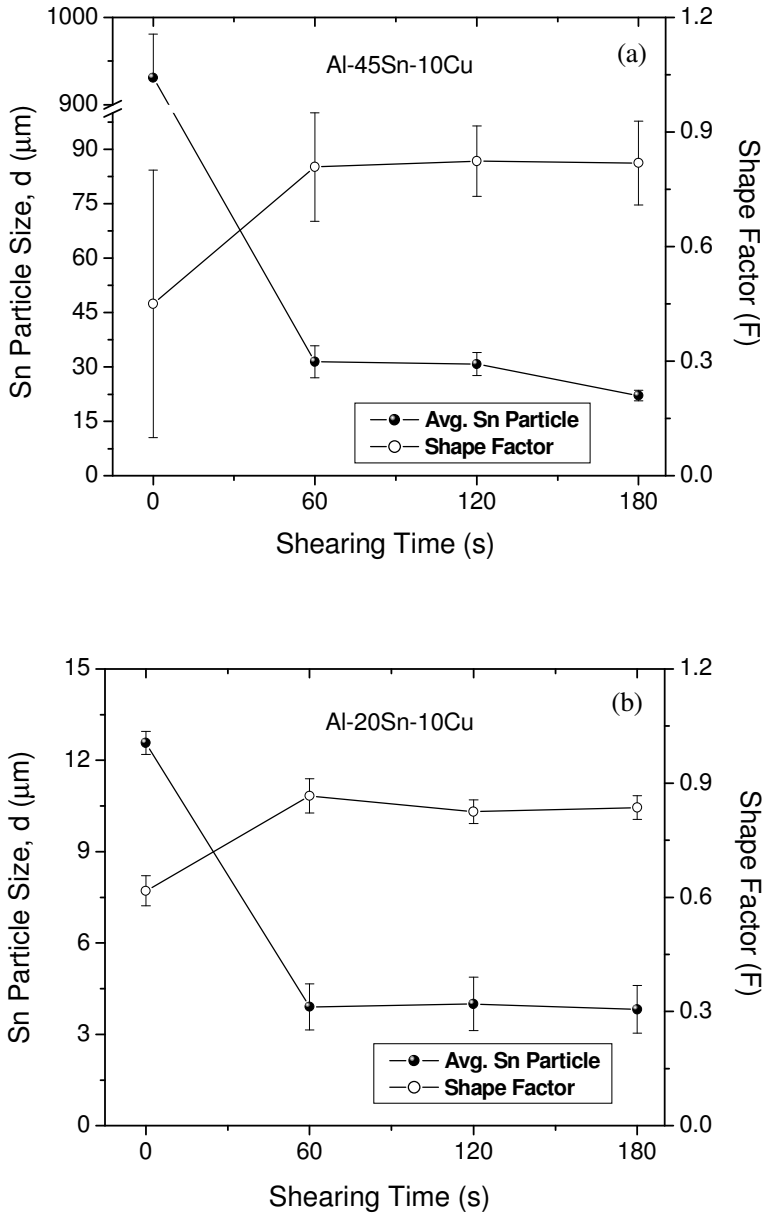

Fig. 4.9. Sn particle size and shape factor as a function of shearing time (s) (a) Al-45Sn-10Cu alloy; T_p = 535 °C and shearing speed = 800 rpm; and (b) Al-20Sn-10Cu alloy; T_p = 580 °C and shearing speed = 800 rpm. Intensive shearing reduced the Sn particle size from 1 mm to ~30 μm and 13 μm to about ~3 μm, after 60 s for the Al-45Sn-10Cu alloy and Al-20Sn-10Cu alloy, respectively.

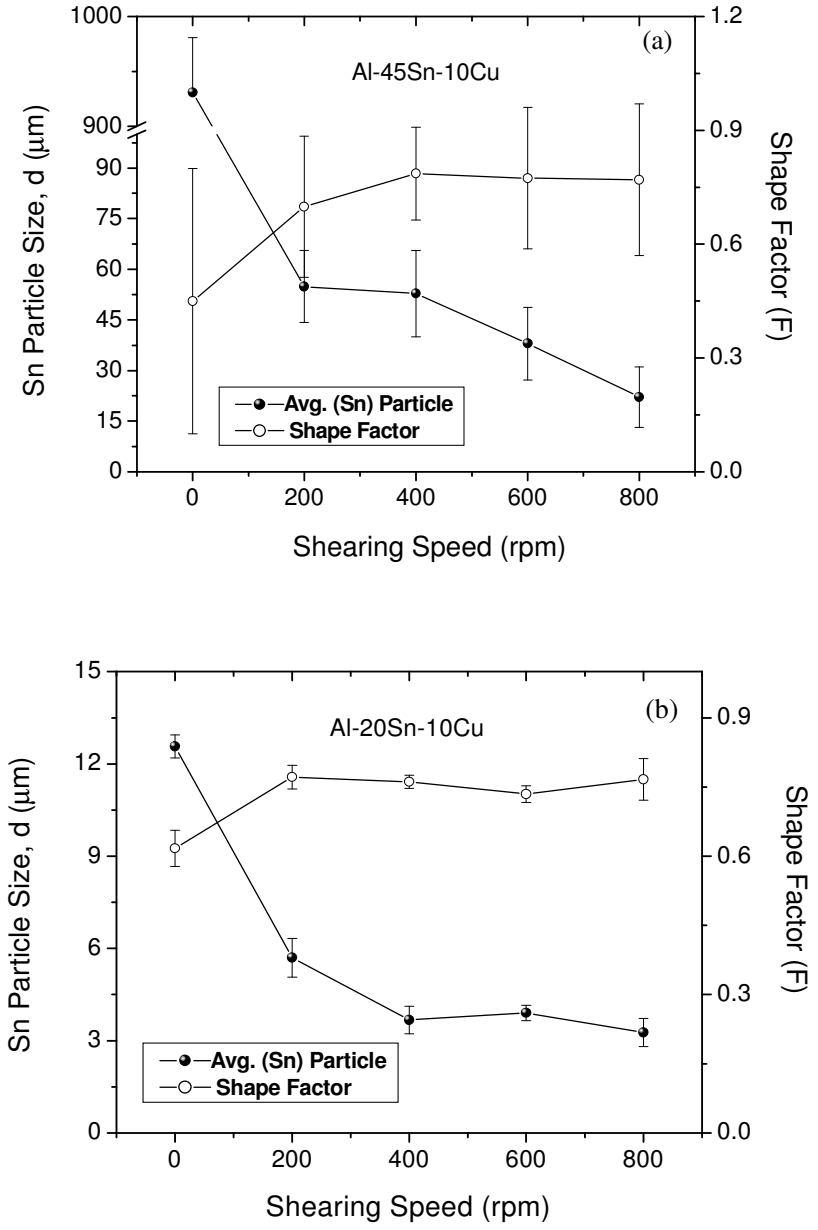

Fig. 4.10. The effect of intensive shearing on the Sn particle size and shape as a function of shearing speed (rpm) (a) Al-45Sn-10Cu alloy; T_p = 535 °C for 180 s; and (b) Al-20Sn-10Cu alloy; T_p = 580 °C for 60 s. Results shows that melt shearing at 200 rpm is adequate to produce a fine and uniform dispersion of the Sn phase.

4.4.4 Effect of cooling rate on the Sn particle size

Studying the size of droplets solidified after liquid phase separation can help in understanding the growth process of liquid droplet formation. The relationship between the extent of cooling below the liquidus curve and the size of the L″ droplets is studied by casting in wedge shaped copper moulds as described in section 3.4.1. This study was conducted on the Al-45Sn-10Cu alloy. After solidification, samples have been sectioned vertically along the major axis, polished and examined without etching by optical and scanning electron microscopy (SEM). The microstructure of the non-sheared sample revealed three striking results (Fig. 4.11):

(i) Sn-rich particles were mostly found in the middle of the section, along the major axis, as shown in Fig. 4.11,

(ii) Al-rich matrix, fills the space around the Sn-rich particles,

(iii) Eutectic θ-Al_2Cu phase fills the space around the Al matrix and Sn-rich particles (Fig 4.6).

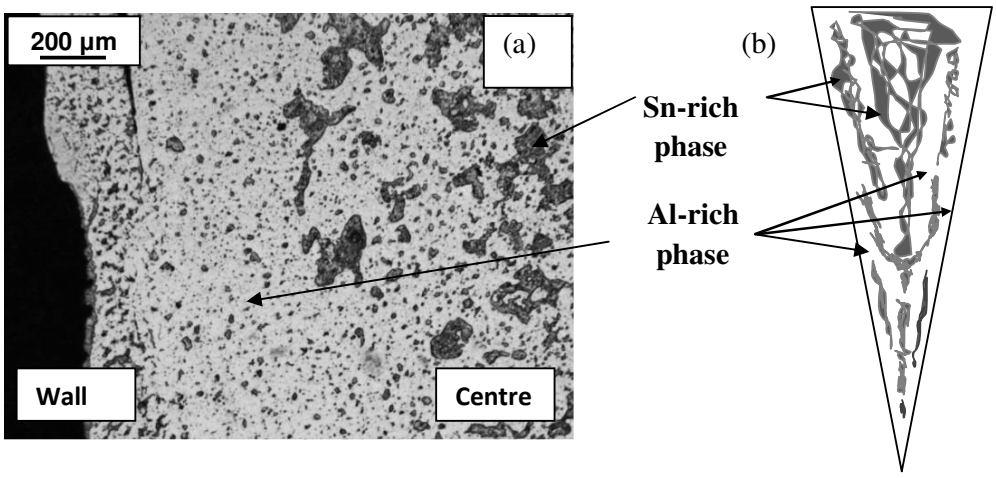

Fig. 4.11. Microstructures produced by casting a homogeneous alloy melt into the copper mould without shearing (a) Optical micrograph of Al-45Sn-10Cu alloy and (b) schematic illustration of phase distribution within wedge shaped sample produced with the Cu-mould. The pouring temperature of the liquid into copper mould was 650 °C.

The effect of cooling rate on the Sn-rich particle size has been investigated by measuring their size along the major axis of the wedge mould. Fig. 4.12 shows the distribution of Sn

particles at different locations along the main axis of the wedge for both sheared and non-sheared samples. From these micrographs, the differences in the Sn-rich particle size can be clearly seen to be more globular in shape. For non-sheared case, the general tendency is that the size of the L″ particles increases with the distance from the tip of the cast wedge sample, i.e. as the cooling rate is decreased. In contrast, optical and SEM micrographs from a sheared slurry reveal that the distribution of the L″ particles are uniform across the major axis of the sample from tip position to half-way along the sample (5 cm). Optical micrographs are shown in Fig. 4.12 at two different locations and quantified results for the sheared sample are shown in Fig. 4.13. Close to the tip the cooling rate is about 1000 Ks^{-1}; therefore the Sn-rich particle size is relatively small. Moving further away from the tip, the number of small spheres decreases while the number of large particles increases. Particle distribution is schematically illustrated in Fig. 4.11. The Sn-rich particles are very large and often around a few millimetres in diameter are found beyond 2 cm and 5 cm from the tip for non-sheared and sheared samples, respectively.

The dark regions are L″, while the bright ones are L′ as confirmed by EDX. This microstructure can be explained by assuming that at the top of the wedge, although the cooling rate is not high, the sample experienced high undercooling and remained liquid for longer time before crystal nucleation took place. When the undercooled melt reaches the miscibility gap it separates into two liquids (i.e. L′ and L″), as predicted by the calculated phase diagram. As the temperature decreases, in order to follow the equilibrium, demixing must take place inside. This explains the reason why most of the Sn-rich phase is located in the middle of the mould. This means that the Sn-rich phase (initially uniformly dispersed in the liquid) moved to the region that solidified later (the middle of the mould when cooling takes place from the mould walls). Fig. 4.11 represents a section of a large L″ drop exactly in the middle of the wedge and a small volume fraction of the Sn-rich particles observed very close to the mould wall, which is believed to form close to the mould wall due to high cooling rate from the Cu mould where Sn-rich particles do not get enough time to travel to the central area (last solidified part) before its final solidification. Failure to obtain a uniform dispersion is usually referred to as “the phase separation problem”. Sometimes it is also referred to as the “coarsening of dispersion” (Ratke 1993).

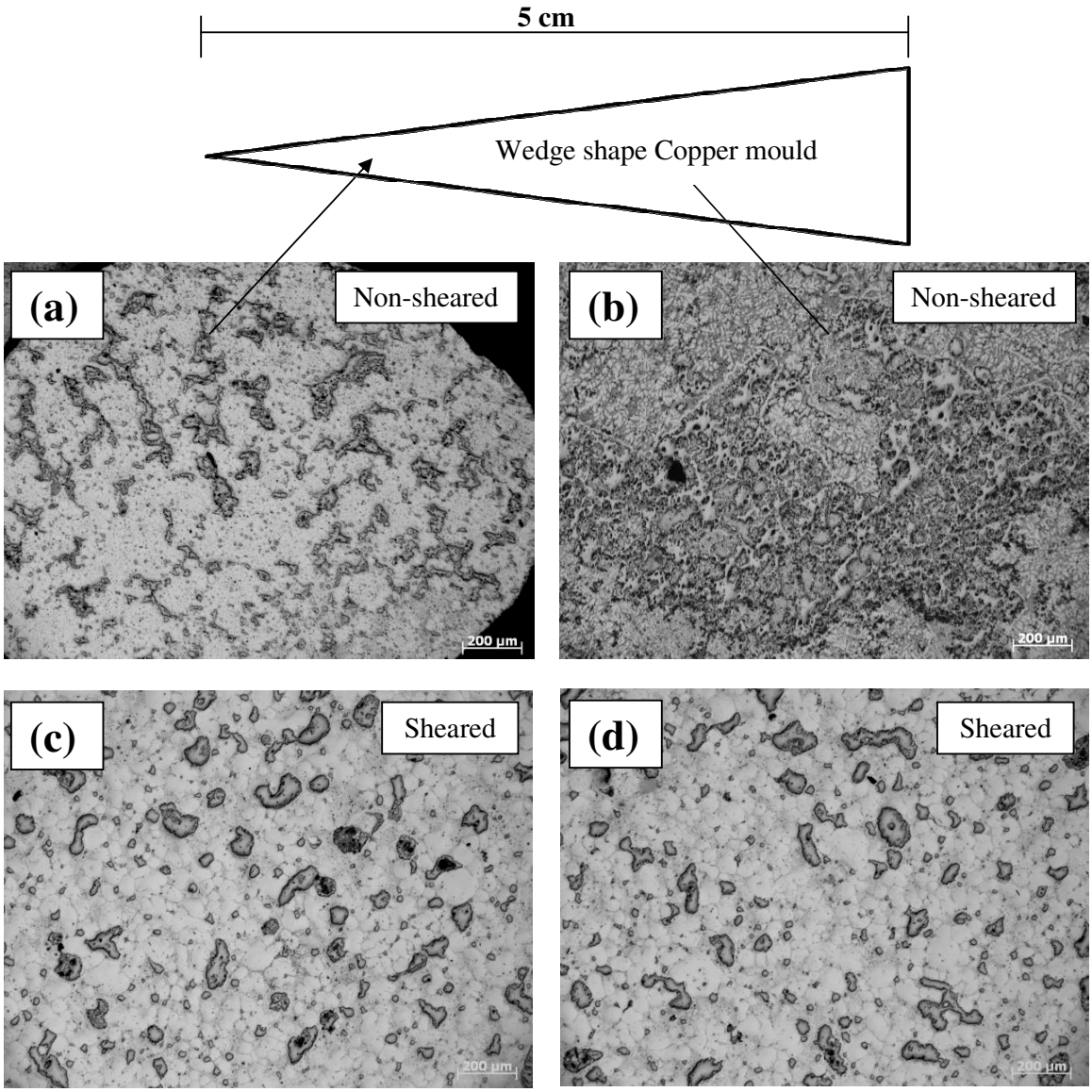

Fig. 4.12. Optical micrographs showing the distribution of Sn particles in the Al-rich matrix of different position along the wedge shape copper mould (a) and (c) at the tip and (b) and (d) at a position 2 cm away from the tip of copper mould. The bright area is Al-rich and dark grey area is the Sn-rich, and light grey area is the eutectic θ-Al_2Cu phase. Sample was prepared by gravity casting, melt directly poured in to the copper mould at 650 °C.

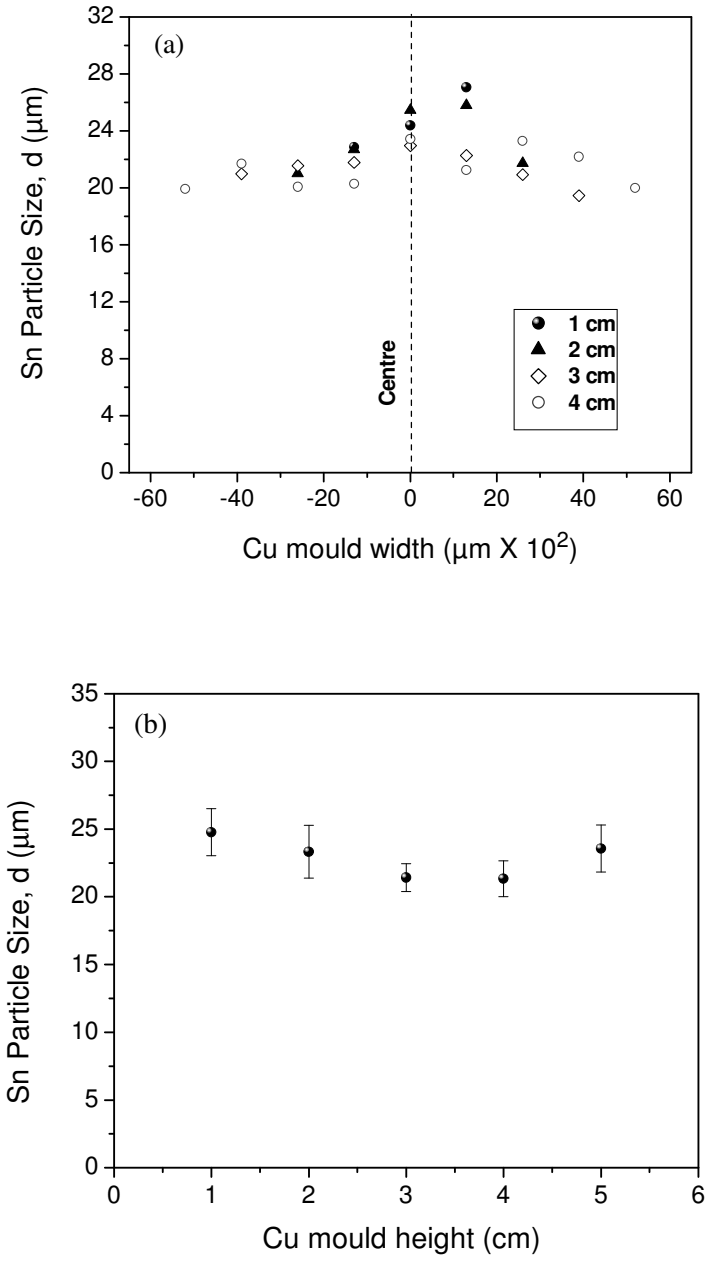

Fig. 4.13. Sn particle distribution in sheared Al-45Sn-10Cu alloy (a) quantitative analysis of Sn particles size with respect to the distance from the tip and (b) average Sn particle size *vs* height of the mould. Note that slurry sheared at 535 °C at 800 rpm for 180 s, non-sheared gravity sample cast directly in the copper mould from 650°C, showed huge segregation in non-sheared samples which was not able to be quantified.

4.5 Effect of Sn concentration on size of particles

Fig. 4.14 shows the microstructures of Al-Sn-Cu samples produced by MC-HPDC. The Sn particles (black in contrast) in all samples are dispersed uniformly in the Al matrix. A good distribution and fine size of Sn particles was achieved with optimum processing parameter. As the wt.% of Sn increases the average Sn particles size increases from 4 µm to 22 µm with an almost constant shape factor (Fig. 4.15a). No significant segregation has been observed throughout the cross section of the tensile sample as shown in Fig. 4.14. Fig. 4.15b reveals that α-Al particles are also spherical in shape.

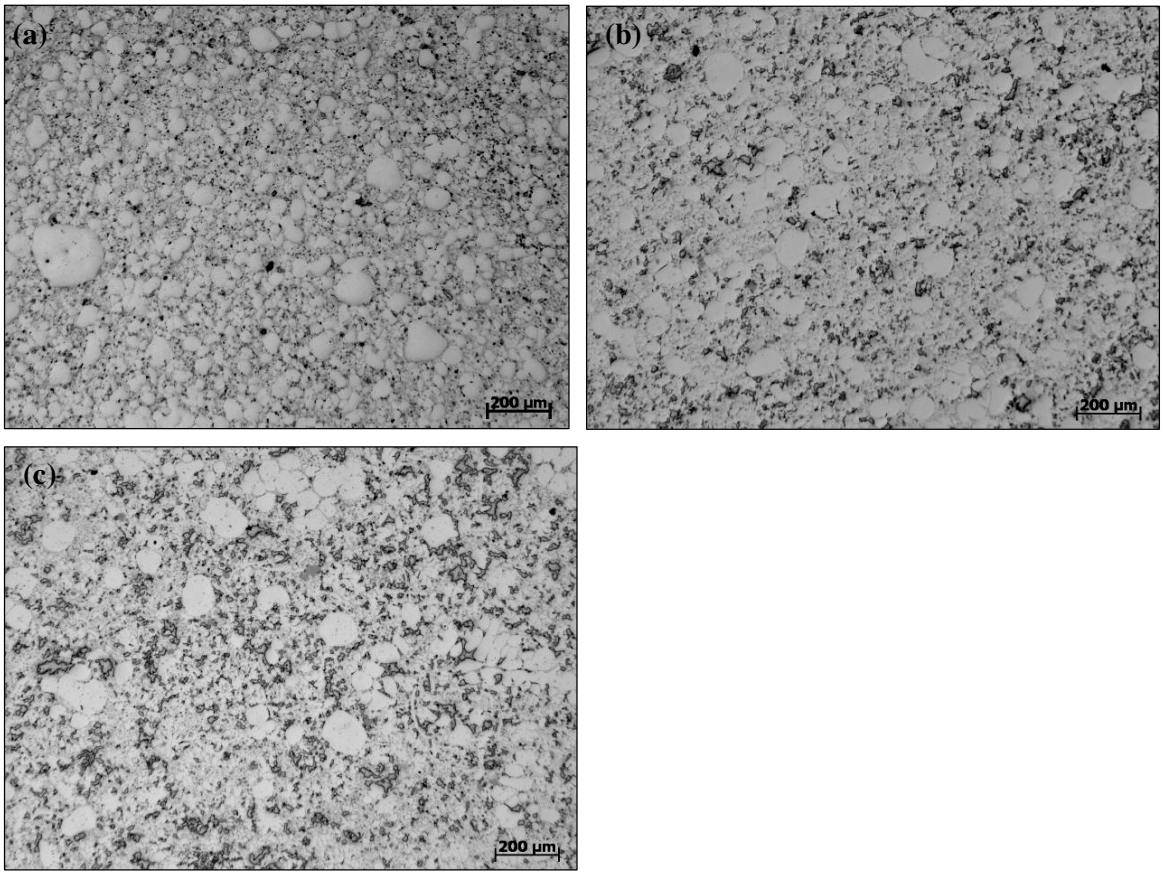

Fig. 4.14. Optical micrographs of various (90-*x*)Al–*x*Sn–10Cu alloys produced by the MC-HPDC process under optimal processing conditions (a) $x = 20$; $T_p = 580$ °C; shearing speed 800 rpm for 60 s (b) $x = 30$; $T_p = 580$ °C; shearing speed 800 rpm for 60 s, and (c) $x = 45$; $T_p = 535$ °C; shearing speed 800 rpm for 180 s.

The size of the α-Al particles vary between 40 µm to 50 µm with different Sn concentrations. The microstructures produced after shearing with a varied shearing time and intensity have also been characterised for their respective volume fractions of α-Al particles and Sn particles.

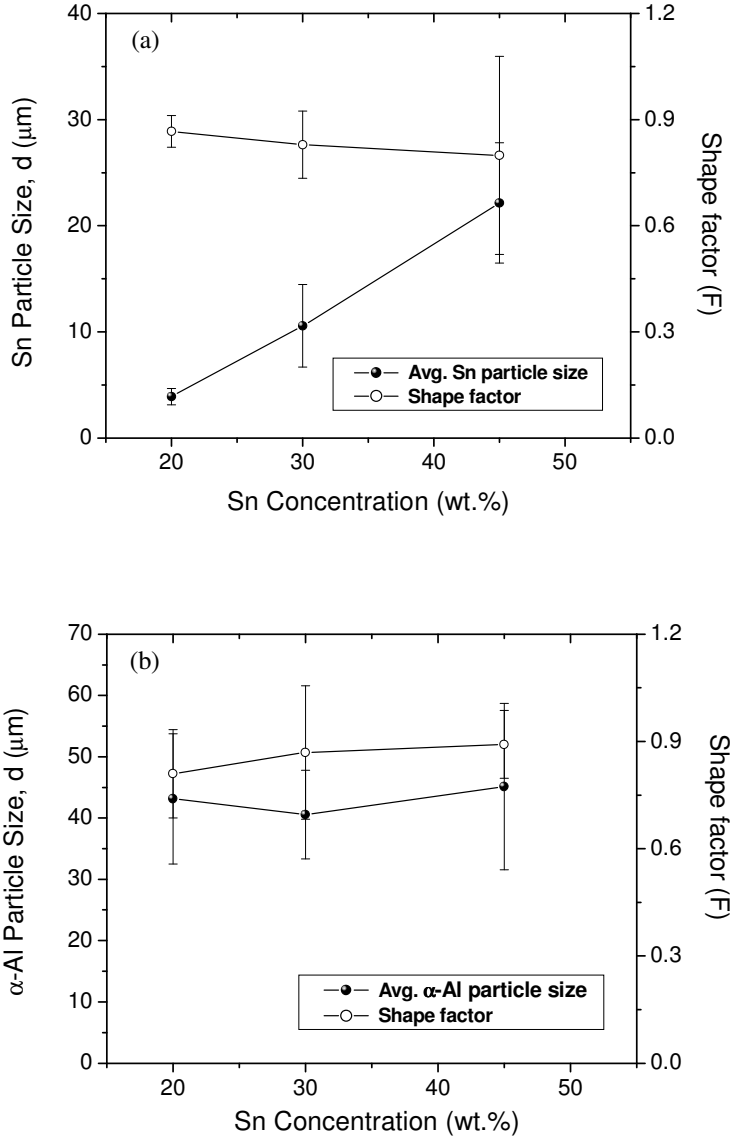

Fig. 4.15. Effect of intensive shearing on (a) Sn particle size and shape and (b) α-Al particle size and shape as a function of Sn concentration. Result show that the Sn particle size significantly increased with an increase in the Sn concentration. However, α-Al particle size did not vary with the Sn concentration.

4.6 Mechanical properties

HPDC components usually contain substantial amounts of porosity due to gas entrapment during the die filling and hot tearing during the solidification in the die cavity. In addition, processing immiscible alloy in the HPDC contains L″ droplets with large segregation and large defect bends are observed. Segregation and a defect band not only affect the mechanical properties but also restrict the property enhancements by subsequent heat treatment. An improvement in the distribution of L″ droplets in the Al matrix will have a positive effect on the age hardening response. Fig. 4.16 shows a comparative study of Vickers hardness with aging time of samples produced by the two different processes. The Al-20Sn-10Cu alloy MC-HPDC samples show an increase in average hardness with an increase in aging time up to 5 h and then no further improvement in hardness with time. While, the Al-45Sn-10Cu alloy MC-HPDC samples show an improved hardness within 1 h of aging time then no further improvement was noticed.

Samples produced with MC-HPDC have a much more homogeneous microstructure, L″ droplets being distributed more uniformly throughout the whole volume of the sample (Fig. 4.8). This is consequently reflected in smaller error bars in the curves of Fig. 4.16, indicating an improvement in the distribution of the L″ droplets which are more uniform and well distributed.

4.7 Summary

Two new Al-20Sn-10Cu and Al-45Sn-10Cu alloys were designed for melt conditioning by advanced shearing technology (MCAST) using the CALPHAD method. The thermodynamically calculated data and a systematic experimental study with differential scanning calorimeter (DSC) were compared. The experimental results are in good agreement with the theoretical data.

A comparison of the microstructures from different casting moulds for an Al-Sn-Cu alloy is presented in Fig. 4.17. The microstructures formed after rheomixing show a size distribution of Sn-particles. Two alloys Al-20Sn-10Cu and Al-45Sn-10Cu, show two

different microstructures based on the solidification path of these alloys. The new alloys have shown heat treatability by age hardening.

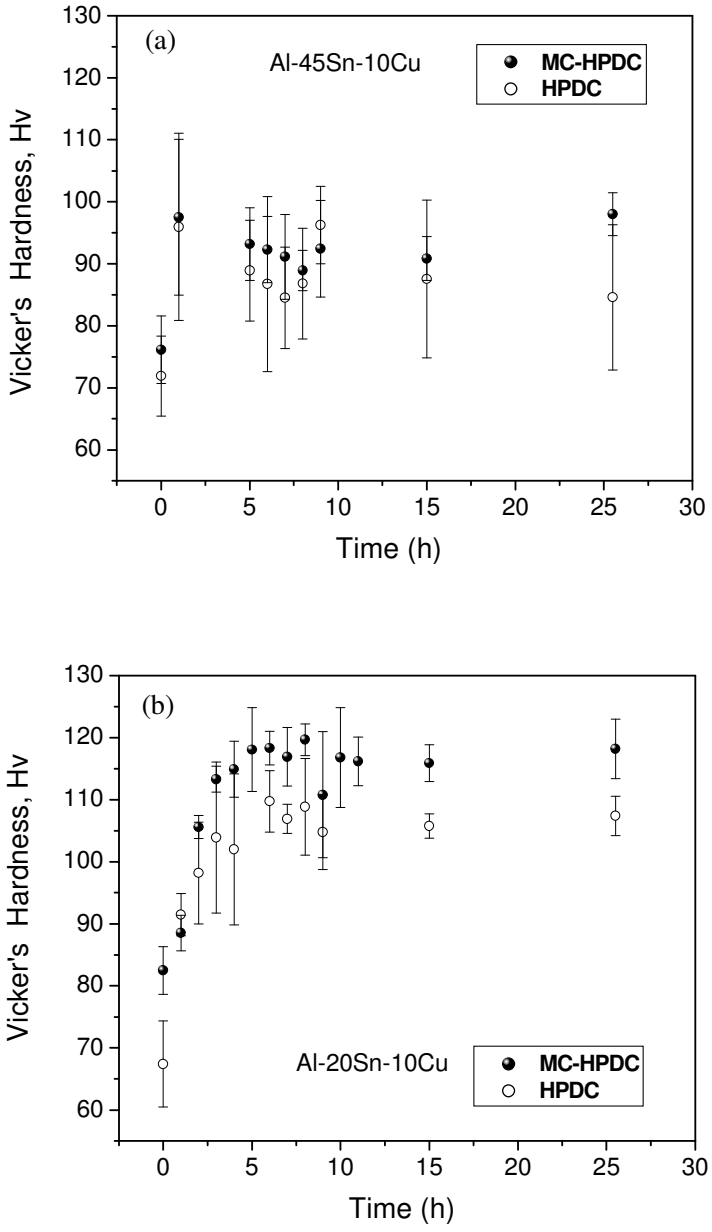

Fig. 4.16. Heat treatment curve, produced from MC-HPDC and HPDC samples (a) Al-45Sn-10Cu and (b) Al-20Sn-10Cu, heat treated at 200°C (below the eutectic), indicates that MC-HPDC samples gave better hardness compared to the HPDC samples.

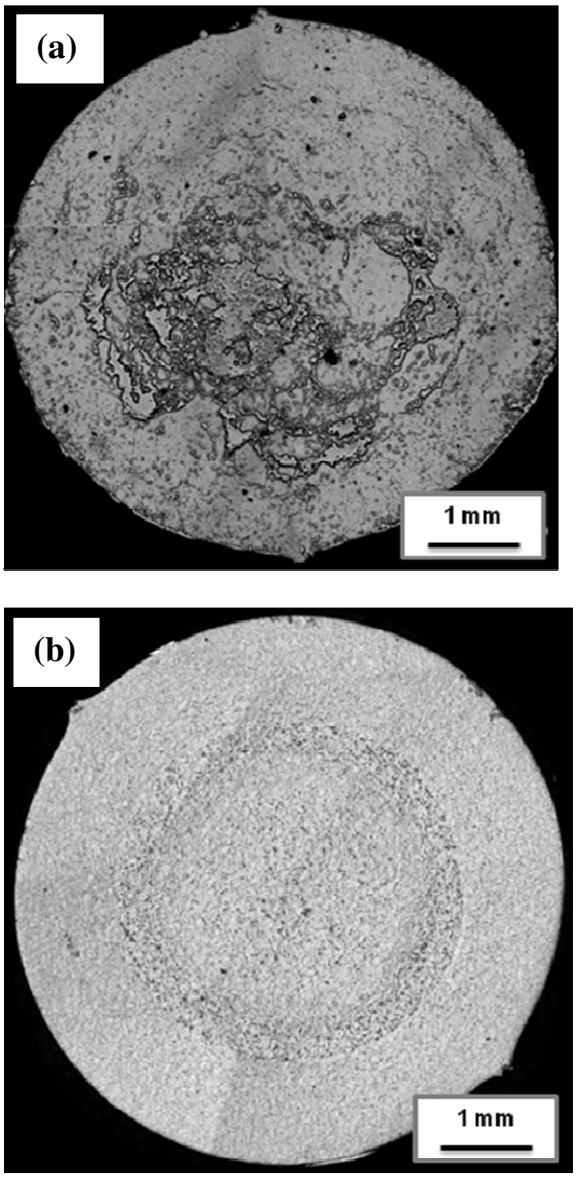

Fig. 4.17 Typical optical micrographs taken from Al-45Sn-10Cu alloy tensile sample cross section (6.4 mm diameter) (a) conventional HPDC and (b) MC-HPDC.

Chapter 5
Intensive Shearing of Al-Si Cast Alloys Results

5.1 Introduction

The objective of this work is to investigate the effect of intensive shearing on the solidification microstructure in a hypoeutectic Al-9.4Si (LM24: Al-9.38 Si-0.80Fe-2.31Cu-0.26Mn-0.49Mg-1.02Zn-0.04Cr-0.05Ti-0.001B), Al-10.3Si (Silafont: Al-10.26Si-0.21Fe-0.03Cu-0.51Mn-0.30Mg-0.03Zn-0.01Cr-0.06Ti-0.001B), hypereutectic Al-14Si (Al-14Si-0.01Fe) alloys (full alloy compositions are given in Table 3.1). Fig. 5.2 shows the Al-Si binary phase diagram. Based on the experimental evidence, in this chapter an attempt is made to address the specific issues of the exact nature of microstructural changes for the different phases. Quantitative analyses are carried out on ESC particles, defect bands, porosity, and mechanical properties under different experimental conditions. Tensile properties were considerably improved after applying intensive shearing to Al-Si alloys.

5.2 Microstructural evolution of Al-Si alloys

5.2.1 Solidification microstructure of the conventional HPDC samples

Optical micrographs of Al-10.3Si (hypoeutectic) and Al-14Si (hypereutectic) alloys obtained from HPDC with 630 °C T_p, are shown in Figs. 5.3a and b, respectively. In the hypoeutectic alloy, shown in Fig. 5.3a, the Al primary phase (white in contrast), with eutectic Si flakes are between the primary Al regions. A dendritic morphology of primary

α-Al phase was more commonly seen. The Al-10.3Si microstructure produced by the conventional method reveals a non-uniform microstructure with the primary α-Al. In the hypoeutectic alloy, the α-Al phase is classified into two categories; (i) large and spheroidal particles (denoted as α_1 or ESCs) are the primary α-Al phase formed during solidification, which are believed to form in the shot sleeve before the liquid reaches the die cavity for final solidification and (ii) fine particles (< 6 μm) called α_2-Al, which are formed inside the die cavity. Eutectic Si flakes exist between the primary Al regions. In the hypereutectic alloy, shown in Fig. 5.3b, the primary Si phase exhibits irregular morphologies and grows as hollow shapes known as "hopper" crystals (Elliott 1984). The matrix in this system is also made of Al and eutectic Si.

A typical cross section of a hypoeutectic Al-Si alloy tensile sample produced by HPDC is shown in Fig. 5.4. Three distinctive features are noticed: (i) a region of fine particles at the outer surface called the "skin"; (ii) a dark defect band at the centre; and (iii) a core of segregation with ESC particles at the centre, are observed and will be further discussed in section 5.3.2.

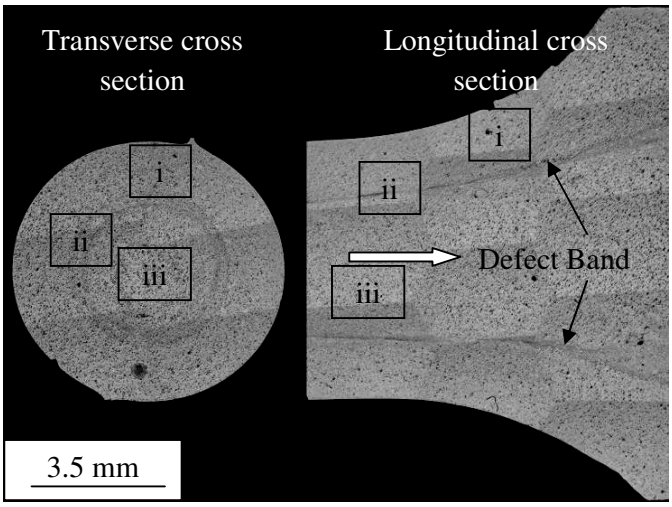

Fig. 5.1. Defect bands in a tensile test sample in the as cast conditions. Left side micrograph is the cross sectional view along the direction transverse to the fluid flow in the tensile sample. Ring shaped defect band can be seen half-way to the middle of the sample. Right side is a longitudinal view, where the formation of bands is extended to the entire sample. Arrow shows the bulk flow direction of the slurry.

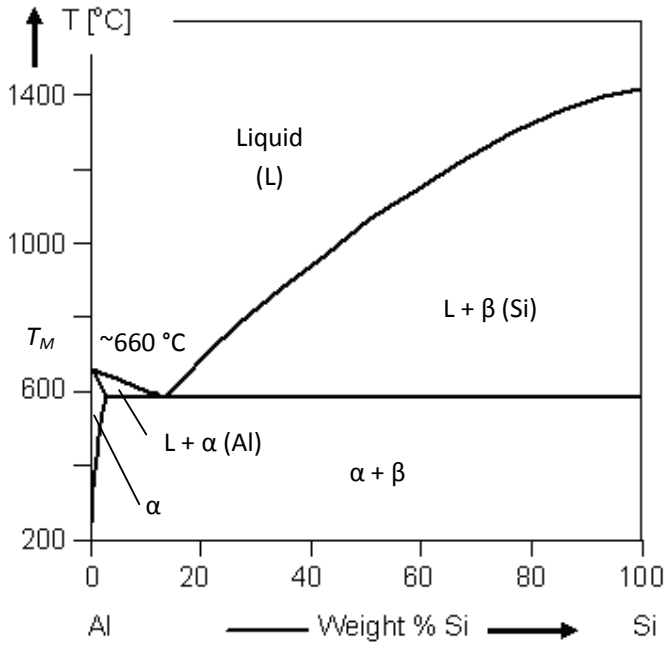

Fig. 5.2. Equilibrium phase diagram of Al-Si binary alloy, eutectic point at 12.7 wt.% Si.

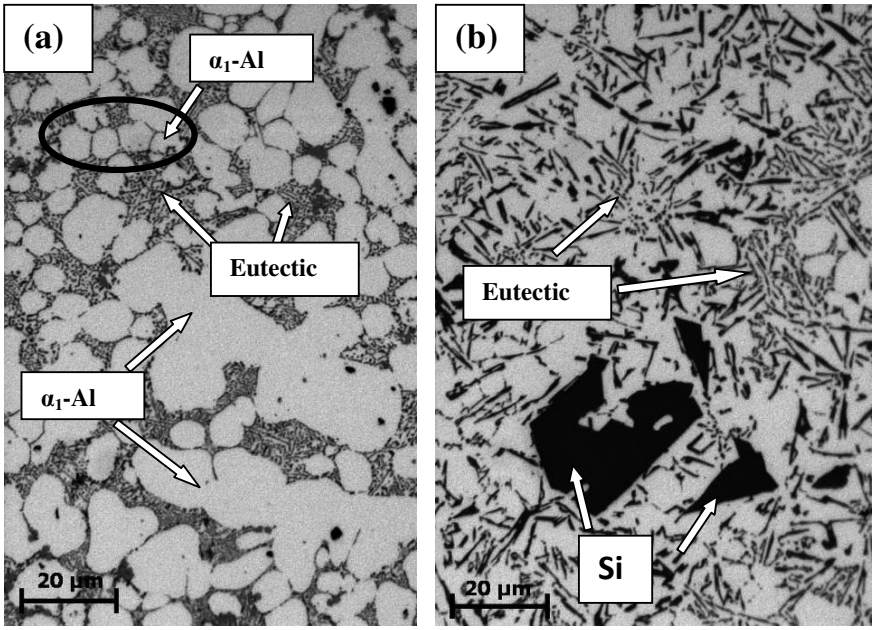

Fig. 5.3. Optical micrographs of (a) Al-10.3Si and (b) Al-14Si alloys, produced by HPDC at T_p = 630 °C.

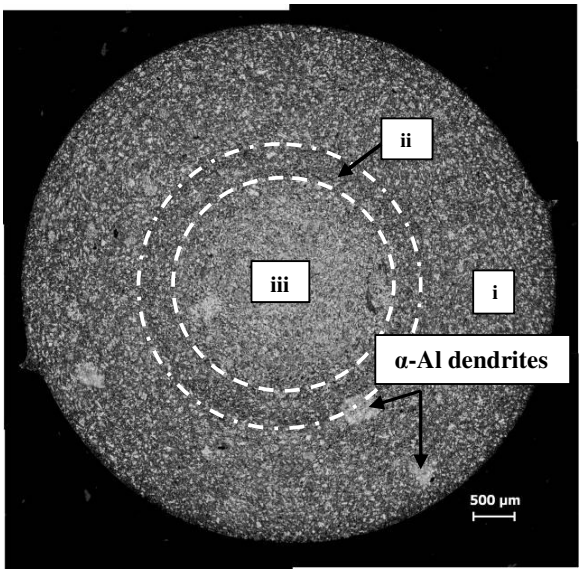

Fig. 5.4. Optical image of an Al-9.4Si tensile sample cross section produced by HPDC at T_p = 630 °C. ESCs are segregated at the central part of the cast sample. Regions (i), (ii), and (iii) represent the skin, defect band and ESC-rich region, respectively.

5.2.2 Solidification microstructure of the MC-HPDC samples

In the MC-HPDC process, intensive shearing is imposed directly on the melt in either the liquid or semi-solid state, prior to die filling. The implementation of the shearing is carried out by the MCAST unit, which is directly attached to a standard HPDC machine (Fig. 3.9). The conditioned melt in liquid or semi-solid slurry is then delivered to a HPDC machine for component shaping. During the MC-HPDC process, a predetermined quantity of superheated alloy melt is fed into the MCAST unit. The alloy melt is then cooled to a pre-set temperature whilst being mechanically sheared by a pair of screws. When the temperature is higher than the liquidus, the shearing of the melt takes place in the liquid state; whilst semi-solid slurry is created if the melt is at a temperature between the liquidus and solidus temperatures.

In contrast to the conventional HPDC process, the Al-Si alloys prepared by the MC-HPDC process showed a fine and uniform microstructure, as shown in Figs. 5.5 and 5.6. Compared to the HPDC sample, the large well-developed dendrites were eliminated in

the hypoeutectic alloy and the size of the primary Si particles in hypereutectic alloys was reduced. In both cases the MC-HPDC process allows the production of a primary phase uniformly distributed through the whole sample. The micro-pores are completely eliminated, and only small amount of very fine shrinkage pores can be observed in the MC-HPDC samples.

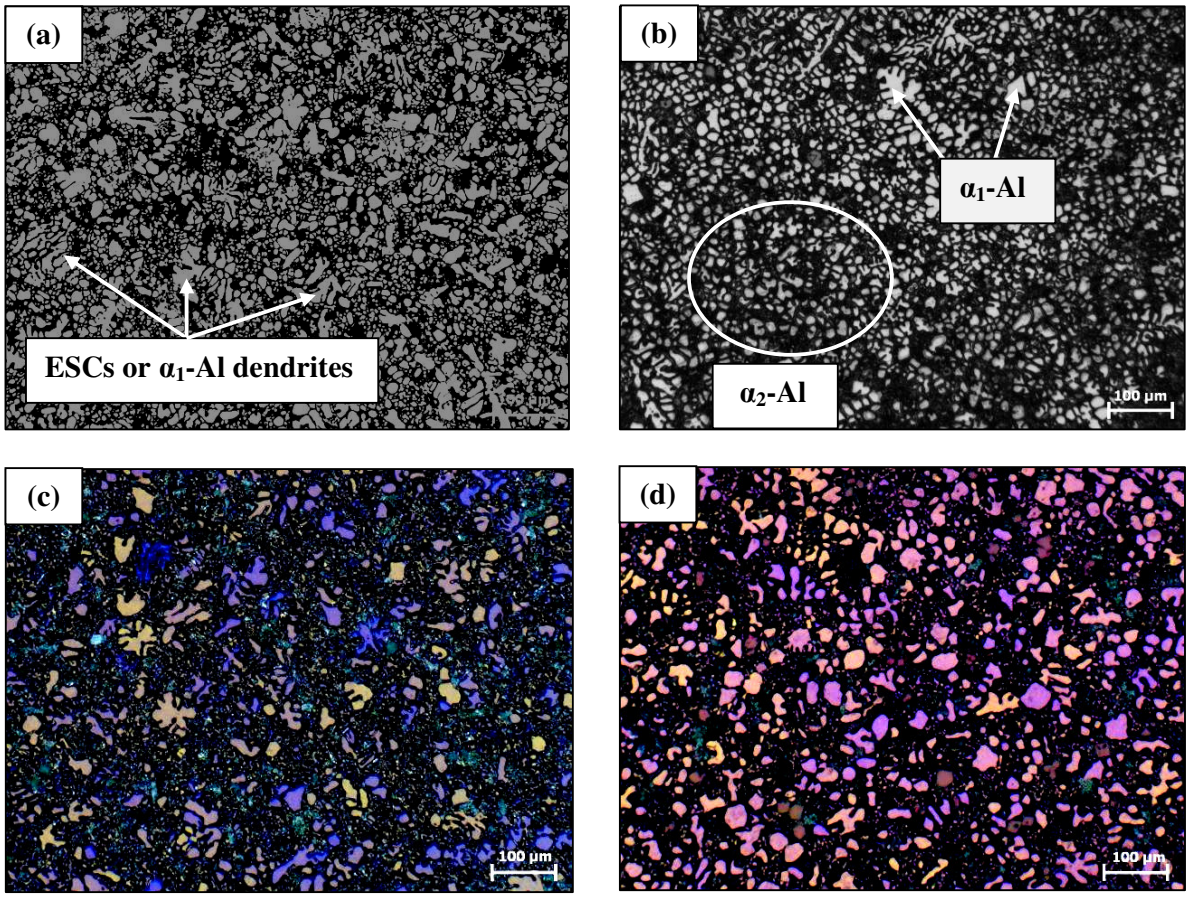

Fig. 5.5. Optical micrographs of Al-9.4Si sample produced by (a),(c) HPDC and (b),(d) MC-HPDC processes. Note that (a), (b) were taken from an etched surface (e*tched with a solution of 1g NaOH in 100ml H_2O, for 10 s*) and (c), (d) were taken from an anodised surface (*anodised with Barker's etching reagent* (*7 ml HBF_4 48%, 93 ml H_2O*)). The primary α-Al dendrites can be clearly seen in samples produced by HPDC while samples produced by MC-HPDC are virtually free of primary α-Al dendrites. It can be seen that the MC-HPDC process provides a finer and more uniform microstructure in comparison with the HPDC process.

Primary dendritic fragments (α_1) that are formed in the shot sleeve and the fine spherical particles (α_2) formed inside the die cavity can be seen.

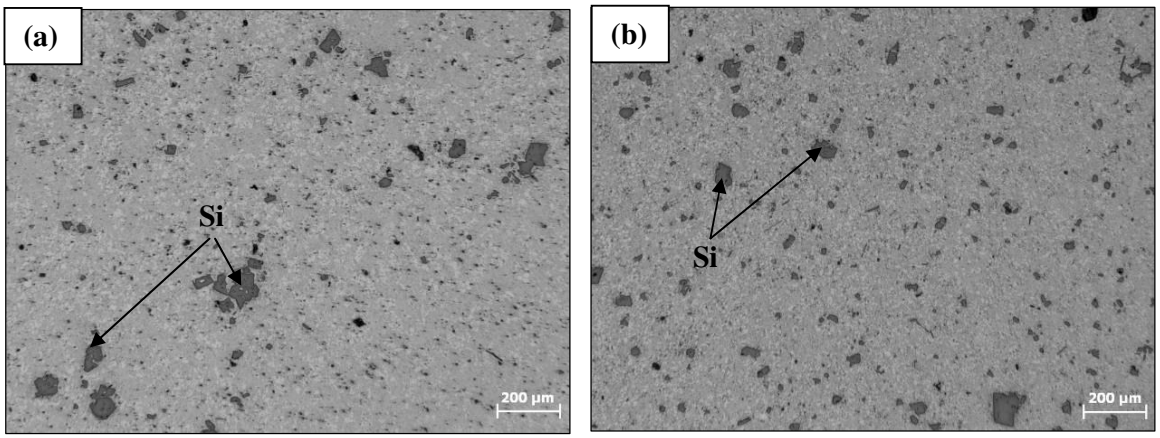

Fig. 5.6. Optical micrographs of hypereutectic Al-14Si samples produced by (a) HPDC and (b) MC-HPDC processes at T_p = 630 °C. It can be seen that the MC-HPDC process provides a finer and more uniform Si particle distribution in the whole microstructure in comparison with the HPDC process.

5.3 Hypoeutectic Al-Si alloys

5.3.1 Fraction of ESCs

To obtain an accurate value for the area fraction of ESCs, quantitative analyses were carried out on optical micrographs. The relatively low temperature of a shot sleeve enhances the formation of the ESC dendrites. This generates the early nucleation of the ESC particles in the shot sleeve. Tensile samples were cast at different pouring temperatures (T_p) by HPDC and MC-HPDC with other constant processing parameters associated with the HPDC machine (Table. 3.2). Graphs were plotted for the fraction of α_1-Al as a function of T_p (Fig. 5.7). The resultant quantitative analyses of both alloys show that the area fraction of ESCs significantly decreased by increasing the pouring temperature. From the quantitative analyses, we notice that intense shearing causes a considerable amount of change in the area fraction of ESCs. It can be said that the total area fraction of α_1-Al particles decreased with an increase of the pouring temperature (total area fraction of primary $f_{\alpha\text{-Al}} = f_{\alpha 1\text{-Al}} + f_{\alpha 2\text{-Al}}$). At the same time as shown in Fig. 5.4, the local area fraction of primary α-Al varies across the cross section and at the centre the

fraction of ESC is significantly higher. The ESC particle shape factor was observed to decrease with an increase in the pouring temperature while in sheared samples it was almost constant with different pouring temperatures.

The quantitative analyses shows that area fraction of α_1-Al significantly decreased from 23% to 11% and 16% to 8% for non-sheared and sheared samples, respectively by increasing T_p from 590 °C to 650 °C. A similar trend was observed for the Al-9.4Si alloy where α_1-Al area fraction was observed to decrease from 25% to 14% and 20% to 6%. Fig. 5.8, illustrates the shape factor (F) and size of particles (d) for both alloys with different T_p. The quantitative analysis of the α_2-Al particles was not carried out due to fact that their small diameters limited the differentiation of individual particles.

5.3.2 Defect band

A microstructural study of the cross section of HPDC and MC-HPDC tensile samples (6.4 mm diameter), for both alloys, reveal the presence of a defect band as shown in Fig. 5.9. Outer and inner edges of the band are highlighted with circular dotted lines. The band position was measured for samples with a single band, and the results are plotted in the Fig. 5.10. Defect band location or the skin thickness is defined here as the position along the radial distance from the casting surface to the outer edge of the band. Both hypoeutectic Al-Si alloy bands contain large amounts of Al-Si eutectic, coarser Al(Fe,Mn)Si intermetallic particles, and interdendritic porosity. By applying intensive shearing with the MCAST unit, the band thickness is observed to decrease significantly. Fig. 5.11 shows a comparison of HPDC and MC-HPDC sample cross sections. In the MC-HPDC sample primary α–Al particles are spread uniformly in the band region and this region does not contain well-defined edges. Fig. 5.12 shows the area fraction of primary α-Al as a function of cross section distance and also noticed from the quantitative result is that the band portion and/or position moved from the wall of the cast tensile sample towards the centre of samples with an increase in the pouring temperature.

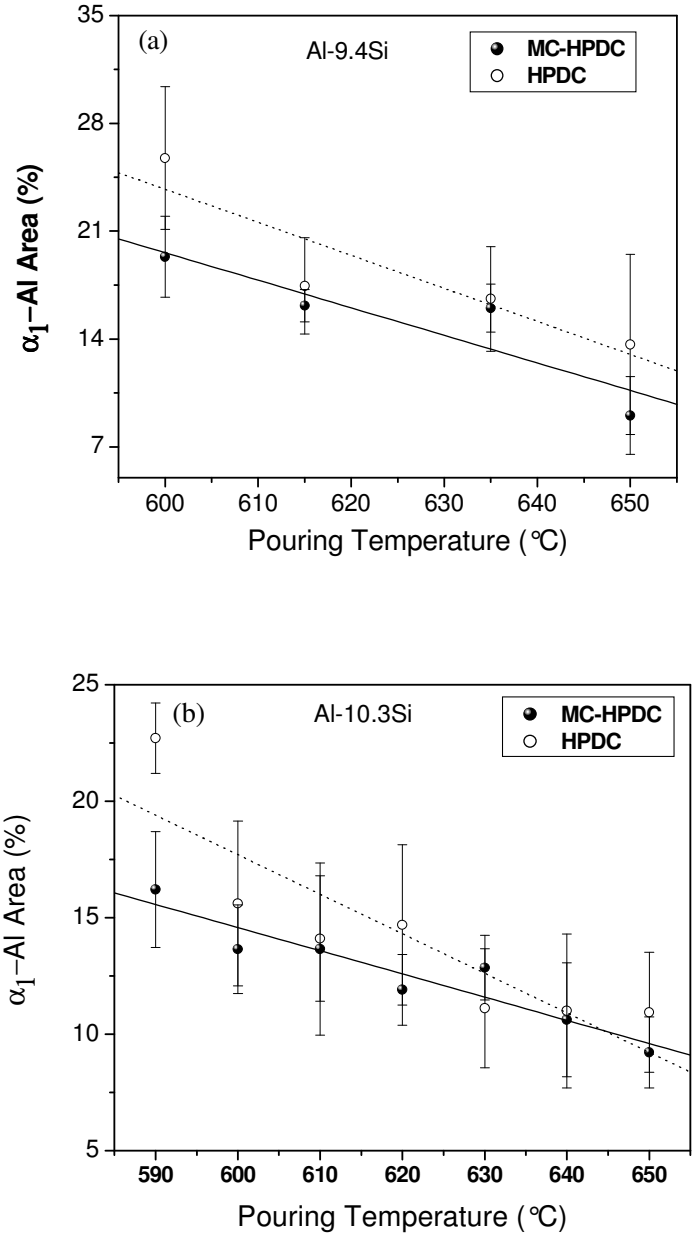

Fig. 5.7. Variation of the area fraction of primary α_1-Al or ESC phase as a function of pouring temperature (a) Al-9.4Si alloy and (b) Al-10.3Si alloy. Note that the α_1-Al area fractions are decreasing with an increase in the pouring temperature (total area fraction of primary $f_{\alpha\text{-Al}} = f_{\alpha 1\text{-Al}} + f_{\alpha 2\text{-Al}}$). Quantitative analysis was performed along the cross section of the tensile samples where the cross section diameter is 6.4 mm and gauge length is 25 mm, as shown in Fig. 5.9.

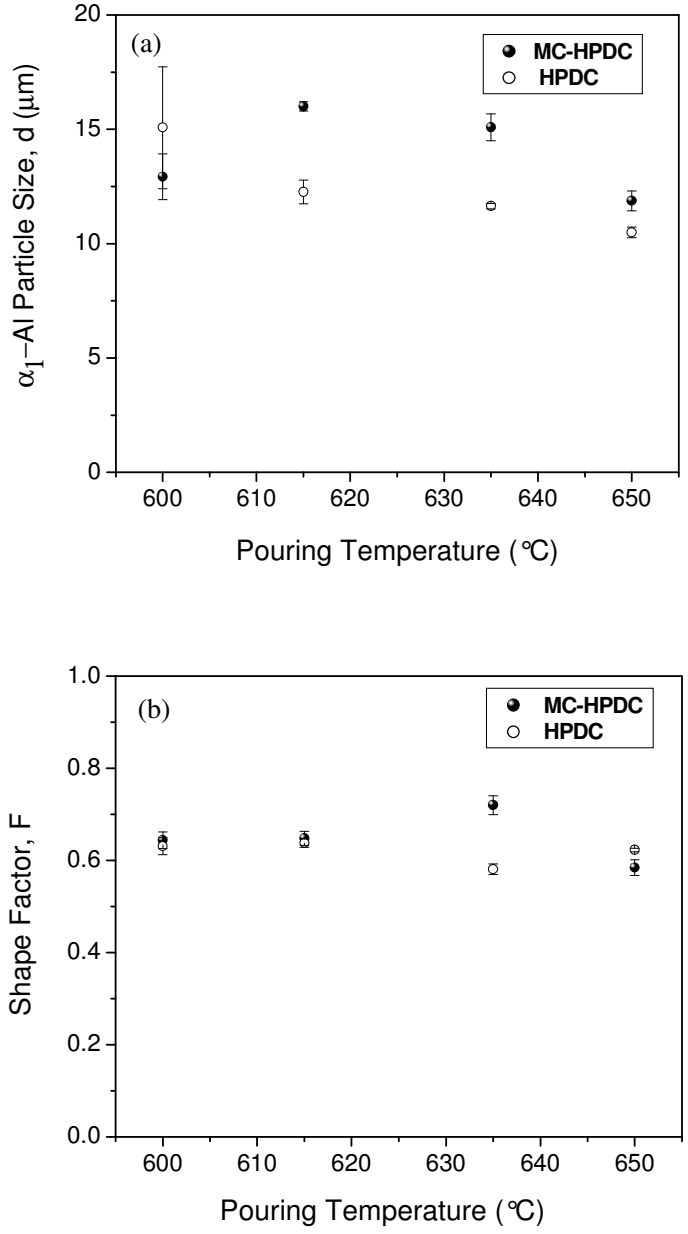

Fig. 5.8. Quantitative analysis of ESC particle (a) size (*d*) and (b) shape factor (*F*) of Al-9.4Si alloy as a function of pouring temperature. Note that α_1-Al particles size and shape are not varied with an increase in the pouring temperature (*Fig. 5.8 continues to next page*).

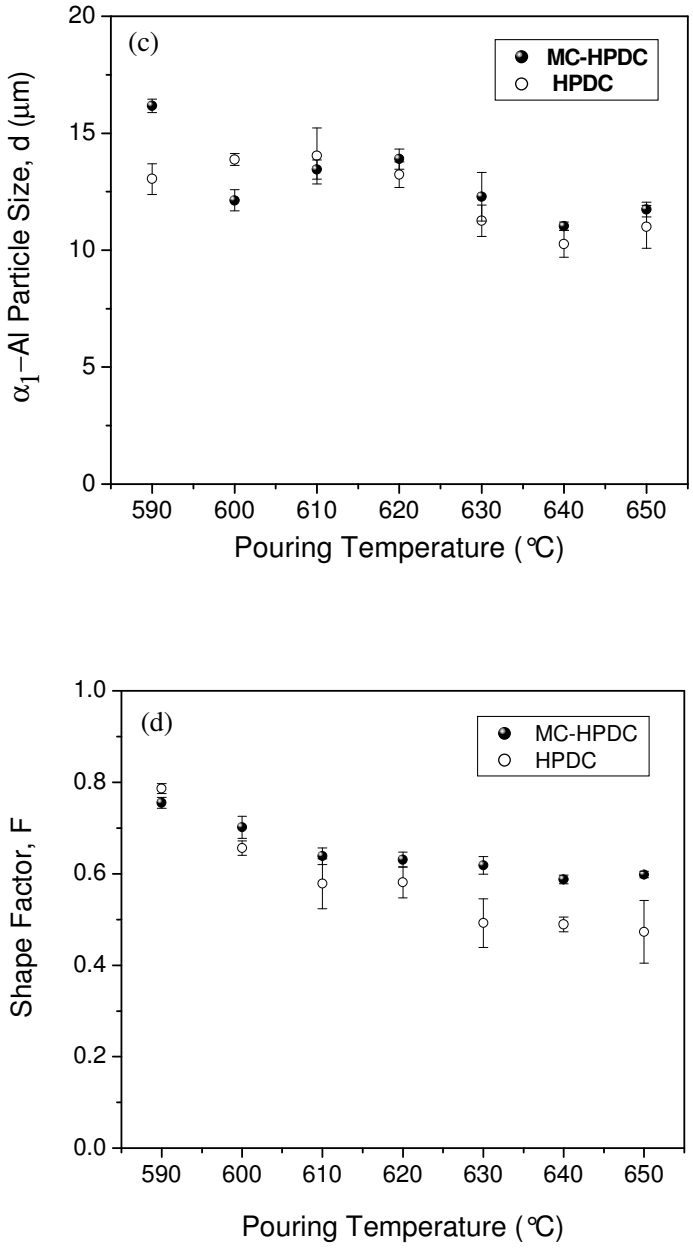

Fig. 5.8. Quantitative analysis of ESC particle (c) size (*d*) and (d) shape factor (*F*) of Al-10.3Si alloy as a function of pouring temperature. Similar to the Al-9.4Si alloy, α_1-Al particle size and shape are not varied with an increase in the pouring temperature.

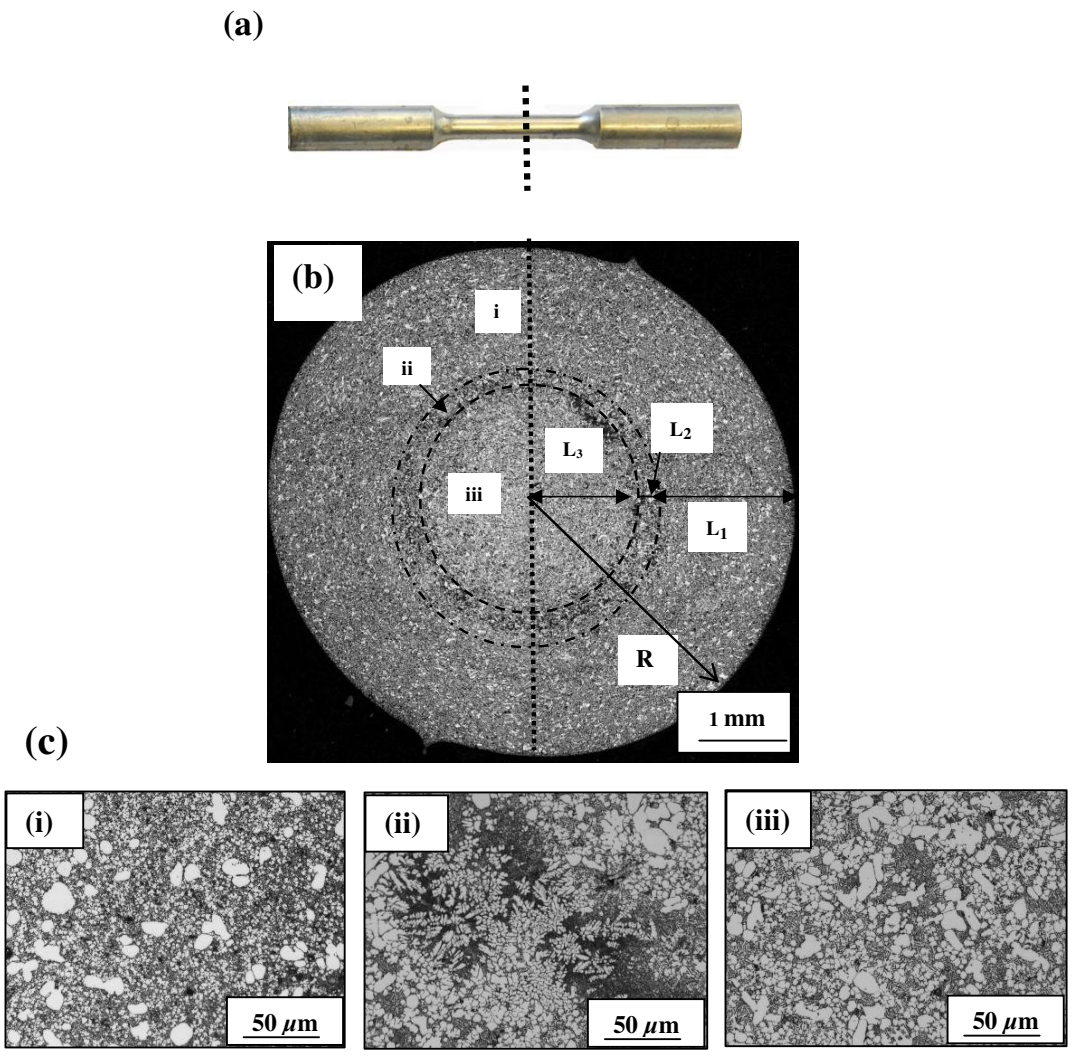

Fig. 5.9. (a) Tensile sample, dimensions of the test samples are 6.4 mm in gauge diameter, 25 mm in gauge length and 12 mm in diameter of grip section. Dotted line corresponds to location where sample was cut (b) Optical image of Al-10.3Si alloy tensile sample cross section produced by HPDC at T_p = 630 °C ESCs are segregated at the central part of cast sample, and (c) higher magnification (i), (ii), and (iii) regions represent the skin, defect band and ESCs region, respectively.

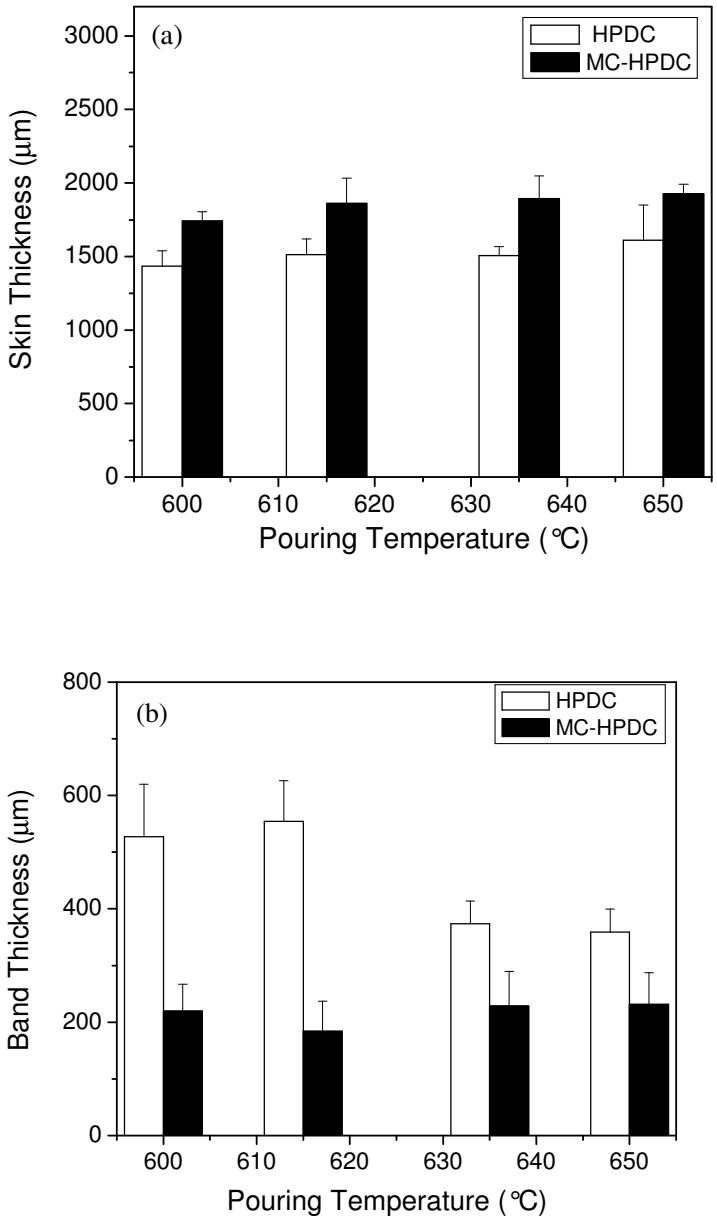

Fig. 5.10. (a) Skin and (b) band thickness of Al-9.4Si alloy tensile samples with different pouring temperatures. Note that skin thickness is defined here as the position along the radial distance from the casting surface to the outer edge of the band (Fig. 5.9b). The results reveal that the band position moves from the wall of the cast tensile sample towards the centre of samples with an increase of the pouring temperature. In addition, after intensive shearing the skin and band thickness are increased and decreased, respectively (*Fig. 5.10 continues to next page*).

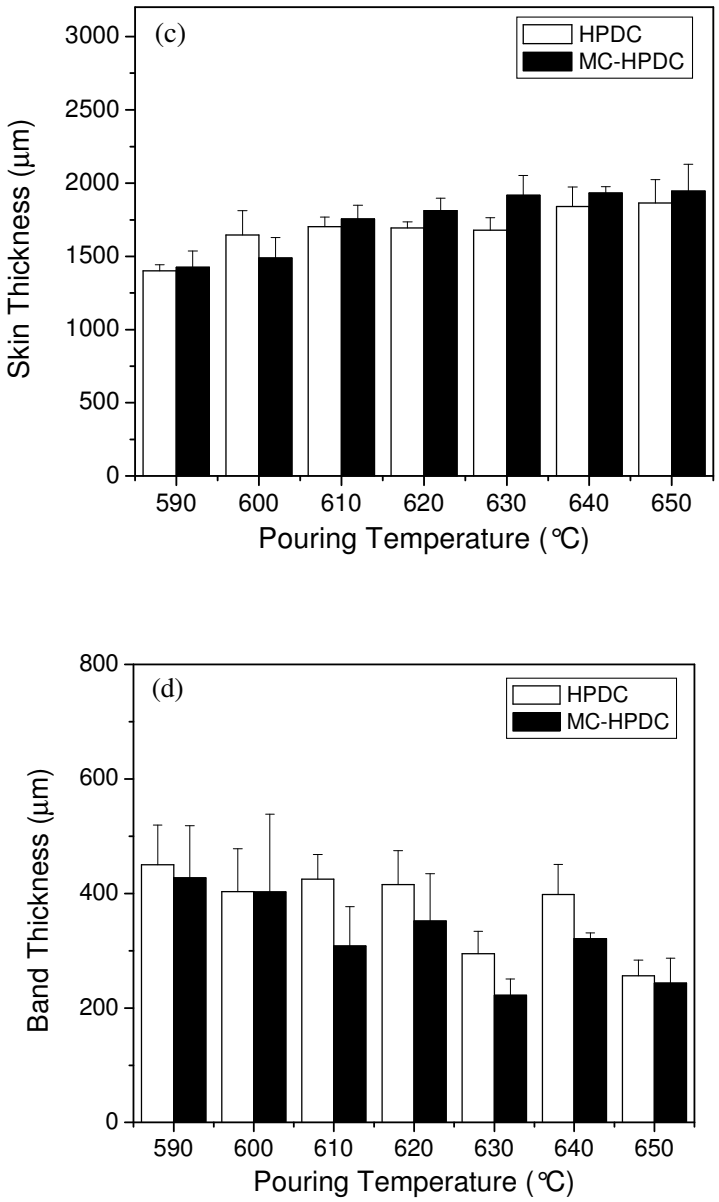

Fig. 5.10. (a) Skin and (b) band thickness of Al-10.3Si alloy tensile samples under different pouring temperatures. Results obtained are similar to the Al-9.4Si alloy, where the skin thickness increased and the band thickness decreased with an increase of the pouring temperature. Considerable benefits were obtained from intensive shearing on band thickness.

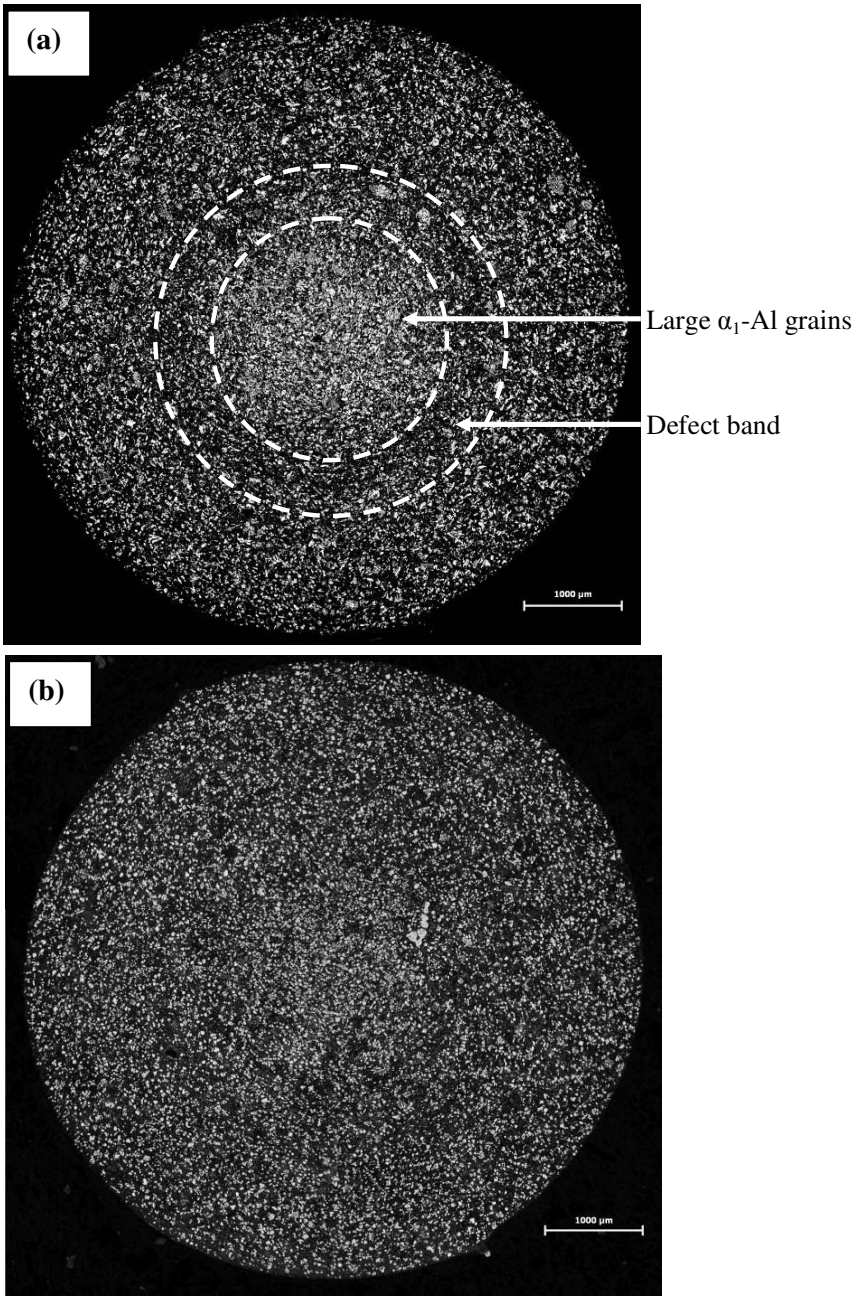

Fig. 5.11. Micrographs of tensile samples cross sections (6.4 mm diameter) Al-10.3Si alloy (a) HPDC sample showing a defect band and large α_1-Al central grains and (b) MC-HPDC sample with negligible band or diffused band with a uniform α_1-Al particles distribution.

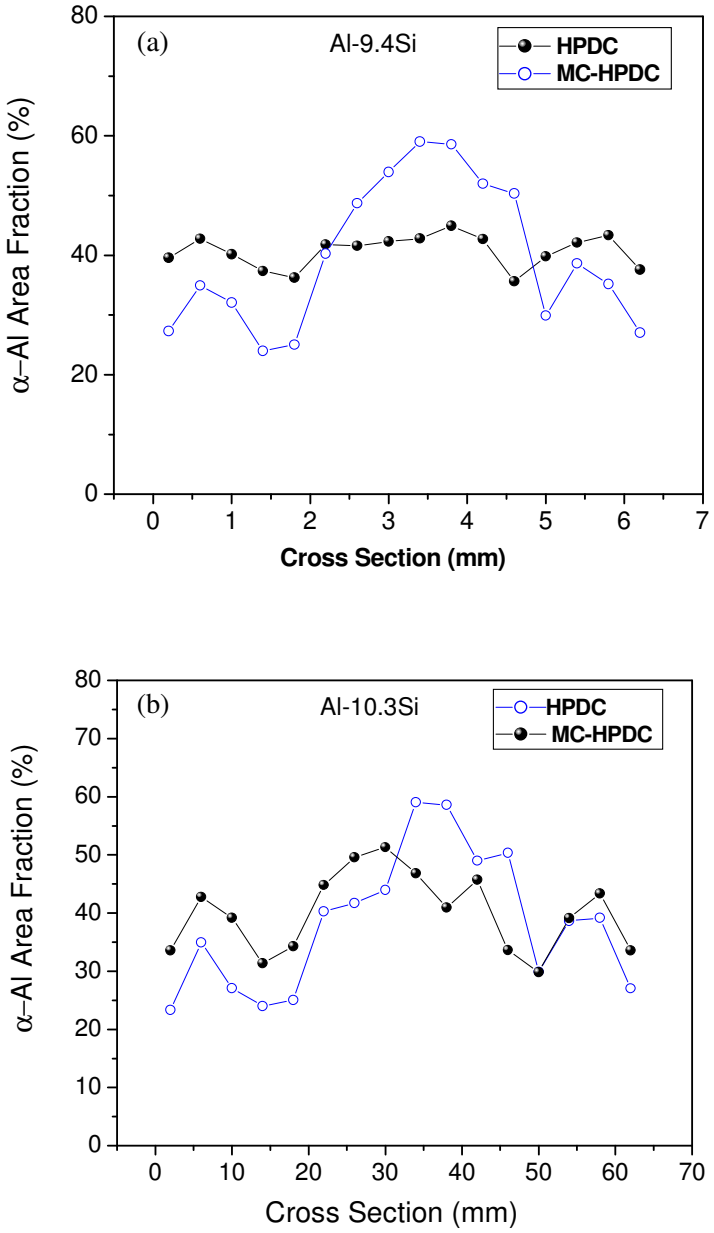

Fig. 5.12. Spatial variation of area fraction of primary α-Al particles across tensile sample cross sections. Each data point represents the measured area fraction of primary α-Al in a total area of 450 X 340 μm^2 (a) Al-9.4Si and (b) Al-10.3Si alloys. The spatial variation of primary α-Al phase shown in Fig. 5.12, suggests that the MC-HPDC process results in more uniformly distributed α_1-Al or ESC particles across the sample.

5.3.3 Size, shape and distribution of intermetallic particles

Al-Si alloys have different types of primary intermetallics and their amounts are related to the level of Fe content. A few intermetallic compound particles are spherical in shape, which were identified by EDX quantification as the α-Al(Fe,Mn)Si phase and also the presence of needle-shaped β-AlFeSi was noted. The primary α-Al(Fe,Mn)Si particles exhibit an equiaxed morphology when they are small, and they may develop into more complex morphologies (e.g. cross-like or star-like) with an increase in their sizes, which is consistent with previous work (Barlock *et al.* 1975, Davignon *et al.* 1996). An overall view of the coexistence of the primary α-Al(Fe,Mn)Si and β-AlFeSi compounds is shown in Fig. 2.9.

The α-Al(Fe,Mn)Si and the β-AlFeSi exist mainly as primary compounds. The major difference in the compositions of the α-Al(Fe,Mn)Si and β-AlFeSi phases is in their Mn and Si contents, making them readily distinguishable by both appearance and morphology. Intermetallic phases could be easily identified by EDX quantification, due to their significantly different compositions.

Comparing sheared microstructures to that of their non-sheared samples, it is seen that the effect of shearing on the morphologies of α-Al(Fe,Mn)Si compounds was significant (Figs. 5.13a and b). The long needle-shaped β-AlFeSi primary phase was largely eliminated from the sheared microstructures. Even the rough branching or star-like features of these in the non-sheared samples being largely changed after intensive shearing (i.e. more globular in shape). Scattered primary β-AlFeSi phase was reduced to a disc-like morphology.

The size distribution for α-Al(Fe,Mn)Si particles is shown for both sheared and non-sheared samples in Fig. 5.13c. It can be clearly seen that by applying intensive shearing their average size has been reduced from ~8 μm to ~5 μm and the narrow size distribution suggests that sheared samples have a negligible density of large α-Al(Fe,Mn)Si particles of size >14 μm. The absence of large particles will have a significant role in improving the mechanical properties, particularly the ductility. The result of the Quadrat method (Karnezis *et al.* 1998) calculations are in accordance with the optical observations made from the microstructure. They are given in Fig. 5.13d as a frequency of the number of particulates per Quadrat, N_q, together with the corresponding

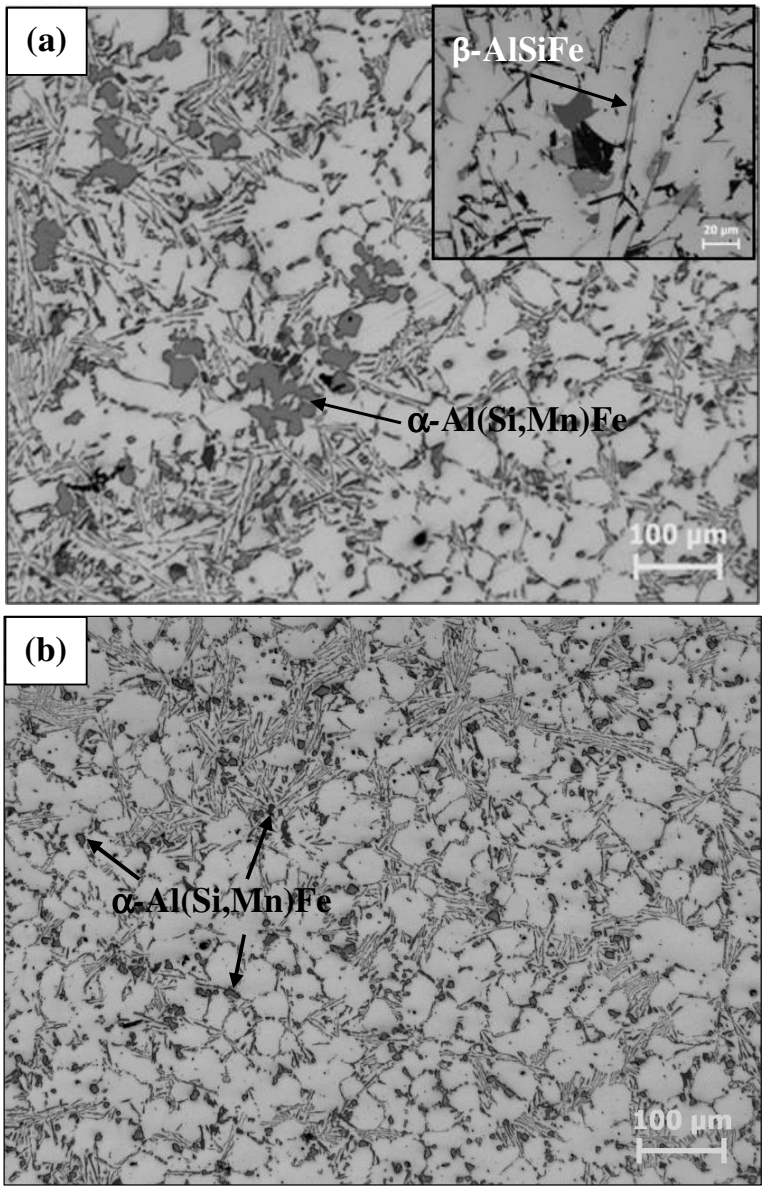

Fig. 5.13. Optical micrographs taken from TP-1 samples (a) non-sheared (inset shows needle-shaped β-AlFeSi intermetallic phase) and (b) sheared, where the angular/or spherical particle is α-Al(Si,Mn)Fe. Optical micrographs show that α-Al(Si,Mn)Fe particles in an intensively sheared sample are distributed uniformly and are small in size compared to a non-sheared sample. The pouring temperature of the samples was 630 °C (*Fig. 5.13 continues to next page*).

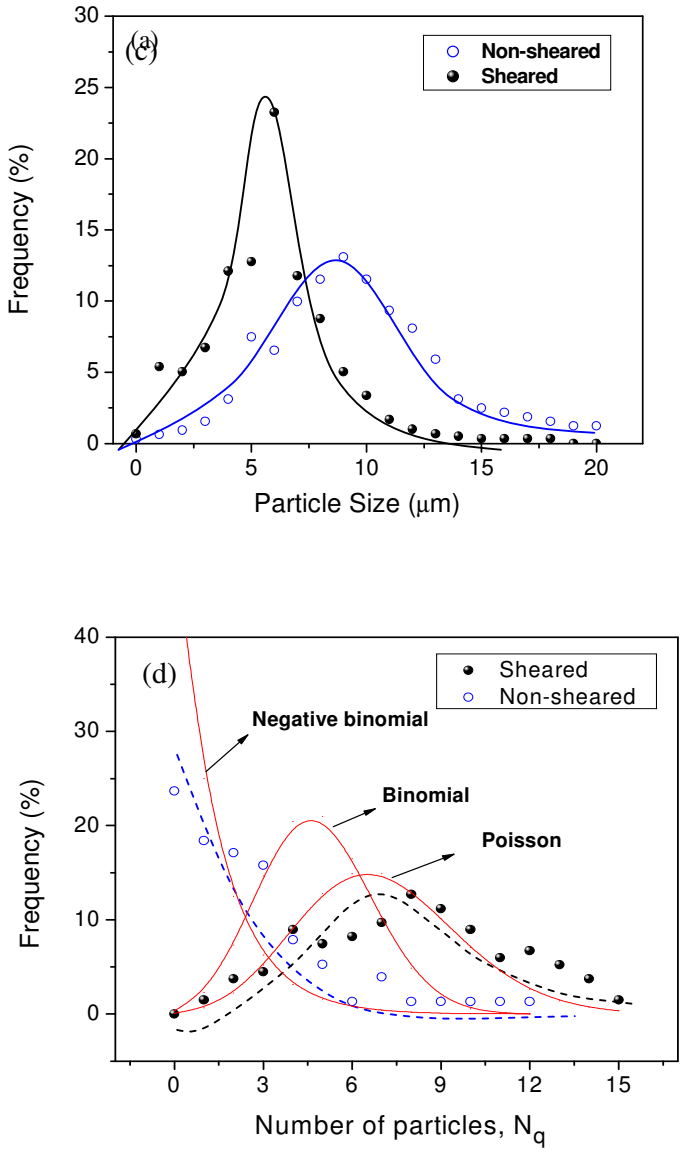

Fig. 5.13. Quantitative analysis (c) α-Al(Si,Mn)Fe particle size distribution curves from 8 random micrographs and (d) particle group number, *Nq* (number of particles per Quadrat) distribution. In Fig. 5.13d solid lines are fits to various statistical distribution curves. The pouring temperature of the samples was 630 °C**.** Fig. 5.13a reveals that intensively sheared samples have higher number of particles which are close to 5 μm in size while non-sheared samples have particles which are 8 μm in size. Fig.13b reveals that the overall distribution of α-Al(Si,Mn)Fe particles is improved by intensive shearing compared with non-sheared samples.

theoretical curves. The magnitude of clustering affects the shape of the N_q distribution, with a higher clustering tendency making the N_q distribution less symmetric. As proven mathematically (Rogers 1974), a clustered spatial distribution follows the negative binomial model, a random spatial distribution follows the Poisson model and a regular spatial distribution model follows the binomial model. The observed particle distribution for the non-sheared samples lie closer to the negative binomial curve indicating clustering, whereas the sheared sample particle distribution resembles more the Poisson and binomial curves.

5.3.4 Porosity

Generally in the HPDC process three different types of pores are observed such as gas pores, shrinkage porosity, and entrained gas porosity (Street 1986). Due to the nature of the HPDC process and the solidification direction of the casting, porosity associated with shrinkage is found in most cast products. It is also known that molten aluminium is very susceptible to hydrogen absorption. Both these factors can lead to porosity in the final components. Porosity on the surface or just beneath will act as a stress raiser and subsequently to crack initiation (Campbell 1997).

The small and approximately round dark areas scattered in the microstructure shown in Fig. 5.14 were identified as gas and shrinkage pores at high magnifications. Macro porosity varying from a few to hundreds of micrometres was noticed in most tensile samples produced by HPDC. In addition, a larger amount of porosity was present in the centre of the cross section where the area fraction of ESC is higher. The SEM analysis and previous work from BCAST suggest that shrinkage porosity was frequently associated with the morphology and distribution of the primary α-Al phase for hypoeutectic alloys, which is most frequently observed in between coarse α-Al primary dendrites (Fig. 5.14b). The samples produced by the MC-HPDC process, where micro

Note:

- The solidification of aluminium is dendrites and will force the gas in the melt to form fine (0.2-0.5 mm in diameter) (Campbell 1997) gas pores; this is true gas porosity.
- When tensile stresses are present during the solidification due to shrinkage in the casting, a low pressure will be created and any gas in the melt will migrate to this low-pressure spot in the casting; this is called shrinkage porosity.
- Entrained gas due to turbulent flow will float to the surface given enough time; any oxide film (Campbell 1997) in the bubble's vicinity will attach itself to the bubble. This will add to the downward force of the bubble by increasing its mass and resistance to flow. This will in all probability trap the bubble in the melt.

and shrinkage porosity were observed only occasionally, the micro pores were found to be usually smaller than in the HPDC samples. A substantial difference was recorded in the occurrence of porosity by quantitative analysis (Fig. 5.15). Samples produced by the HPDC process generally showed a level of porosity of about ~1% area fraction, while those produced by the MC-HPDC process showed approximately 0.3% area fraction.

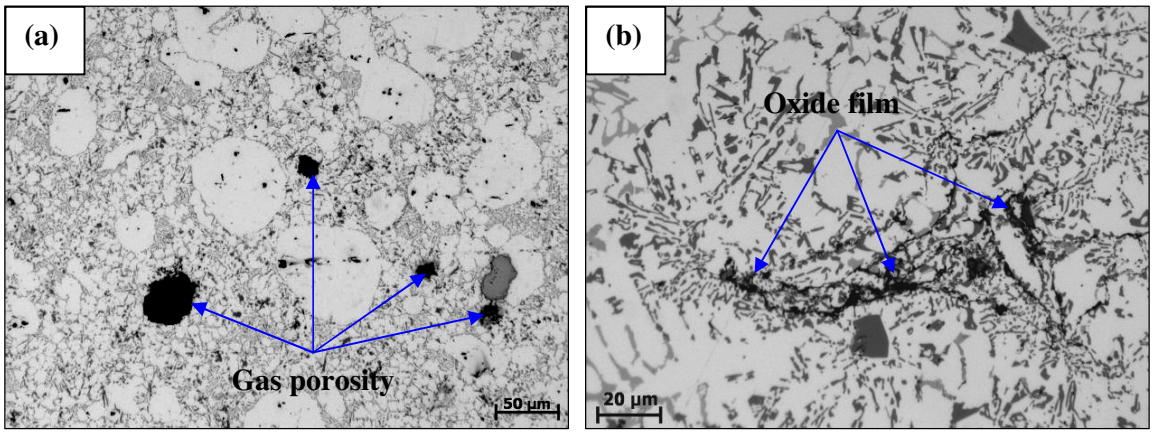

Fig. 5.14. Optical micrographs of Al-9.4Si alloy showing (a) gas porosity (micrograph taken from an MC-HPDC sample) and (b) oxide film (micrograph taken from a TP-1 sample)

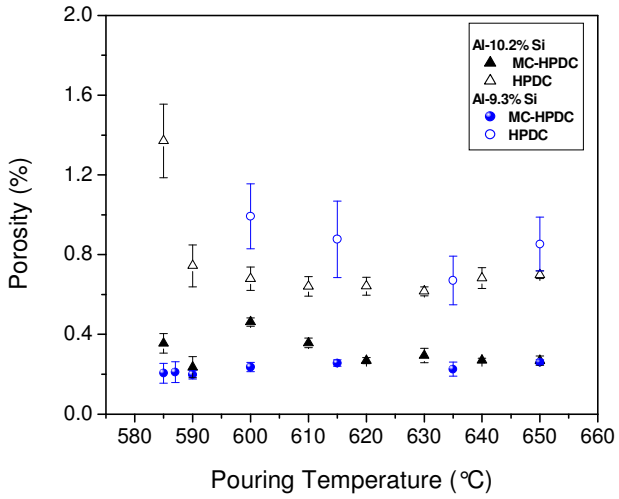

Fig. 5.15. Area fractions of porosity as a function of the pouring temperature (T_p) from tensile test samples. The samples were produced by the HPDC and MC-HPDC processes. HPDC tensile samples showed a level of porosity of about ~1% area fraction, while those produced by the MC-HPDC process showed about ~0.3% area fraction.

5.3.4.1 Shrinkage porosity measurements

Al-9.4Si alloy was used to study the effect of intensive shearing on shrinkage and micro porosity. A Tatur test was used to make qualitative and quantitative measurements of micro and macro (pipe, slumping and contraction) porosity. The experiments were carried out in wide-based cone mould (Fig. 3.7) which leads to the formation of different types of porosity in the casting as illustrated in Fig 3.8.

In order to study the solidification and porosity distribution pattern, Tatur samples were cut vertically almost exactly into two equal halves along the pipe. Fig 5.16 compares the macrostructures of Al-9.4Si alloy Tatur shrinkage samples produced by both the conventional and the MCAST processes. The conventional sample cast at 720 °C has a large columnar grain structure close to the edge of the sample and large grained equiaxed structure towards the centre of the sample. The MCAST Tatur shrinkage sample shows a fully fine equiaxed grain structure throughout the entire cross section. Further, Fig. 5.17 is given to see more clearly the nature of the grain structure of both the conventional and MCAST Tatur shrinkage samples. It can readily be seen from the colour image that the conventional sample consists of a typical columnar structure with a grain size up to the millimetre scale in the edge region and an equiaxed grain structure towards the central region of the sample cast at 720 °C. By contrast, application of intensive shear to the liquid metal prior to casting, avoids the columnar grain growth by favouring the formation of a fully equiaxed structure with an average grain size of 350 μm. Previous work concluded that under the same casting conditions, the grain size of a conventional casting is strongly influenced by the melt superheat but the dependence of the grain size on the superheat is substantially less for sheared samples (Fan *et al.* 2009a).

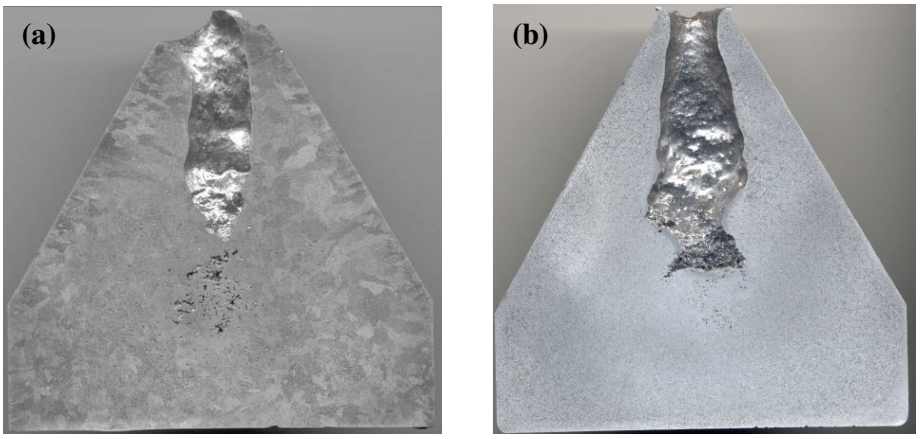

Fig. 5.16. Image showing macro structure of Tatur shrinkage samples for the Al-9.4Si alloy; finer and more uniform microstructure can be seen in the MCAST sample (a) Conventional sample at a pouring temperature of 720 °C and (b) MCAST sample pouring temperature is 615 °C, above the melting point; shearing speed 500 rpm for 60 s).

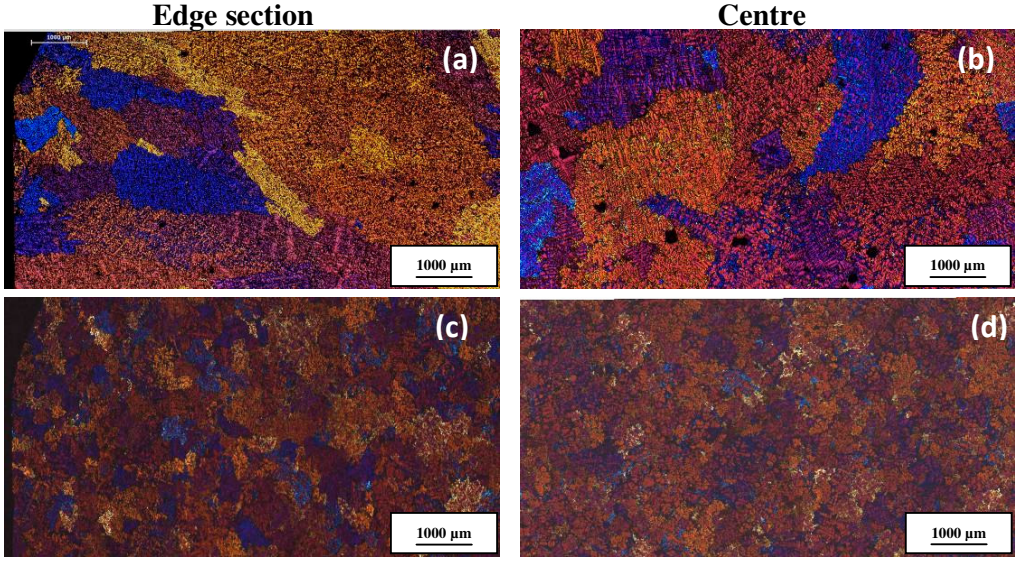

Fig. 5.17. Microstructures of Tatur samples for the Al-9.4Si alloy produced by (a),(b) conventional and (c), (d) MCAST method. The Conventional sample at a pouring temperature of 720 °C and MCAST sample pouring temperature is 615 °C, above the melting point; shearing speed 500 rpm for 60 s.

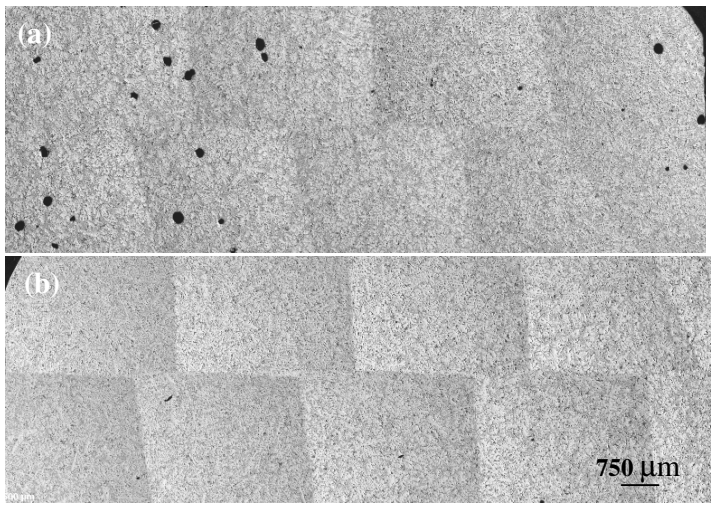

Fig. 5.18. Low magnification optical view of porosity in Tatur samples of Al-9.4Si alloy cast at a pouring temperature of 615 °C showing no visible porosity at this magnification in the MCAST sample (a) conventional and (b) MCAST sample.

Fig. 5.18 is a typical low magnification optical microscope view of Tatur shrinkage samples from edge towards the centre of an Al-9.4Si alloy sample. It is hard to see the presence of any large pores in the MCAST sample compared to the conventional sample and the variation in the porosity size and number as a function of pouring temperature for conventionally cast Al-9.4Si alloy is shown in Fig. 5.19, where not much change in pore size (up to 400 µm) is seen between a pouring temperature of 720 and 615 °C for conventional cast samples. It has to be mentioned that the sample cast at the higher pouring temperature of 720 °C has a larger number of pores. By contrast, it is hard to see the presence of pores at low magnification for the MCAST sample as can be seen in Fig. 5.18b. A high optical magnification study was undertaken and the size of the porosity is plotted in Fig. 5.19. In this case only 50 pores were included in the MCAST sample. The pore size in the MCAST sample was very much less than 50 µm, however, pores with a size up to 400 µm were observed for the conventional samples. Fig. 5.20 illustrates typical patterns of pores in the central regions close to the end of the pipe of conventional and MCAST samples poured at the same pouring temperature of 615 °C. An

interconnected network of porosity can be seen for both samples; however, a larger size is noted for the conventional sample compared to the MCAST sample.

The measured apparent densities of Al–9.4Si alloy Tatur sample produced by both the MCAST and conventional method are given in Table 5.1. The lowest apparent density of 2.765 g/cm^3 was noted for the samples cast conventionally when the pouring temperature was 720 °C. An increase in the apparent density in Al-9.4Si alloys was observed by the application of the MCAST process. The apparent density of conventional and MCAST processed Al-9.4Si alloy samples is 2.773 and 2.783 g/cm^3, respectively. As can be seen from Table 5.2, a higher pouring temperature (720 °C) gives a higher volume percentage of micro porosity. This is expected because of the decreased apparent density. It can be concluded that the application of intensive shearing gives less micro porosity than in non-sheared samples.

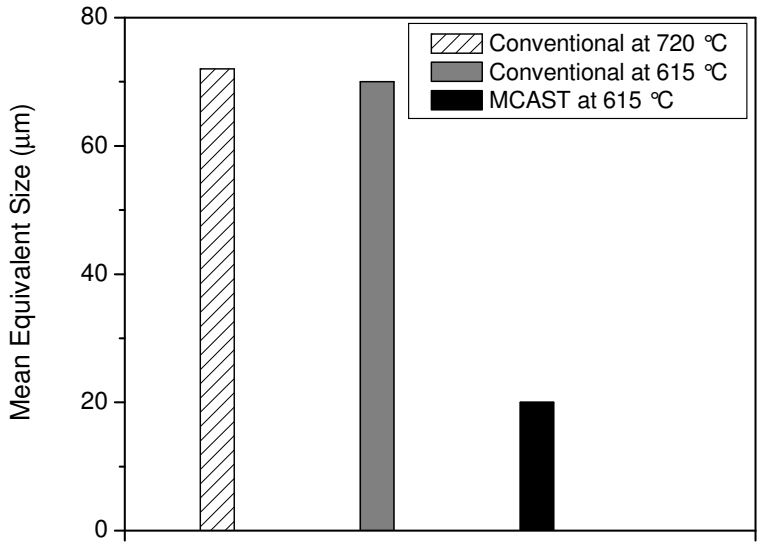

Fig. 5.19. Variation of individual pore size as function of pouring temperature and casting process for the Al-9.4Si alloy; pores with a mean size of 72 µm can be seen for the conventional sample but only up to 20 µm for the MCAST sample.

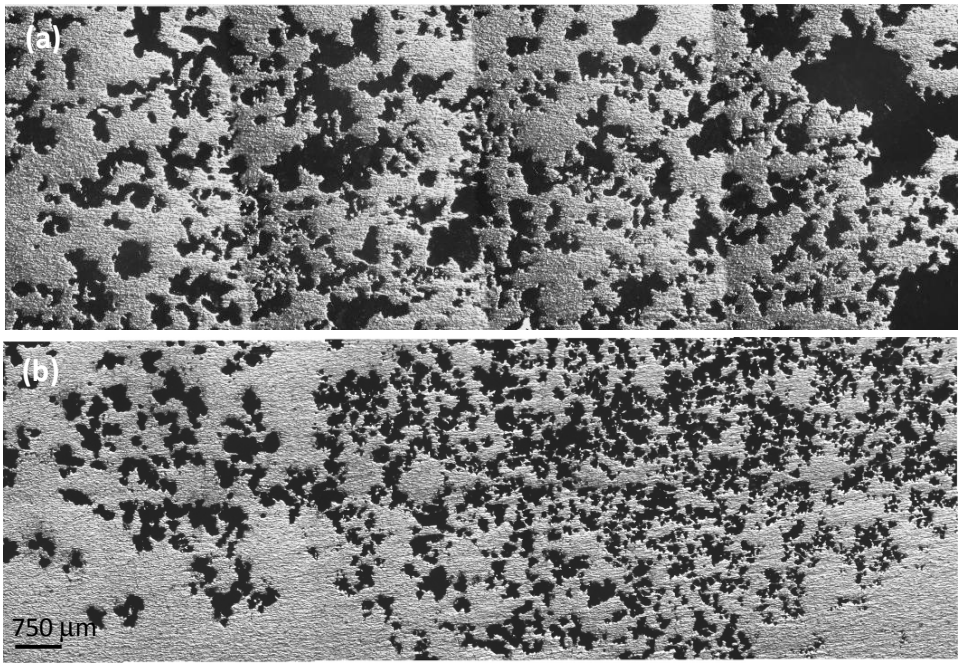

Fig. 5.20. Comparison of porosity in the central part of Tatur shrinkage samples cast at a pouring temperature of 615 °C for the Al-9.4Si alloy (a) conventional and (b) MCAST.

Table 5.1. Al-9.4Si alloy non-sheared and sheared samples density measurement.

Pouring Temperature (°C)	Apparent Density (g/cm^3)	
	Conventional Method	MCAST Method
720	2.765	-
635	2.784	2.788
615	2.773	2.783

Table 5.2. Al-9.4Si alloy non-sheared and sheared samples shrinkage porosity measurement using a shrinkage mould, where a = volume of micro-shrinkage cavities; b = volume of macro-shrinkage cavitations (pipe); c = volume of slumping and contraction (Fig. 3.8). Note that results are volume percentage of Tatur volume. For calculation method see appendix II.

Condition	Non Sheared				Sheared			
	a	b	c	Total	a	b	c	Total
720°C	0.82	3.71	2.97	7.50	-	-	-	-
650°C	0.37	3.46	2.76	6.59	0.08	3.50	3.18	6.76
635°C	0.34	3.53	3.39	7.27	0.24	3.57	3.11	6.93
615°C	0.59	2.42	4.49	7.50	0.23	3.36	3.09	6.68

5.3.5 Grain size

It can be seen from the previous section that the microstructures of samples produced under intensive shearing using the MCAST unit, are finer and more homogeneous compared to the conventional gravity cast microstructure. Application of intensive shearing suppresses the dendritic and columnar grain formation, as a result a fine and uniform microstructure is produced. Additionally Fig. 5.21 illustrates the grain size of the Al-10.3Si alloy cast at different pouring temperatures under TP-1 mould conditions (section 3.4.3). The average grain size was calculated by the liner intercept method by analysing 15 micrographs. To reduce the error in estimation of the grain size, at least 5 lines per micrograph were used. In Fig. 5.22 a graph of the grain size as a function of the pouring temperature clearly reveals that the grain size decreases when the pouring temperature is closer to the liquidus temperature of the alloy. From these results we may conclude that the influence of the melt superheat on the grain size was suppressed and much finer grain structures were obtained under intensive shearing. This is supported by an enhanced nucleation in the sheared samples compared to the conventional cast TP-1

samples, where the grain density increased significantly compared with the conventional TP-1 cast samples. In addition, the conventional cast samples show a significant amount of interdendritic segregation between the dendrites and arms (Kotadia *et al.* 2010).

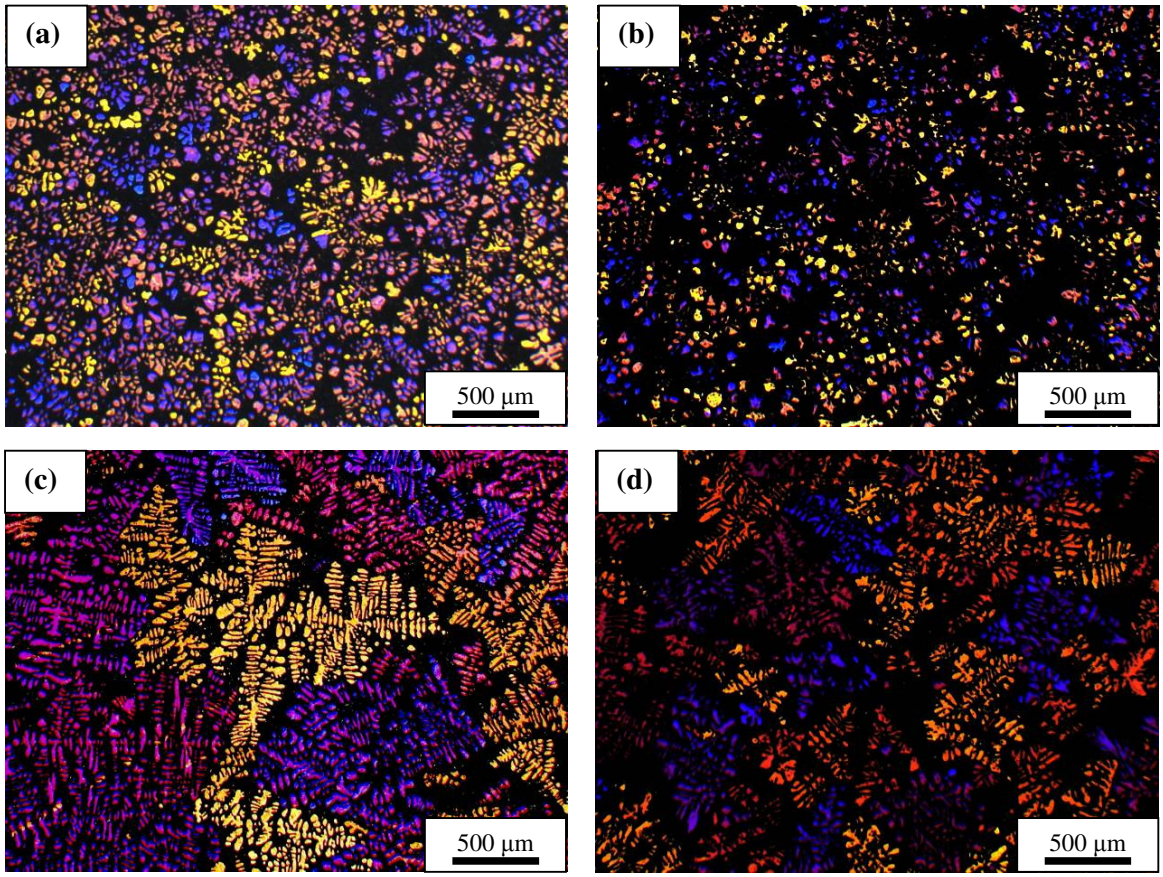

Fig. 5.21. Optical micrographs of TP-1 mould, non-sheared and sheared processed Al-10.3Si alloy, (a) and (c) non-sheared, (b) and (d) are sheared samples; (a) (b) T_p is 590 °C and (c), (d) T_p 650 °C. The MCAST processing conditions were; rotation speed = 600 rpm and shearing time = 60 s. Non-sheared samples have large and fully-grown dendrites compared with the sheared samples.

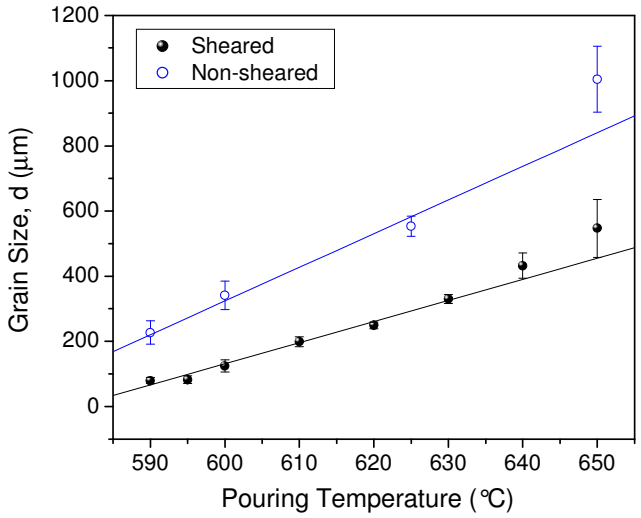

Fig. 5.22. Variation of the grain size as a function of casting temperature for Al-10.3Si cast alloy in a TP-1 mould with and without melt shearing. The results clearly reveal that grain refining occurs by intensive shearing.

5.3.6 The mechanical properties of HPDC and MC-HPDC tensile samples

The substantially reduced macro, micro and shrinkage porosity, combined with the replacement of coarse primary α-Al dendrites by spheroidal aluminium particles in hypoeutectic alloys imparted improved ductility to the MC-HPDC samples of Al-Si alloys. The ultimate tensile strength (UTS) also exhibited an obvious improvement. Fig. 5.23 summarises the tensile properties obtained from samples produced by HPDC and MC-HPDC as a function of the pouring temperature. As can be seen, MC-HPDC samples of Al-Si alloys exhibited a good combination of UTS and elongation, compared to the typical tensile properties of samples produced by the conventional HPDC process. Fig. 5.23 also shows that both strength and ductility of the MC-HPDC samples are almost independent of the pouring temperature within the present pouring temperature range. However, Fig. 5.23 shows the HPDC tensile properties strongly depend on the pouring temperature. For the HPDC samples, the UTS and elongation slightly increased with the pouring temperature. This means that MC-HPDC process provides a larger processing

window than in the conventional HPDC process. These results are encouraging, in that the MC-HPDC process is capable of achieving a slight improvement in strength and ductility of Al-Si alloys while retaining all major advantages of a HPDC process described in section 2.2.4. Mechanical properties of the alloys are measured on tensile samples which have not been heat treated.

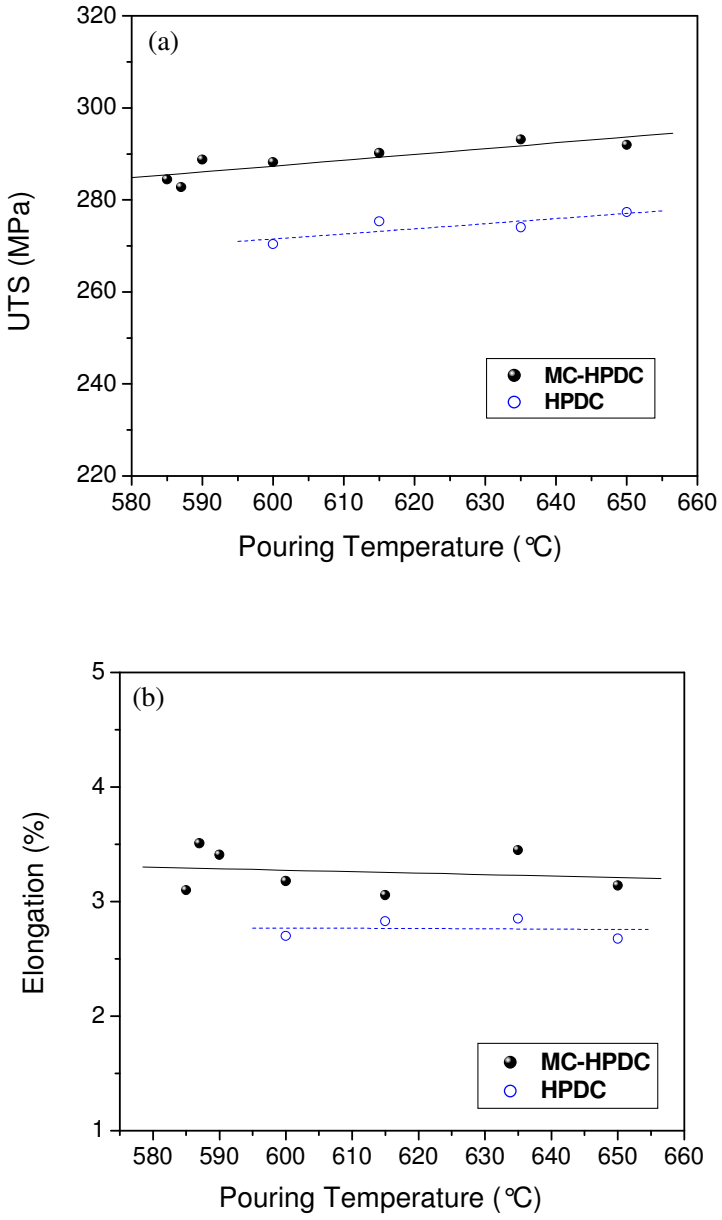

Fig. 5.23. Variation of the Ultimate tensile strength, UTS (MPa) and elongation (%) as a function of the pouring temperature (a),(b) Al-9.4Si alloy (*Fig. 5.23 continues to next page*).

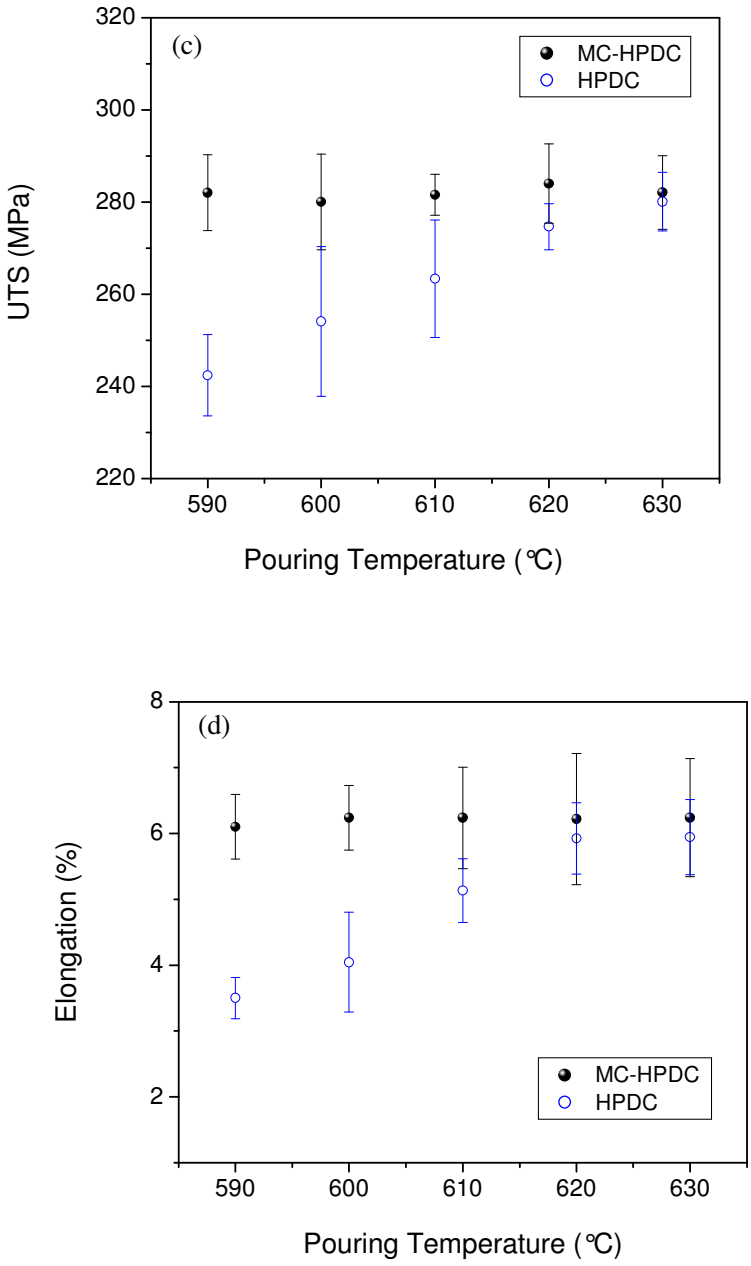

Fig. 5.23. Variation of the Ultimate tensile strength, UTS (MPa) and elongation (%) as a function of the pouring temperature (c), (d) Al-10.3Si alloy.

In addition, statistic distributions of mechanical properties of cast Al-Si alloy was explained with the Weibull distribution (Weibull 1951). The detail explanation about the Weibull distribution is given in appendix IV. The UTS and elongation are plotted on normal probability coordinates in Figs. 5.24 and 5.25.

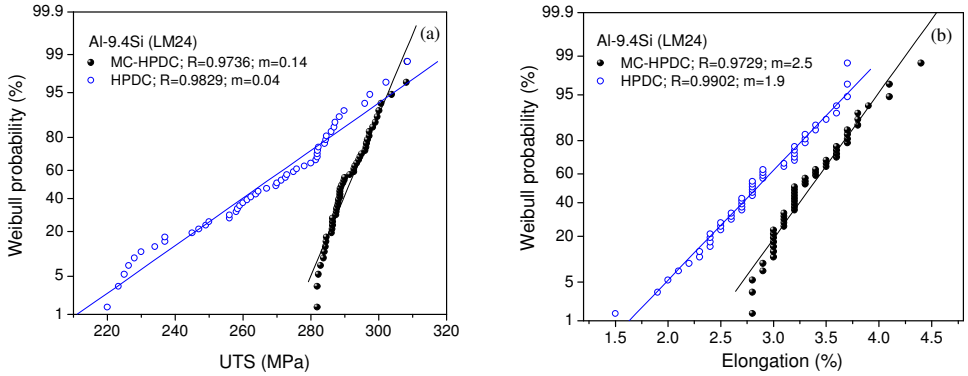

Fig. 5.24. Weibull probability curves of the mechanical properties (a) UTS and (b) elongation for Al-9.4Si alloy HPDC and MC-HPDC process tensile samples.

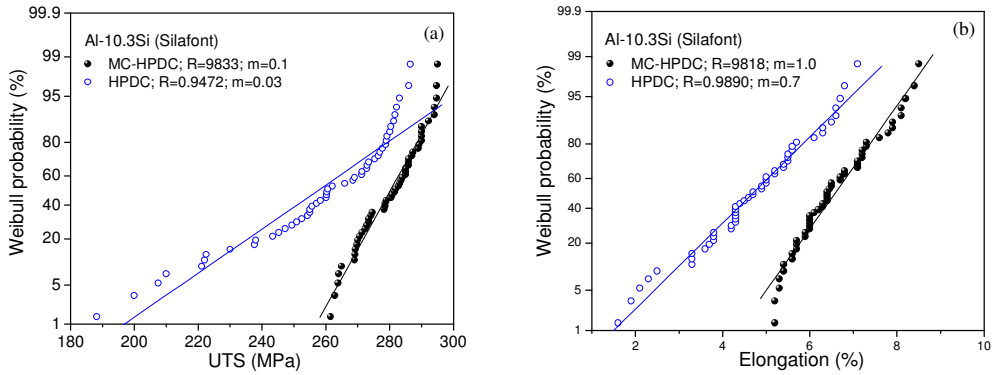

Fig. 5.25. Weibull probability curves of the mechanical properties (a) UTS and (b) elongation for Al-10.3Si alloy HPDC and MC-HPDC process tensile samples.

For an ideal normal distribution, the Weibull probability curve would be a straight line on the normal probability coordinates. The UTS data obtained from HPDC and MC-HPDC process have been analysed using the statistical distributions as described above and their

'goodness of fit' to each is described by the regression coefficient. Prior to the plotting, each of the ranked positions of UTS values (1 = worst) were converted to the failure probability of a population. The statistical significance of the differences can be estimated from the 90% confidence limits. The graph clearly shows a certainty of difference between HPDC and MC-HPDC castings. Figs. 5.24 and 5.25 show the UTS and elongation data followed the normal distribution very well. The slope of the lineally fitted line increased in HPDC process data showing reduced mechanical properties. The experimental analysis shows that the HPDC processes likely to produce bad castings compared with the MC-HPDC process.

5.4 Hypereutectic Al-Si alloy

5.4.1 Shape, size and distribution of the Si phase

The quantitative analysis of the HPDC hypereutectic Al-14Si alloy shows that the primary Si particle size increased from 13 µm to 17 µm by increasing the pouring temperature from 590 °C to 650 °C. In other words, the density (number of particles per unit cross sectional area) of the Si primary particles significantly reduced from 147 to 32 mm^{-2} which is a factor of 78 %. In addition, the microstructures reveal that the number of primary Si particles that were smaller than 5 µm were significantly increased throughout the sample with increased T_p and also revealed that coarsening of the eutectic Si occurred. The flake-shaped eutectic structure that formed at lower T_p, transforms to a globular shape at higher T_p due to coarsening of the eutectic phase.

A similar study was carried out using the MC-HPDC process. The MC-HPDC result shows a significant drop in the Si particle size and the average Si particle size obtained at all the different pouring temperature was ~ 12 µm, which contrasts markedly with the HPDC samples (from 13 to 17 µm) (Figs. 5.26 and 5.27). In addition, the particle size distribution curve clearly reveals that the MC-HPDC sample has a higher number of small particles compared with the HPDC process.

Along with the distribution, the morphology of primary Si particles in the matrix plays an important role in determining the properties of a hypereutectic alloy. In the present study effort has been made to quantify the effect of on the resultant morphology of primary Si particles. Fig. 5.28a shows the sphericity of primary Si particles as a function of

temperature of HPDC and MC-HPDC samples. The HPDC samples had needle-shaped Si particles (Fig.5.26a) with a low sphericity value of ~0.52 ± 0.04. The average sphericity value of Si particles in the MC-HPDC samples was found to be ~0.61 ± 0.06 indicating a relatively spherical morphology.

The shape distributions of primary Si particles (≥ 5 μm) are shown in Fig. 5.28b they show similar behaviour under both HPDC and MC-HPDC conditions prepared at a 640 °C pouring temperature. In the HPDC sample, the Si particles have a broad size distribution that falls off gradually on either side of the peak. In comparison, the MC-HPDC sample showed a consistent shift of the peak in the shape distribution curve to a lower value than that observed in the HPDC sample. It is clear from Fig. 5.28 that the melt conditioning treatment was successful in modifying the Si particles into the desired more spherical morphology.

Defect bands in hypereutectic alloys are difficult to identify. However, defect bands were measured from the outer surface of tensile samples and could be identified as they were composed of a larger volume of eutectic phase. Fig. 5.26 shows a cross sectional view of a tensile bar produced at 620 °C. There is strong indication that defects bands do exist in this alloy (Fig. 5.29). Fig. 5.30 reveals three different regions of the defect band in the hypoeutectic alloy. Inside the band region more eutectic phase is segregated, which is similar to that of the hypoeutectic alloys.

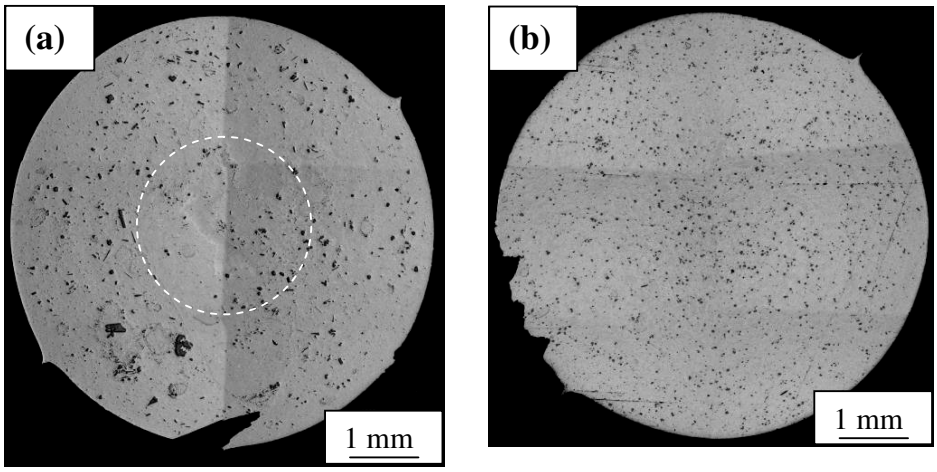

Fig. 5.26. Optical micrographs from tensile sample cross sections (a) HPDC and (b) MC-HPDC, pouring temperature was 620 °C. The MC-HPDC tensile samples have small size Si particles with a spherical shape and better uniformity in the overall cross-section.

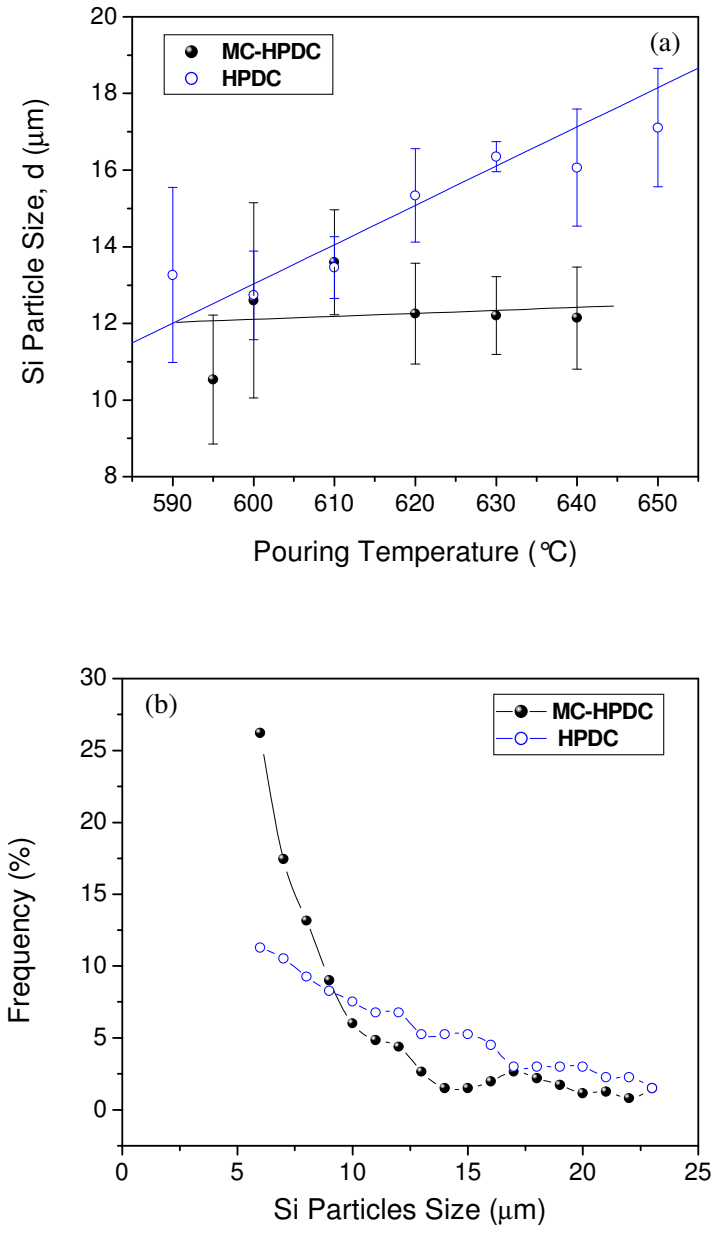

Fig. 5.27. Quantitative analysis of Al-14Si alloy (a) Variation of primary Si particles (≥ 5 μm) as a function of pouring temperature and (b) distribution curve for Al-14Si alloy primary Si particles (≥ 5 μm) processed at 640 °C.

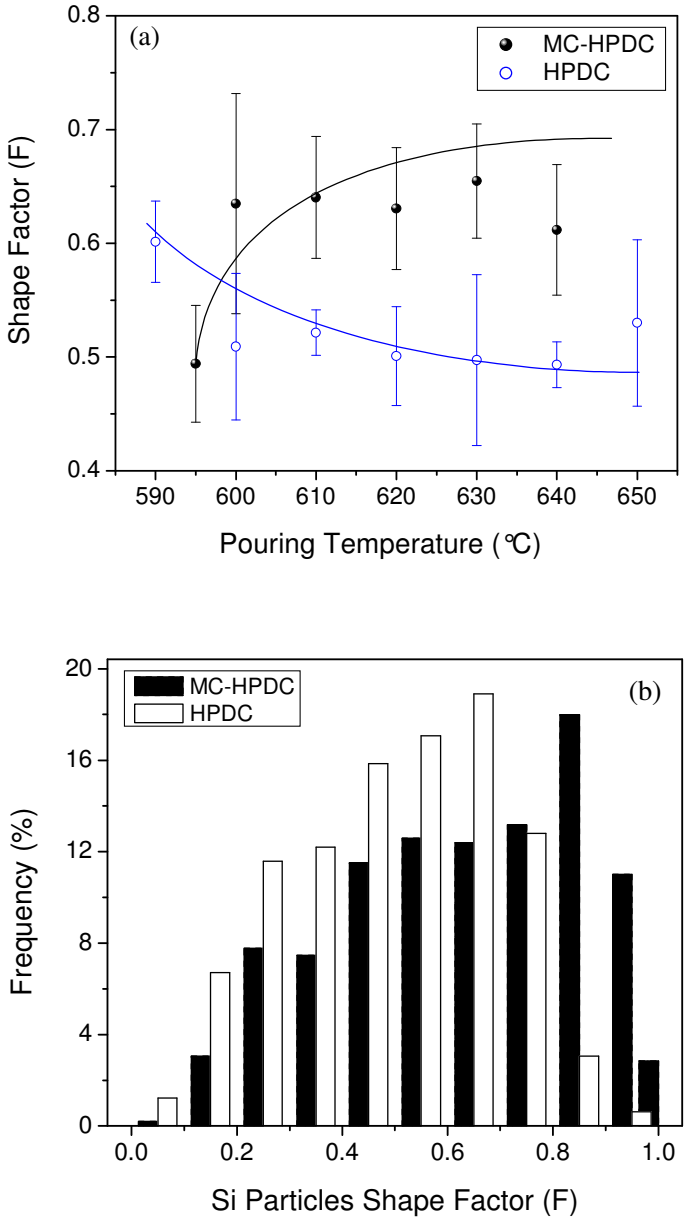

Fig. 5.28. Al-14Si alloy prepared in HPDC and MC-HPDC at 640°C (a) shape factor as a function of the pouring temperature and (b) histograms showing the Si sphericity distribution in conventional HPDC and MC-HPDC samples. Sample pouring temperature was 640 °C.

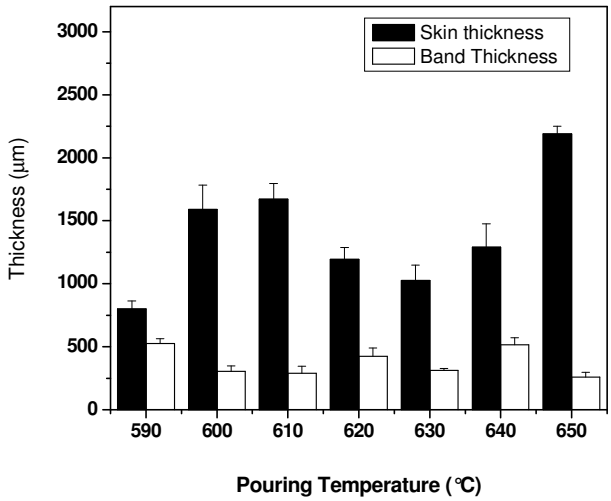

Fig. 5.29. Al-14Si alloy skin and band thickness as a function of pouring temperature for HPDC samples.

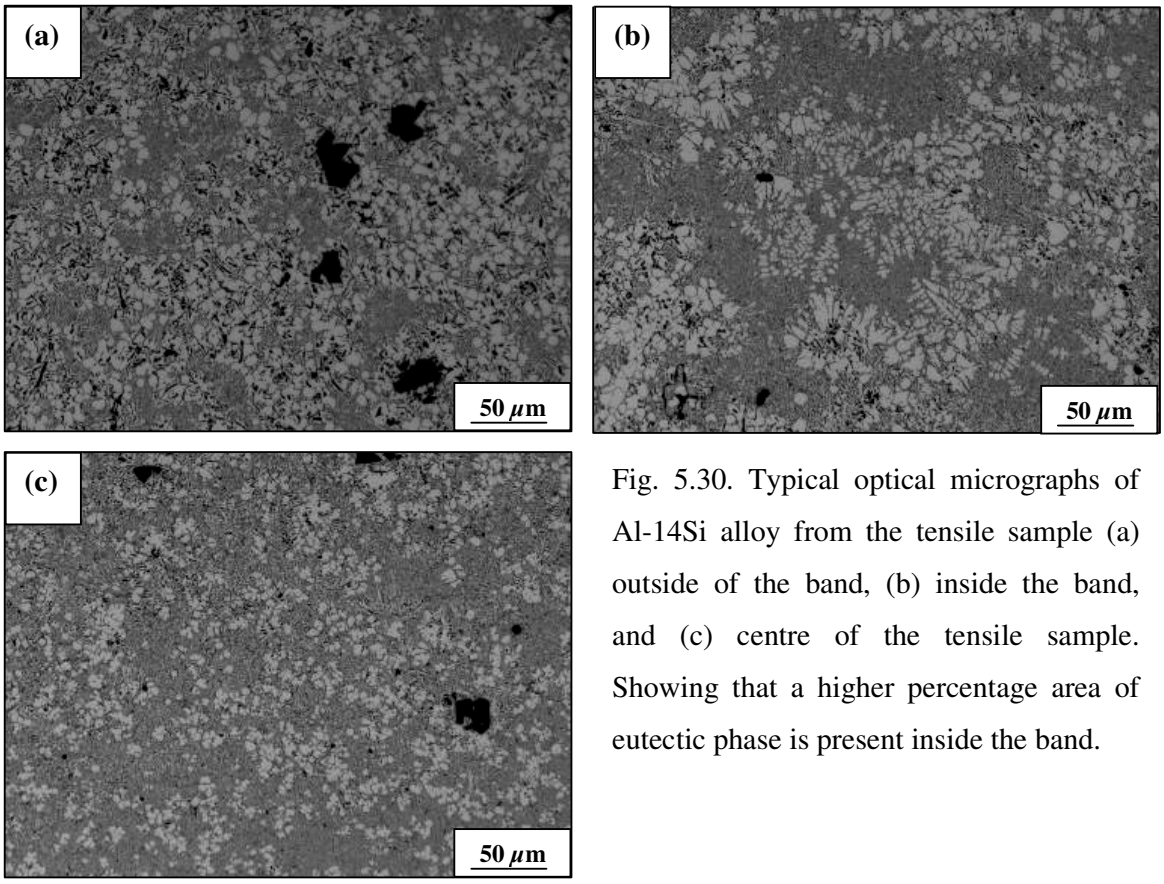

Fig. 5.30. Typical optical micrographs of Al-14Si alloy from the tensile sample (a) outside of the band, (b) inside the band, and (c) centre of the tensile sample. Showing that a higher percentage area of eutectic phase is present inside the band.

5.4.2 Mechanical properties of HPDC and MC-HPDC samples

It is well known that, both the structure and properties of Al-Si alloys are extremely sensitive to the fabrication technique. The distribution and morphology of primary Si particles have an important bearing on the mechanical properties of a hypereutectic Al-Si alloy. With a view to extending their applications to structural components, these materials should have a good combination of strength and ductility. Fig. 5.31 illustrates that compared with the conventional HPDC process; the MC-HPDC process provides samples with a slightly higher ultimate tensile strength and much higher tensile elongation to failure.

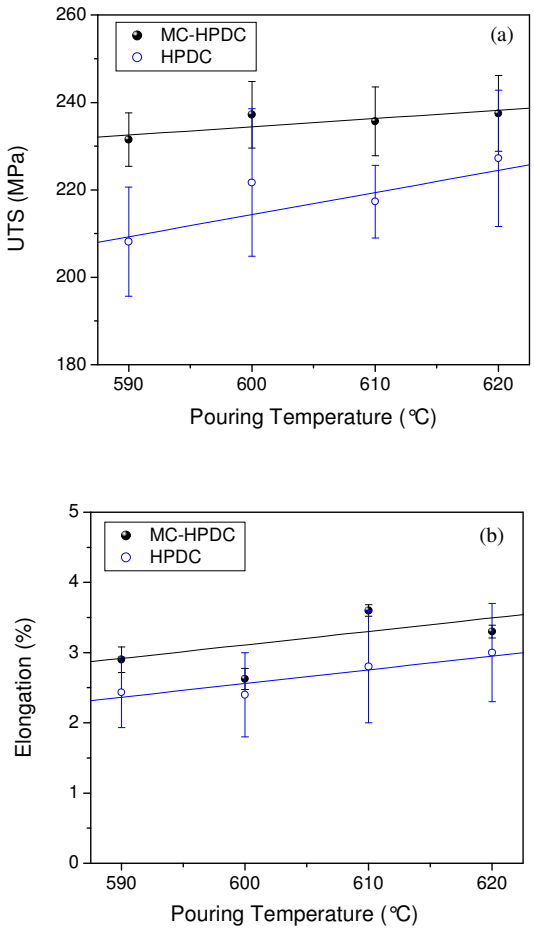

Fig. 5.31. Variation of the Ultimate tensile strength, UTS (MPa) and elongation (%) as a function of the pouring temperature of the Al-14Si alloy.

5.5 Summary

The effects of pouring temperature and intensive shearing on microstructural and mechanical properties of hypoeutectic and hypereutectic Al-Si alloys have been investigated systematically.

Hypoeutectic Al-Si alloy

- In HPDC experiments, increasing the pouring temperature from the liquidus temperature, the externally solidified crystals (ESCs) reduced significantly, which in turn, contributed to an increased area fraction of small primary α-Al particles and better uniformity of the eutectic phase in the whole volume of the sample.

- The defect band thickness was reduced with an increase in the pouring temperature. At a higher pouring temperature, the defect band location moved towards the centre of the sample. Changes in microstructural features such as defect band thickness, and skin thickness have a direct correlation with the observed mechanical properties.

- A large dendritic morphology was obtained under conventional solidification processing conditions. In contrast to conventional processes, the intensive shearing significantly refined the structure and highly globular α-Al grains were obtained throughout the volume of the solidified sample. In addtion, intensive shearing at the liquidus temperature improved the distribution of the α-Al(Mn,Fe)Si intermetallic phase with a narrow distribution and average α-Al(Mn,Fe)Si intermetallic particle size reduced from 8 μm to 5 μm.

- The intesively sheared samples had significantly reduced porosity in tensile samples. Samples produced by the HPDC process generally showed a level of porosity of about ~1% area fraction, while those produced by the MC-HPDC process showed approximately ~0.3% area fraction.

- The ultimate tensile strength (UTS) and elongation (%) for MC-HPDC samples of the hypoeutectic Al-Si alloy were better than for HPDC samples.

Hypereutectic Al-Si alloy

- Defect bands were observed in both sheared and non-sheared HPDC tensile samples and some samples illustrate multiple defect bands. However, there is no evidence observed in the change of defect band in the hypereutectic alloy in the current study with respect to pouring temperature.
- The intensively sheared samples had significantly improved the morphology and distribution of primary Si particles.
- The ultimate tensile strength (UTS) and elongation (%) for MC-HPDC samples of the hypereutectic Al-Si alloy were slightly better than for HPDC samples.

Chapter 6
Al-Sn-Cu and Al-Si Alloys Discussion

6.1 Introduction

Fundamental investigations performed in Al-Sn-Cu and Al-Si alloys, show that the melt conditioning by advanced shearing technology (MCAST) unit, developed by BCAST, Brunel University, can be used in the processing of these alloys in various applications. In this chapter, discussion is mainly concentrated on two different alloy systems Al-Sn-Cu immiscible alloys and Al-Si cast alloys. The microstructural evolution is explained with well understood theory and/or hypothesis.

6.2 Al-Sn-Cu alloys

Under conventional foundry conditions, immiscible alloys exhibit serious segregation and layered structures after solidification. In this investigation, we have used intensive shearing by an MCAST unit with the aim to produce a homogeneous microstructure. Under this condition immiscible alloys solidified without segregation because the second phase (i.e Sn in the Al-Sn alloy) droplets no sooner emerged than were trapped by the matrix phase (i.e Al in the Al-Sn alloy). The following section is focused on a study of the solidification path of ternary Al-20Sn-10Cu and Al-45Sn-10Cu immiscible alloys and the mechanism to produce fine and uniform microstructures under the intensive shearing condition is discussed. Comparison has been made between the conventionally cast and MCAST specimens.

6.2.1 Microstructural evolution during gravity die-casting

As mentioned in chapter 4, the solidification paths of the two chosen alloys are expected to differ significantly in the first stages. While the Al-45Sn-10Cu shows demixing of the liquid phase before commencement of solidification, the Al-20Sn-10Cu first shows precipitation of Al before demixing occurs. This can be seen in the microstructures of each alloy after conventional casting in a metallic mould shown in Figs. 4.6a and b. The most significant difference between these two micrographs is the agglomeration of Sn (white phase in SEM images) in the Al-45Sn-10Cu sample (Fig. 4.6a), while Sn in the Al-20Sn-10Cu sample (Fig. 4.6b) is regularly distributed between the other phases in the microstructure, indicating that the liquid separation occurred after primary solidification in the Al-20Sn-10Cu sample. In the following discussion, the microstructural formation in each sample alloy will be discussed with respect to the calculated solidification path which is also shown in the phase fraction diagrams in Fig. 4.2 as well as the measured DSC signals traces, shown in Fig. 4.3.

The sequence of phase separation/ formation of the Al-45Sn-10Cu alloy according to Calphad calculations are given below:

Phase formation temperature	Phase formation	Eq.
above 587 °C	L,	6.1a
between 587 to 558 °C	$L \rightarrow L' + L''$,	6.1b
between 558 to 524 °C	$L' + L'' \rightarrow L' + (Al) + L''$,	6.1c
at 524 °C (monotectic reaction)	$L' = L'' + (Al) + \theta\text{-}Al_2Cu$,	6.1d
between 524 to 227 °C	$L'' \rightarrow (Al) + \theta\text{-}Al_2Cu$,	6.1e
at 227 °C (eutectic reaction)	$L'' \rightarrow (Sn) + (Al) + \theta\text{-}Al_2Cu$	6.1f

When the Al-45Sn-10Cu sample is cooled below the surface of the liquid miscibility gap (587 °C) droplets of L″ liquid begin to separate from the prior L (Eq. 6.1b). These droplets are nucleated mainly in the areas near the wall of the casting, where the undercooling is greatest. As the composition of these liquids is originally quite similar,

the interfacial energy, and therefore the measurable enthalpy effect of this reaction, is very low. As a result, no signal can be detected in the DSC experiment. Over the next 30 °C, the amount of L″ grows and the droplets move uninhibited through the melt, coagulating as they settle and grow. The motion of L″ droplets through the unstirred melt can be attributed to two factors. The first factor affecting the direction of droplet motion is the denser nature of the Sn-rich L″ (dark grey in the OM images) than L′ (white in the OM images) in Fig. 6.1. Therefore, L″ droplets sink toward the bottom of the casting due to gravity (Fig. 6.1a), which is described by the well-known Stokes motion, for the settling velocity (Ratke 1993, Ratke and Diefenbach 1995, Ratke *et al.* 1996, Zhao and Ratke 2004). The second factor affecting the direction of droplet motion is the temperature gradient. The droplets migrate from a low temperature region to high temperature regions, described by the well-known Marangoni motion (Curiotto *et al.* 2006, Munitz and Abbaschian 1996, Ratke 1993, Ratke and Diefenbach 1995, Robinson *et al.* 1999). When a droplet has a melt with temperature gradient, ∇T, a thermocapillary convection in/around the droplet is induced. The droplet surface is drawn from the hotter poles towards the colder poles in order to lower the surface energy. The consequence is the motion of the droplet towards the hot region (Wu *et al.* 2003, Wu and Ludwing 2005). When the local temperature drops below the bimodal point at 598 °C, Sn droplets start to nucleate and grow at the casting surface. The Marangoni force causes the droplets to move from outer regions towards the casting centre (Fig.6.1a). The Al rich melt moves in reverse direction. The droplet motion results in a depletion of the secondary liquid phase in the corners and outer region, and an enrichment of the casting centre. When the cast melt reaches the monotectic point, the monotectic reaction occurs, and the droplets are entrapped in the monotectic matrix. After the final solidification the outer regions of the casting have a lower volume fraction of Sn droplets whereas the centre has a higher one (Wu *et al.* 2005). In the current experiment, the presence of gravitational force and density difference between Sn and Al liquid cause Sn droplets to segregate to the base of the ingot. The OM images in Fig. 6.1b reveal that the motion of the Sn droplets, as indicated by their elongated shape is perpendicular to the main axis of the mould. Both hydrodynamic effects coupled to external fields are explained in chapter 2. The Al rich dendrite nucleates near the mould wall and dendritic tip front moves inwards. The Al rich dendrites solidification pattern agrees with the classical explanation of steel ingot solidification by Campbell (1997).

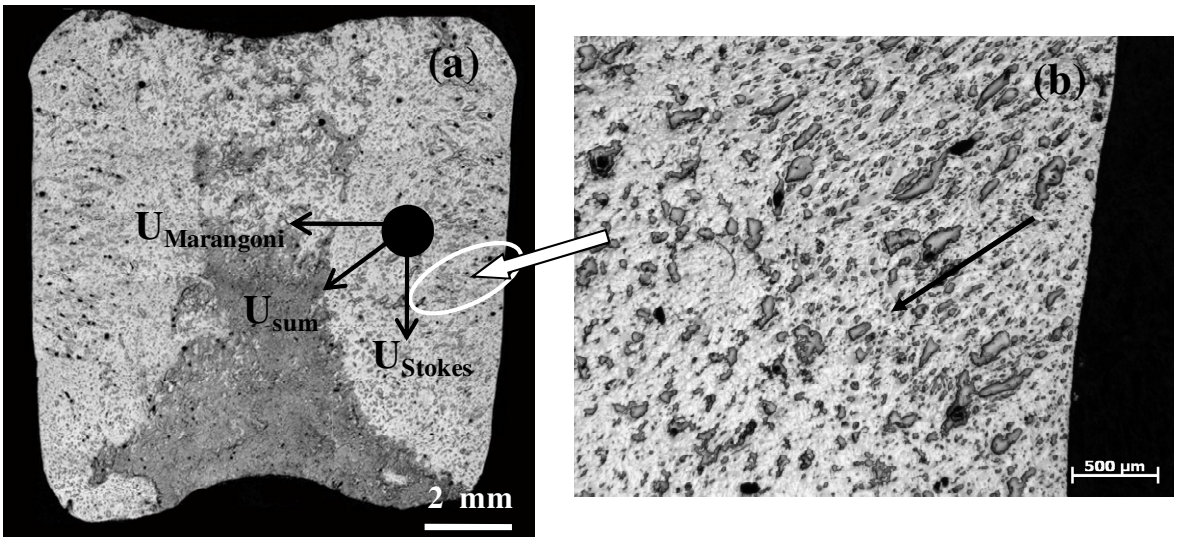

Fig. 6.1. (a) OM image of phase separation in the Al-45Sn-10Cu alloy of L′ (white in contrast) and L″ (dark grey in contrast) liquid in the conventional solidification process (sample cast into a steel mould directly from 650 °C); and (b) OM image from the mould wall indicating that the (Sn) droplets migrate toward the centre of the mould driven by Stokes and Marangoni motions.

Upon further cooling of the Al-45Sn-10Cu sample, an Al solid solution and more L″ is formed from the L′ phase (Eq. 6.1c and d). The first (most right-hand) signal on the DSC curve marks the beginning of this precipitation reaction at 559.5 °C. This is closely followed by the monotectic reaction, $M: L' = L'' + (Al) + \theta\text{-}Al_2Cu$ occurring in the regions which are dominated by L′. This reaction occurs at 524 °C according to the calculation and at 526.8 °C in the DSC measurement. The fine microstructure corresponding to this stage of solidification can be seen between the dark primary Al dendritic phases in the magnified insert in Fig. 4.6b. Finally, the remaining L″ solidifies to form predominantly pure Sn particles (white in the SEM images) via the eutectic reaction, $E: L'' = (Sn) + (Al) + \theta\text{-}Al_2Cu$. This reaction was detected at 228.3 °C, while the thermodynamic calculations suggest that it should occur at 227 °C. In the Al-45Sn-10Cu alloy, the Calphad prediction is in good agreement with experimental data.

According to the Calphad calculation the Al-20Sn-10Cu sample should begin to solidify at around 598 °C. The sequence of phase separation/ formation of the Al-20Sn-10Cu alloy according to Calphad calculations are given below:

Phase formation temperature	Phase formation	Eq.
above 598 °C	L,	6.2a
between 598 to 550 °C	$L \rightarrow (Al) + L'$,	6.2b
between 550 to 524 °C	$L \rightarrow L' + (Al) + L''$,	6.2c
at 524 °C (monotectic reaction)	$L' = L'' + (Al) + \theta - Al_2Cu$,	6.2d
between 524 to 227 °C	$L'' \rightarrow (Al) + \theta - Al_2Cu$,	6.2e
at 227 °C (eutectic reaction)	$L'' \rightarrow (Sn) + (Al) + \theta - Al_2Cu$	6.2f

According to the Calphad calculation the Al-20Sn-10Cu sample should begin to solidify at around 598 °C. The DSC experiment shows a small amount of undercooling, where the first (most right-hand) peak at 592 °C represents the beginning of Al precipitation. These primary grains/dendrites grow to a phase fraction of around 0.5 before the first demixing of the remaining melt occurs at 550 °C (Eq. 6.2b). In this case the composition of L'' differs substantially from the parent liquid phase, and a small enthalpy effect can be detected in the DSC experiment. L'' droplets form throughout the sample, and while similar factors as described above (gravity and temperature gradient) also apply here, the motion of these droplets is inhibited by the solid particles and increased viscosity of the alloy. As a result, coagulation of the L'' droplets does occur as shown in Figs. 6.2a and b, but not to the same extent as in the Al-45Sn-10Cu sample (as seen in Fig. 6.1). Upon further cooling below 550 °C, the remaining liquid in the Al-20Sn-10Cu sample follows similar stages of solidification as described above for the Al-45Sn-10Cu sample. First, Al and a small amount of L'' is precipitated in the L' regions, before this region solidifies almost completely in the monotectic reaction. Finally, the L''regions solidify, forming mainly pure Sn particles in the eutectic reaction at 227 °C. Both these reactions have been clearly identified on the DSC curve in Fig. 4.3.

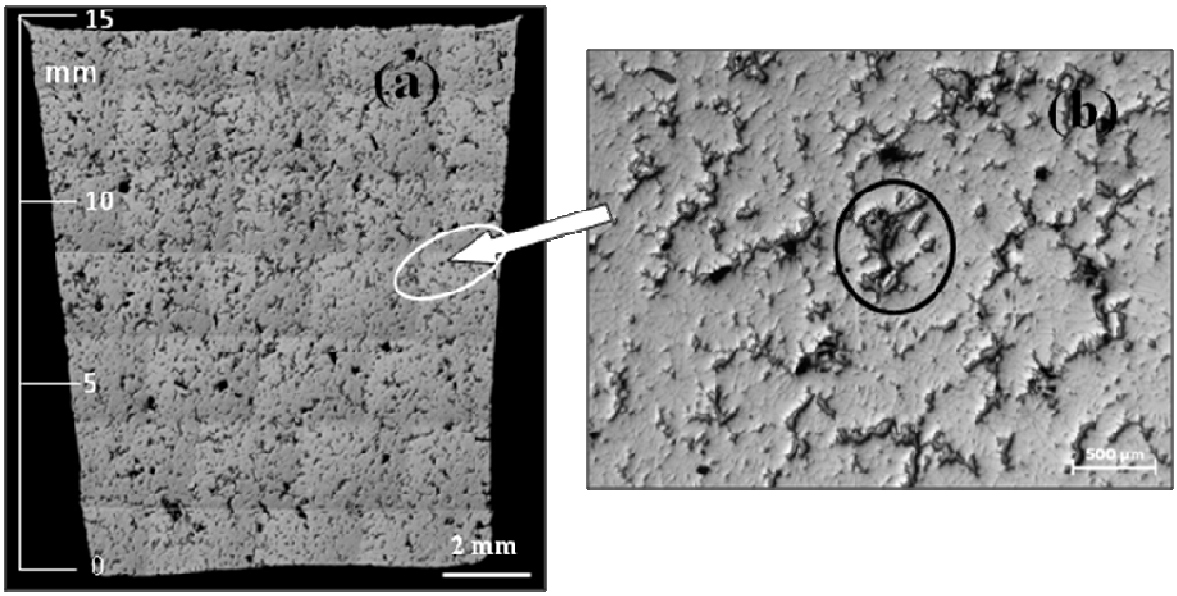

Fig. 6.2. (a) OM image of phase separation in the Al-20Sn-10Cu alloy of L′ (white in contrast) and L″ (dark grey in contrast) liquid in the conventional solidification process (cast into a steel mould directly from 650 °C); and (b) High magnification OM micrograph showing the Sn-rich phase trapped between the primary (Al) dendrites.

6.2.2 Microstructure of HPDC and MC-HPDC samples

In order to assess the effect of intensive melt shearing on the dispersion of the soft Sn-rich phase in the hard Al-rich matrix, both Al-45Sn-10Cu and Al-20Sn-10Cu alloys were processed by both HPDC and MC-HPDC processes. The microstructures obtained of the two alloys processed under different conditions are presented in Fig. 4.8. The most significant difference between the microstructures of the HPDC and MC-HPDC samples (Fig. 4.8) is that a very much finer microstructure is achieved with the MC-HPDC process. The distribution of the soft Sn particles (dark grey in the OM images) is also much more uniform, particularly for the Al-45Sn-10Cu alloy sample. This indicates that intensive shearing affects the microstructure of immiscible alloy castings through droplet interaction, including rupturing, coalescence and suspension (Tang and Wrobel 2005b).

The mechanism of the microstructural evolution and particle distribution for the Al-45Sn-10Cu alloy can be summarized as follows: In the MC-HPDC process, when the

alloy is fed into the MCAST machine (above the T_c) the melt is cooled quickly to the barrel temperature set by the control system, which is usually just below the monotectic temperature (T_m). Under the intensive shearing and powerful dispersive mixing action created by the twin screws, the liquid droplets attain a fine size. This is a result of the dynamic equilibrium between two opposite processes, coagulation and break-up of liquid droplets. Inside the MCAST machine, the slurry flow direction is opposite to the direction of the screw rotation, which means that the shear stress direction is opposite to the direction of the fluid velocity, and the turbulence leads to the formation of droplets with a round shape as well as accelerating the rupturing. The stages of the process from the homogeneous liquid to fine and uniformly distributed Sn particles in an Al matrix are shown schematically in Fig. 6.3. The fluid moves in the periphery of the screws in a 'figure of 8' motion moving from one pitch to the next. In the continuous flow field, the fluid undergoes a cyclic stress and re-orienting processes. The initial and boundary conditions are simplified and categorized as shown in Fig. 6.4. These include one-sided and two-sided shear; rapid profile, linear profile and nil profile of initial shear rate.

However, the final size of the liquid droplets will be dictated by the intensity of the shear mixing action and the thermo-physical properties of the system, such as viscosity, interfacial tension, etc. It is well known that the viscosity of the melt increases exponentially with the volume fraction of the solid phase and decreases dramatically with an increase in the shear rate and shear time (Fan 2002). Through careful selection of the processing temperature from thermodynamic calculations (Fig. 4.2), the viscous force was kept high enough to counterbalance the gravity force. Also, it has been experimentally confirmed that it is easier to break up liquid droplets when the viscosity ratio falls within $0.3 < \lambda < 1.5$ (where, λ is the viscosity ratio between the two liquids) (Fan *et al.* 2001). The phenomenon of drop formation in non-linear rheology is shown schematically in Fig. 6.5. Consequently, the alloy system is stabilized before the final solidification of the remaining liquid takes place. Therefore, a higher viscosity helps to inhibit agglomeration by slowing down the sedimentation of the Sn droplets.

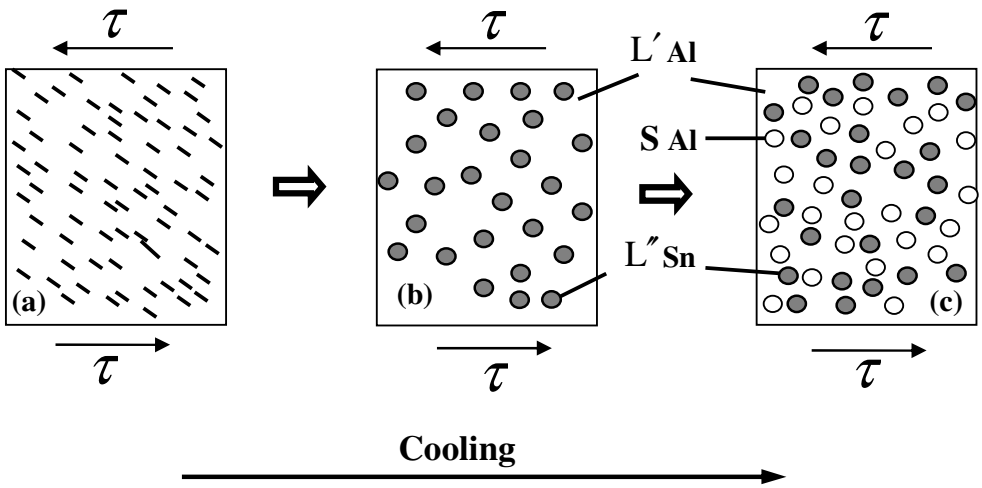

Fig. 6.3. Schematic illustration of the rheomixing process to achieve a uniform distribution of the soft phase in an (Al) alloy matrix (a) homogeneous liquid (above the T_c); (b) creation of the L″ droplets in the L′ matrix; and (c) rheomixing: formation of a primary (Al) solid phase (S) in the L′ matrix through a monotectic reaction.

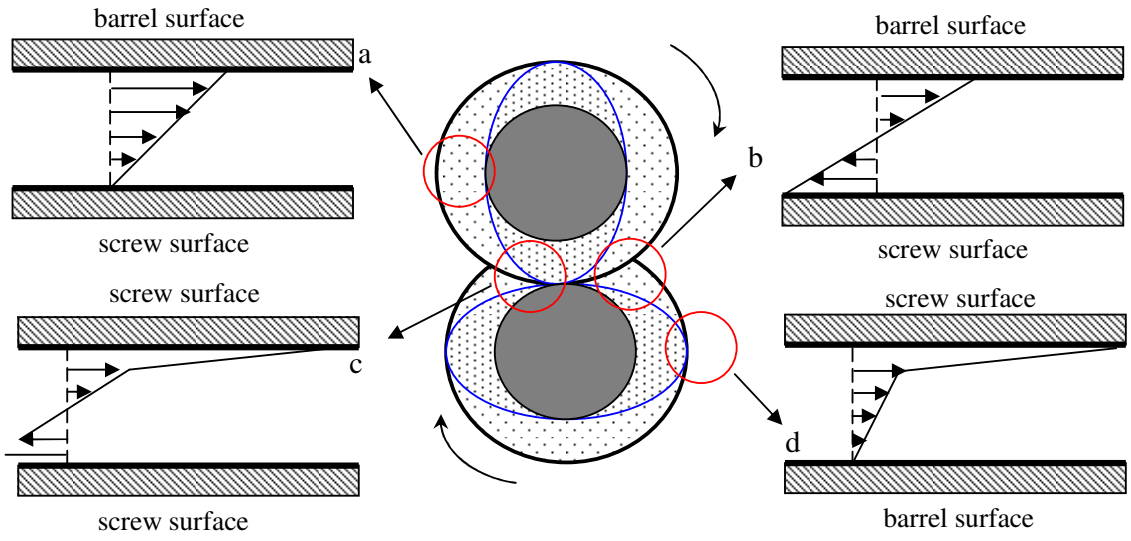

Fig. 6.4 Schematics of simplified flow configuration for the initial and boundary conditions in the different areas of the twin-screw machine. Schematics (a) and (b) show a linear profile of the shear rate. Schematics (c) and (d) show a rapid profile of the shear rate. Middle figure shows the viscosity vector field (Avalosse *et al.* 2000).

The effect of the viscosity of the semisolid slurry on the Stokes (U_s) (Levich 1962) and Marangoni motions (U_m) (Young *et al.* 1959) are explained in chapter 2, given by Eqs. 2.8 and 2.4. During intensive shearing, the melt temperature is extremely uniform throughout the entire volume of the liquid mixture. According to Eq. 2.4, U_m = 0, therefore, segregation of L″ droplets due to Marangoni motions is negligible during solidification of the intensively sheared melt. The high viscosity and small size of the Sn droplets also slow down the gravitational segregation according to the Eq. 2.4.

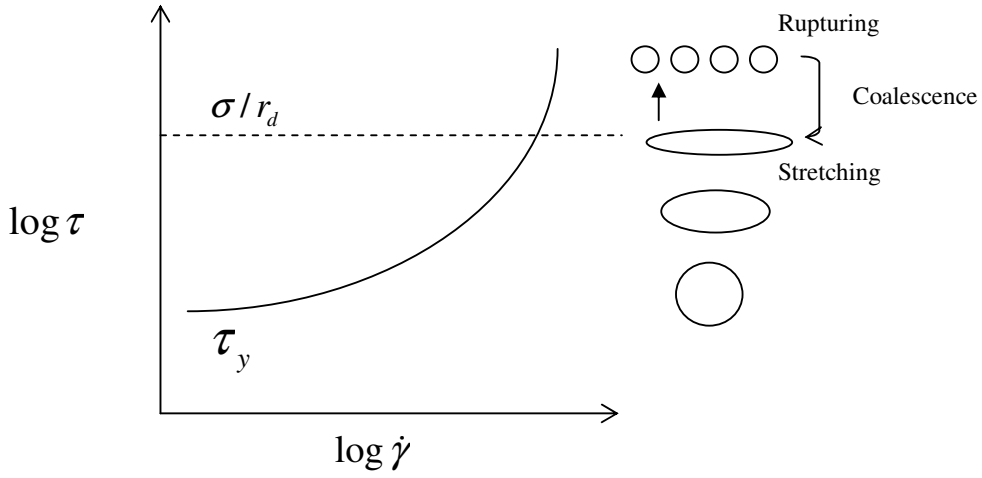

Fig. 6.5. Schematic sequence of results by shear rate (Mason 1999).

In the Al-45Sn-10Cu alloy, the Sn particle size has significantly decreased from 1 mm to 55 μm by shearing at 200 rpm (Fig. 4.9a). This is a significant reduction in the Sn particle size, compared with the conventional HPDC process. By further increasing the shear speed from 200 rpm to 800 rpm the Sn particle size has been reduced from 55 μm to 22 μm, as shown in Fig. 4.9a. For the Al-20Sn-10Cu alloy sample the Sn particle size was measured to be 13 μm (Fig. 4.9b) as produced by the conventional HPDC process. This Sn particle size is very small compared to the conventional HPDC Al-45Sn-10Cu alloy samples. The reason for this is that primary Al particles precipitate occurs first before demixing of the liquid as mentioned before, and also the Sn concentration was lower compared to the Al-45Sn-10Cu alloy. However, by applying shearing to the Al-20Sn-10Cu alloy the Sn particles size was reduced from 13 μm to 3 μm at 800 rpm for 60 s. Both the Sn and primary Al particle morphology is quite close to spherical. Fig. 4.9 clearly shows that the size of the Sn particles was significantly decreased and the shape factor increased with an increase in the shearing speed.

Figs. 4.8a and c illustrate that Sn particles are severely segregated in the conventional HPDC process for both alloys. In contrast, Figs. 4.8b and d show that, a homogeneous microstructure of the soft phase in the Al matrix was achieved after intensive shearing in the semisolid region. It was also observed that intensive shearing helps to increase the number of the Sn particles as a result of the reduced particle size shown in Fig. 4.8. It was observed that a decrease in Sn particle size with shearing is related not only to the break-up process but also due to the shear-induced coalescence. The coalescence can be accelerated by the same factors that favour the drop break-up, i.e. high shear rate and reduced viscosity ratio. Therefore, the minimum droplet size under given shear mixing conditions is a dynamic balance between two opposite processes, droplet break-up and coalescence.

Quantitative analyses of the distribution were made by the Quadrat method (Karnezis *et al.* 1998). Fig. 6.6 shows the frequency of scatter according to the number of particulates per Quadrat, *Nq*, together with the theoretical (Karnezis *et al.* 1998, Rogers 1974) statistical distribution curves (solid line). Fig. 6.6 reveals that the soft phase distribution in the Al matrix is close to the Poisson and the binomial distributions from the MC-HPDC process, while the HPDC process results in a segregated distribution expressed by a negative binomial curve. It can be seen from these quantitative results and microstructures that the intensive shearing process offers a better distribution of the soft phase throughout the whole volume of the sample compared to conventional methods (Karnezis *et al.* 1998, Rogers 1974).

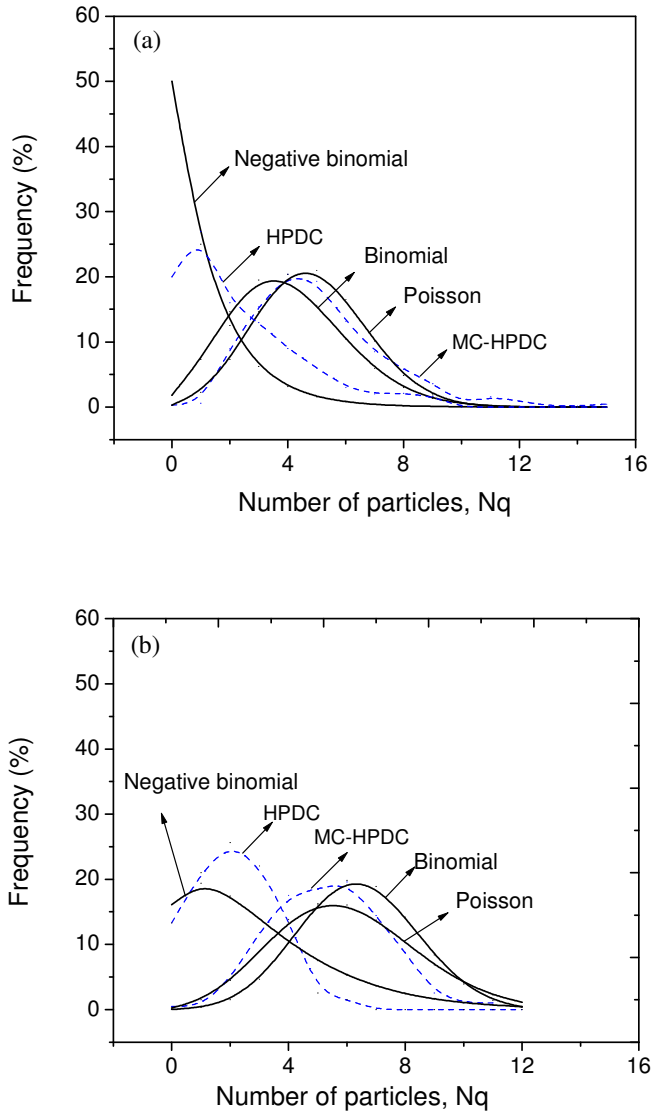

Fig. 6.6. Sn particle size distribution for HPDC and MC-HPDC samples in comparison with other theoretical distribution curves for (a) the Al-45Sn-10Cu alloy and (b) the Al-20Sn-10Cu alloy.

6.3 Al-Si alloys

Microstructural refinement during solidification is important for cast metallic alloys to improve their mechanical performance as finished castings or subsequent thermo-mechanical processing behaviour as semi-finished products such as billet and slab materials. Chemical refinement is a standard practice for many commercial alloys. However, many alloy systems do not have an established chemical refiner and alternative approaches to microstructural refinement need to be established. In chapter 5, it has been shown that intensive shearing of the liquid metal leads to significant microstructural improvement. The objective of the following section is to explain specific issues related to microstructural and morphological changes, and suggest possible mechanisms for such modifications.

6.3.1 Microstructural evolution under shearing

The experimental findings in this study clearly demonstrated that a substantial grain refinement with a uniform microstructure for Al-Si alloys can be achieved by the MCAST unit. Microstructural refinement is achieved by intensive melt shearing provided by the MCAST process without any involvement of a deliberate chemical addition. This physical grain refining process by fluid flow is in contrast to the chemical grain refining achieved by addition of grain refiners such as Al-Ti-B master alloy.

6.3.1.1 Nucleation of α-Al in hypoeutectic alloys

The ideal condition for nucleation has been referred to as physical grain refinement in the present investigation. Consequently, physical grain refinement increases the effective nucleation by tailoring the solidification conditions without necessitating the addition of inoculants. There has been significant controversy in explaining grain refinement without grain refiner additions. The extensive literature suggests that in the absence of a grain refiner (where constitutional undercooling produced nucleation is important), big bang (also known as free chill crystals or wall mechanism) and dendritic detachments is the primary contribution to the creation of equiaxed grains (Chalmers 1964, Das *et al.* 2006, Hutt and StJohn 1998, Kurz and Fisher 1998).

The MCAST unit consists of a pair of twin screws, which is capable of delivering very high intensity shear and a high level of turbulence. In addition, inside the MCAST unit the entire melt is broken up into packets of liquid that are in intimate contact with the screw surfaces and barrel resulting in very efficient heat transfer. Experimental evidence shows casting near the liquidus temperature promotes a fine equiaxed microstructure. The formation of fine and equiaxed grains close to the liquidus temperature has been explained in the literature (Wang *et al.* 2000a, Wang *et al.* 2000b, Xia and Tausig 1998). Recently, it has been shown that intensive shearing is also capable of producing a fine grain size above the liquidus temperature.

Based on the experimental evidence, Fan *et al.* 2009a proposed a multi-step heterogeneous nucleation mechanism, as shown schematically in Fig. 6.7. In this mechanism, oxide particles play an important role to nucleate the α-Al phase. However, it is well known that the wetability of oxide is low by a liquid melt (Campbell 2003, Campbell 2006) and this is an essential condition for an oxide particle to act as a potent nucleation site. Several experiments have shown that under intense shearing conditions, wettability of oxide by liquid metal is improved and oxide particles can be dispersed by overcoming the energy barrier for wetting (Fan *et al.* 2009b).

It is believed that in these alloys during the continuous cooling of the sheared melt, the intermetallic phase nucleates on the oxide particles. With further cooling to temperatures below the alloy liquidus, the primary phase (e.g., α-Al) will then nucleate on the intermetallic particles. The primary α-Al phase may also nucleate directly on the oxide particles if there is no intermetallic phases present. Therefore, it is very important to disperse these nucleation sites in the whole volume of liquid melt. According to the free growth theory developed by Greer *et al.* (2000) the undercooling ΔT_{fg} required for achieving the state of free growth is given by:

$$\Delta T_{fg} = \frac{4\sigma_k}{\Delta S_v d} \tag{6.3}$$

where d is diameter of the potent inoculant particles and ΔS_v is the volumetric entropy of fusion. The free growth undercooling is inversely proportional to the particle size, showing that the larger particles are more potent for heterogeneous nucleation and become active first and, under typical solidification conditions, only a small fraction of

the particles become active before recalescence occurs. According to this theoretical model, more particles would contribute to heterogeneous nucleation if a narrow size distribution is achieved, and therefore the efficiency for the inoculation is promoted. Although oxides are always present in alloy melts, this type of dramatic grain refinement had never been observed previously, due to the lack of sufficient active particles.

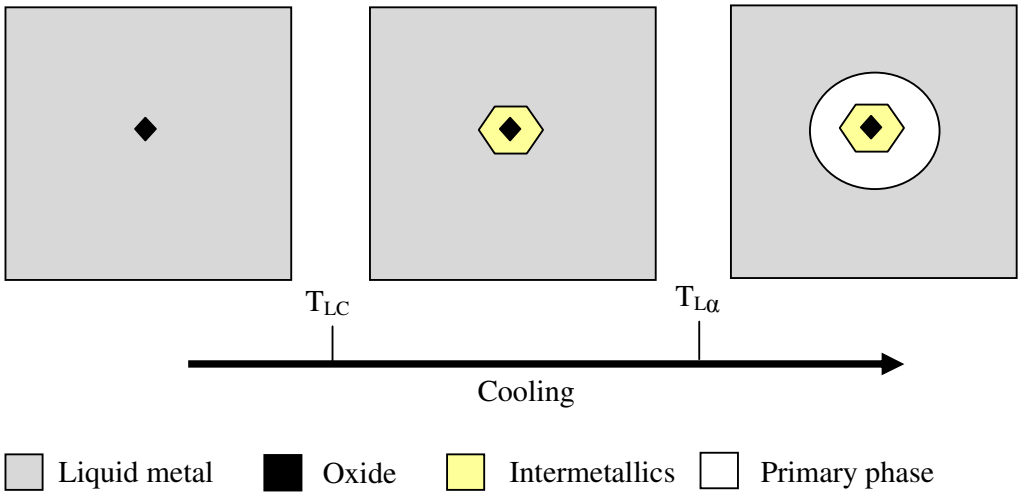

Fig. 6.7 Schematic diagram showing the multi-step nucleation mechanism. T_{LC} and $T_{L\alpha}$ denote the liquidus of intermetallic phases and the primary solid solution phase, respectively.

6.3.1.2 Nucleation of primary Si in hypereutectic Al-Si alloy

Optical microscopy conducted on the conventional Al-14Si samples revealed the presence of star like, platelet and polygonal shape primary Si particles (Fig. 6.8a) which congregate resulting in a non-uniform distribution in the matrix. It is known that the microstructure in the solid state is influenced by the liquid structure before solidification (Wang *et al.* 2000c). For liquid hypereutectic Al-Si alloys, Si is present essentially as Si clusters (Fig. 6.8b) (Singh and Kumar 1973). Some researchers suggest that Si-Si clusters of a large size should be conducive for the formation of the nuclei of star-like or other irregular primary Si (Xu *et al.* 2006). It is reported that the nucleation of irregular morphology primary Si are generated by the formation of linked clusters due to successive branching of critical size polyhedral groups of Si atoms in the liquid melt

(Liang *et al.* 1995). In a conventional casting process, the majority of nuclei are transferred to the overheated liquid region due to convection caused by die filling, resulting in a non-uniform distribution of primary Si particles.

On the other hand, the MC-HPDC Al-14Si samples show an improvement in morphology and distribution of primary Si phase (Fig. 5.24). The fluid flow inside the MCAST unit is characterised by a cyclic variation with a high shear rate and high intensity of turbulence. These characteristics make the twin-screw mechanism very powerful for dispersive mixing. The temperature and composition field inside the MCAST unit are extremely uniform throughout the alloy melt. The intensive mixing action and melt conditioning are likely to disperse the small sized Si clusters, giving rise to an increased number of potential nucleation sites. Under such conditions, it is expected that throughout the entire volume of the liquid, nucleation would occur and each nucleus would survive and contribute to the final solidified microstructure. The uniform temperature and composition field due to an intensive shearing and the intense turbulent flow are effective for microstructural refinement leading to an energetically stable spherical growth of the primary Si phase.

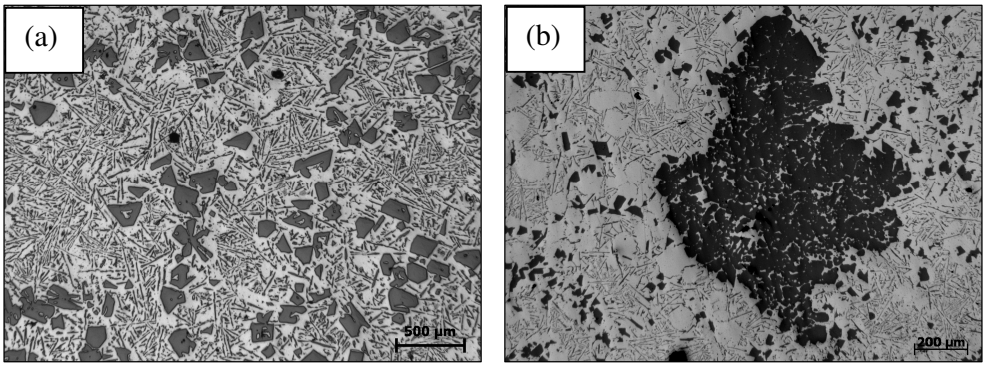

Fig. 6.8. Al-14Si alloy conventionally cast in a graphite crucible from the liquidus temperature (a) different types of Si flake and (b) Si particle cluster.

6.3.1.3 Eutectic Si

It is well established that the Al–Si eutectic typically consists of flakes or plates. At relatively fast cooling rates, such as in HPDC, the Al-Si eutectic phase is much finer compared with that from normal casting techniques. Al-Si alloys display four different

types of eutectic morphology (Elliott 1984) depending on the cooling rate and composition, which are massive silicon particles, rod or angular silicon, flake silicon, and fibrous silicon. The growth characteristic of Al-Si eutectic suggested by Kobayashi and Hogan (1985) consider that nucleation of flat plate Si occurs when two groups, each made up of a few Si atoms arranged in a tetrahedron, combine together to form an embryo. Once formed, the embryo develops into a critical size nucleus by the attachment of single Si atoms to its surfaces. In this arrangement, the central mirror plane between the two tetrahedrons becomes a {1 1 1} twin plane. More tetraheda can add to the growing nucleus, which minimizes its surface energy by forming {1 1 1} planes at its corners. The presence of two or more {1 1 1} twin planes triggers growth of the Si phase via the twin plane re-entrant edge mechanism (Hamilton and Seidensticker 1960), resulting in a plate-like morphology. The growth direction of Si can be changed depending on the solidification conditions by displacement twinning (Shamsuzzoha and Hogan 1985).

Unlike the primary Al or Si phase, there is a scarcity of available results on the effect of intense shearing on the morphology of the eutectic Si phase. An increase in the eutectic spacing under intensive shearing has also been explained on the basis of a reduction in Si enrichment ahead of the Al phase from enhanced convection, thereby eliminating negative curvature and nucleation of new Si phase at the eutectic interface (Feng *et al.* 2008). However, as in the case of an externally applied force application, there have been conflicting reports. Coarsening of eutectic Si has also been reported in a mechanically stirred melt undergoing relatively fast solidification in a metallic mould (Apaydin 1982) where the Si particles may not travel enough through the bulk liquid. On the other hand, refinement of eutectic Si and intermetallic phases has been reported under electromagnetic stirring although the origin of refinement has not been explained (Nafisi *et al.* 2006). This clearly demonstrates the difficulties associated with interpreting Al-Si eutectic growth since cooling rate variations can significantly influence the Si morphology and complicate the observed experimental results. Despite the volume of research conducted on the Al-Si eutectic, a comprehensive understanding of the mechanisms of microstructural formation is still lacking (Makhlouf and Guthy 2002). The relative domination of nucleation or growth may make an important contribution to the evolving eutectic morphology (Dahle *et al.* 2005, McDonald *et al.* 2004).

In the present study, we observed that the uniformity of the eutectic silicon phase has been modified by varying T_p. In the hypoeutectic system, the micrographs of various cast samples produced at higher T_p suggest that overall microstructural refinement in the entire bulk sample occurs through an increased area fraction of α_2-Al which are much smaller than ESCs (or α_1-Al) and this provides a better uniform microstructure when compared to samples produced at lower T_p. The presence of a higher area fraction of α_2-Al at higher T_p (Fig. 5.7) can improve the chance for a uniform distribution of the eutectic phase during the solidification process in HPDC. It could be possible that the fine Si platelets are formed in the last eutectic to freeze between the existing solid α-Al. These individual intergranular liquid pockets have a very small volume but a large contact area with the solid grain resulting in a high cooling rate refining the eutectic morphology. The size, shape and distribution of the brittle eutectic Si phase in final microstructure play very important roles into the mechanical properties of alloys (Elliott 1984, Makhlouf and Guthy 2002). The coarse, large size eutectic silicon flakes give low strength and poor ductility (Dahle *et al.* 2001).

Observed eutectic Si morphology is a fine and fibrous structure (average eutectic flake size 2.1 μm) due to an elevated undercooling under the high cooling on HPDC process (~10^3 Ks^{-1}). On the other hand, at slow cooling eutectic Si forms long flake (average eutectic flake size 9 μm) like structure, typically of TP-1 (~ 3.5 Ks^{-1}). From previous researcher (Grosselle *et al.* 2009) note that eutectic Si flake size decreased from 3.13 μm to 2.43 μm in caste samples increase strength from 225 MPa to 280 MPa.

6.3.1.4 Intermetallics

The optical microstructure characterisation shows that intensive shearing has an effect on the primary α-Al grain size, as described in the previous section. The result from the intermetallic study under intensive shearing shows a similar effect on the morphology of cubic α-Al(Fe,Mn)Si particles, which is indirect conformation with the oxide nucleation theory proposed by Fan *et al.* (2009b). Intensive shearing also shows considerable effects in reducing the tendency for the formation of faceted features (note that faceting is common for intermetallic compounds). The dendritic morphologies of the α-Al(Fe,Mn)Si compound can be modified into an equiaxed morphology (Fig. 5.13). Previous work (Fang *et al.* 2007) at BCAST demonstrates that with the monoclinic β-AlFeSi phase, melt

shearing was seen to reduce the usual long needle morphology into discs or short bars with a substantial reduction of the aspect ratio. The effects of melt shearing on the cubic α-Al(Fe,Mn)Si can be interpreted in a similar way to the solid solution phase, as the star-like or cross-like features can be considered as a special case of dendritic growth. On the other hand, the effects of melt shearing on the morphological modification of the monoclinic β-AlFeSi are interesting, since the formation of a needle-shaped morphology is largely due to significantly different solid–liquid interfacial energies and associated disparity in growth rates along different crystallographic directions. The modification of aspect ratios for the β-AlFeSi phase suggests that melt shearing could reduce the differences in solid-liquid interface, in turn, slow down the preferential growth in the direction of the longitudinal needle axis. This could occur due to the reduction in the diffusion layer thickness at the solid-liquid interface, and the associated disturbance of local equilibrium ahead of the growing solid front. This is expected to lower the compositional difference at the solid-liquid interface, thus reducing the growth anisotropy and resulting in a reduced aspect ratio (Fang *et al.* 2007).

In microstructures of the hypoeutectic Al-Si alloys, the intermetallic particles have agglomerated forming clusters preferentially located at the grain boundaries or the interdendritic regions (Fig. 5.13a). This can be explained by particle pushing theories (Stefanescu 1988a, Stefanescu *et al.* 1990, Youssef *et al.* 2005), which predict the existence of a critical velocity of the solidification front below which the particles are pushed ahead of the advancing solidification front. Cohesive forces hold the agglomerates together, hydrodynamic stresses developed due to the specially-designed profile of the screws, break the agglomerates into individual particles which results in a homogeneous dispersion (Fig. 5.13b). It could be possible that the fine α-Al(Fe,Mn)Si particles are formed in the matrix due to the uniform chemical composition, temperature and nucleation sites throughout liquid.

6.3.2 Defect band formation

From previous research Dahle and StJohn (1999) showed that in the HPDC process, feeding and deformation directly leads to several types of defects. The defects formed include porosity, hot tearing and chemical segregation. It will be shown that the presence of these defects in many cases can be attributed to the fracture (shearing and/or collapse)

of the dendritic network during the filling and solidification process. The conventional HPDC cross section Fig. 5.9b shows a highly inhomogeneous microstrucutre. The central region of the casting is always seen with a large amount of ESC particle segregation or interlocked dendrites (Fig. 5.9c), which contain a significant liquid fraction. The remaining liquid exists between the dendritic envelopes in this case, the region would have taken longer to solidify than the surroundings and be difficult to feed. It is difficult to feed because, little liquid is available from adjacent regions to feed the shrinkage, and porosity forms (Fig. 5.14). Porosity in the centre is found when there is little during solidification and is a straight forward result of insufficient feeding to the last region of the casting to solidify. The defect band ring segregation at high magnification is shown in Fig. 5.9c. The layer of segregation can be explained by shearing and flow between a layer solidified at the wall and a region of a high solid fraction in the centre due to flow. The solid is concentrated in the centre of the flow, either as a result of solidification during flow, but more likely because of premature solidification in the shot sleeve (Gourlay *et al.* 2004).

6.3.2.1 Mechanism for band formation

In a conventional HPDC cast specimen (Fig. 5.9), the higher solid fraction of ESC particles are concentrated in the centre of the die cast samples. As we move from the centre towards the mould wall the solid fraction ESC particles are decreased (Fig. 5.12). A schematic diagram of the distribution of solids in an HPDC tensile specimen is shown in Fig. 6.9. As is known when the solid fraction of particles has increased above the coherency point, the shear strength will increase as a function of f_s (solid fraction). Once the ESC dendrite network forms and hence starts to partly interlock with growth it requires a higher energy to deform and shearing occurs with a high resistance. This leads to a defect band between the concentrated ESC particle region and the skin. In particular in the conventional HPDC process, the ESC particle solid fraction is mainly governed by the temperature of the melt in the shot sleeve and is influenced by several parameters, such as the liquid metal superheat, the heat transfer coefficient, and surface properties of the shot sleeve and alloy composition (Dahle and StJohn 1999, Gourlay *et al.* 2004).

In contrast, the sheared melt will have a uniformity of temperature, composition and a well-dispersed nucleation site which allows the formation of considerably less solid

fraction of ESC particles (Fig. 5.7) and these are well distributed throughout the volume of the MC-HPDC cast specimen. At low solid fractions, the strength increases at a relatively low rate. When the solid fraction along the shear plane is reduced to below f_s^{peak}, shearing can occur with less resistance. This shear strength is further reduced when the ESC particle morphology is spherical in shape which allows considerable liquid flow between the particles, which helps in the final solidification to reduce the area fraction of porosity in a cast specimen (Fig. 5.15).

The experimental results give witness to this mechanism with respect to the variation of the pouring temperature. Fig. 5.10 shows the generated defect band position from the die wall and thickness with respect to the processing temperature of HPDC and MC-HPDC specimens. The results clearly show a higher fraction of ESC particles in the conventional HPDC specimen generate a defect band closer to the die wall. From the experimental results it is also noticeable that by applying intense shearing to a Al-Si hypoeutectic liquid resulted in a reduced defect band size and uniform distribution ESC particles which allow the band position to be closer towards the centre, which has a direct relation with the mechanical properties of the cast samples, a detailed explanation will be given in section 6.3.4.

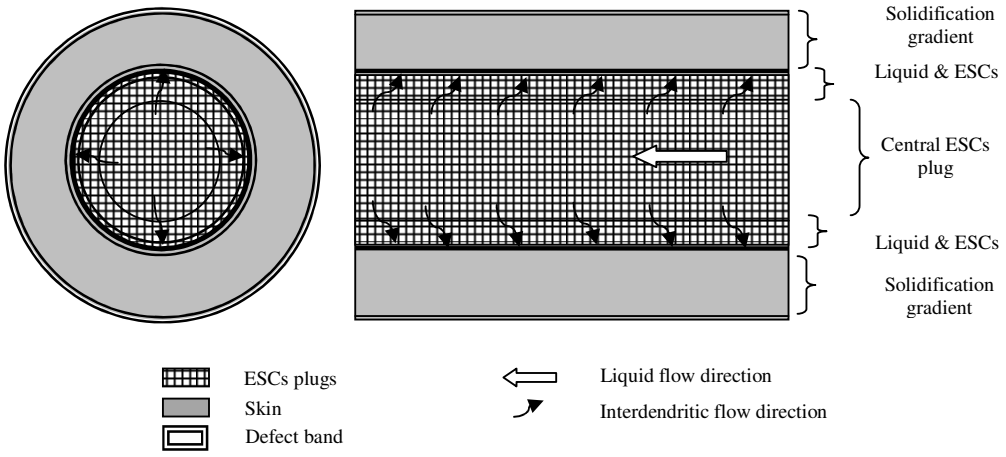

Fig. 6.9 A schematic diagram of the distribution of solid at a late state during flow (Figure redrawn from Gourlay *et al.* 2004).

6.3.3 Porosity

From a current understanding, it is believed that porosity in Al alloys is due to both solidification shrinkage and gas porosity. Hydrogen is the only gas which dissolves readily to a significant level in liquid Al. Hydrogen contents of ~0.65 and 0.034 ml/100 g in the liquid and solid phase have been reported for pure Al (Stefanescu *et al.* 1988b). This suggests that there is a lower solubility in the solid than in liquid aluminium and hence as solidification proceeds, the excess hydrogen from the newly-formed solid phase will be rejected and hence accumulated at the solidifying interface giving rise to the formation of gas bubbles and then gas pores.

Most metals shrink during the phase transformation from the liquid to solid and this is the main reason for the formation of macro and micro shrinkage porosity in castings. Macro shrinkage or volumetric shrinkage is typically of the order of 6 % for pure Al alloys (Brown 1999) and it varies with the addition of alloying elements. The macro volumetric shrinkage can be compensated for by dimensional allowances; however, production of micro shrinkage porosity free cast components is known to be a challenge. During solidification, the liquid volume reduces and the surrounding liquid will flow in to compensate. According to Campbell (1997) there are five different feeding mechanisms which can take place to compensate the volumetric shrinkage during different stages of solidification and micro shrinkage porosity formation is high during the interdendritic and solid feeding stages (last stages of solidification) so that generally micro shrinkage porosity is found in the interstices of dendrites and at the areas which solidify last.

The high area fraction of porosity measured at a higher pouring temperature (Table. 5.2), in the present Tatur test experiments can be attributed to the higher solubility of hydrogen and high level of shrinkage porosity. In addition, the current investigation shows the application of high intensity shearing to the liquid Al melt prior to solidification reduces the formation of micro porosity under the same casting conditions for Al-Si alloys studied. It is necessary to mention here that the liquid melt will be exposed to air for a longer time during the MCAST process compared to the conventional process. It is expected that liquid Al melts should absorb a certain amount of hydrogen gas and might have formed gas bubbles. An optical view of the porosity formed exhibits the presence of larger size pores in the conventional sample than in the MCAST sample. This finding

suggests that gas bubbles that have already formed in the liquid melt may have collapsed and/or been dispersed to a smaller size by the application of high intensity shearing which hence resulted in the formation of smaller and less micro porosity.

As suggested by Campbell (1997), and other authors Gupta *et al.* (1992) an oxide film can be a potential site for the formation of gas and shrinkage porosity in a conventionally cast sample, however, no systematic work has been done in the current study. Generally, oxide films are present in as cast Al alloys as bifilms, and are sites for easy gas entrapment between the contacting dry side oxide films. Previous studies Fan *et al.* (2009a), and the present investigation found that when the intensive shearing was applied to the melt, the oxide film will be broken up into individual particles and dispersed uniformly in the liquid melt. Furthermore it is also understood that intensive shearing can force the liquid metal to wet the oxide particles by "forced convection" (Fan *et al.* 2009a and 2009b). The presence of wetted individual oxide particles in the MCAST sample can no longer be potential sites for porosity formation and may lead to diminish the level of porosity.

6.3.4 Mechanical properties

The tensile specimens produced under intensive shearing (MC-HPDC) show better properties compared with the conventional HPDC tensile specimens Fig. 6.10. These results are very well supported by the microstructural observations such as considerably reduced porosity, improved skin thickness, band thickness and refinement and a good distribution of the eutectic phase, primary α-Al and intermetallic particle size. As a result of these features MC-HPDC samples of hypoeutectic Al-Si alloys exhibited a good combination of UTS and elongation, compared to the typical tensile properties of sample produced by the conventional HPDC process.

As described previously cast hypoeutectic Al–Si alloys have a dual phase microstructure, composed of a primary α- Al phase and an interdendritic eutectic Al-Si structure. The primary phase is an Al-based solid solution in hypoeutectic alloys and the primary phase is a Si-based solid solution in hypereutectic alloys. A large volume of research has been conducted to evaluate the primary α–Al, Si, eutectic Si and intermetallic particle size, shape and distribution and their deteriorating effects on the deformation behaviour and

fracture properties of Al–Si alloys (Fat-Halla 1987, Gall *et al.* 2000, Lee *et al.* 1995, Qian *et al.* 2006). Al-Si alloys have a strong mismatch in the elastic and plastic properties between the primary α–Al and Si phases; the distribution of each phase is believed to affect the fracture behaviour. With conventional HPDC the solidification process and microstructure of tensile specimens varies significantly across the three regions such as the skin, defect band and segregated ESC particles (Fig. 5.9). These regions have different sizes, shapes and distributions of each phase (Figs. 4b, 5 and 6a). It is therefore quite probable that each phase and the regions play an important role in the mechanical properties of specimens. The fine and more uniform microstructure under an intensive shearing condition has a significant influence on the mechanical properties. It is important to note that, shearing not only causes a refined microstructure but also contributes to an increased skin thickness of the tensile specimen (Fig. 5.10) and this skin area mainly contained finer particles (Fig. 5.12).

In the HPDC process it is possible that there are two forms of oxide film defect in cast components, one which originated in the crucible and the second, which formed in the mould cavity. Oxide film defects are formed in the mould by surface turbulence which entrains the films which in the bulk liquid. Common mechanisms for this entrainment include returning waves, arising during filling of the runner bar, and plunging jets. It has been concluded that when developed, returning waves cannot attain the more stable and less entraining tranquil flow regime desirable in the running system of castings. Detailed explanations on the oxide film and liquid flow in the current study are difficult due to the difference in liquid melt (pouring) temperature and alloy compositions (Green and Campbell 1993).

The potency of each type of oxide defect is unknown in the current experimental conditions. All the tangled networks observed during this study are like those observed in Fig. 5.14. On no occasion was it possible to resolve an oxide film in section. It is known that the thickness of an oxide film formed on an aluminium melt held for approximately 60 min is in the order of tenths of microns (Thiele 1962). This should have been resolved with SEM examination. The thickness of an oxide film formed on an aluminium-magnesium alloy melt during the initial stages (10s) of liquid metal oxidation is known to be approximately 20 nm (Freti *et al.* 1982). Therefore the failure to observe an oxide film implies that all the tangled oxide networks observed were formed during conditions of

surface turbulence (metal velocity greater than 0.5 ms^{-1}). The source of the tangled oxide film networks in the castings may be the initial transient filling stage before the final solidification (Green and Campbell 1993). The Weibull statistic analysis in Figs. 5.24 and 5.25, clearly indicate that the defect density determines the tensile strength and elongation. In this current study Weibull probability curves are mainly affected by the porosity, oxide films, grain size, defect band which are the defects.

A comparative study, in this work illustrated the relationship between the yield strength (YS) and the skin area of the tensile specimens. The data points in Fig. 6.11 are the measured YS as a function of the cross sectional area occupied by the skin ($\pi(R^2-(L_2+L_3)^2)$ of the tensile specimen as shown in Fig. 5.9b. Experimental data is well described by a linear fit (solid line), which strongly suggests that the improved mechanical properties can be correlated well with the observed improvement in area occupied by small α_2-Al particles or skin. The experimental results obtained in this study are also well supported by a previous study where by removing the skin of a tensile specimen, a significant reduction in the yield strength was measured (Maugis 1985, Cook 2006). The mechanical properties of Al-Si alloy components may be further improved via refining the primary phase and the eutectic Si flake size.

For the hypereutectic alloy, the variation in ultimate tensile strength (UTS) and elongation with pouring temperature, under sheared conditions are similar to that of the hypoeutectic alloys. In the Al- 14%Si alloy, the solidification event controls the size, shape, and distribution of the more brittle Si phase in the final microstructure, which in turn is likely to influence both the ductility and strength of the alloy (Elliott 1984). It is well known that depending on the nature of the Si phase in hypereutectic Al-Si alloys, it can offer a range of mechanical properties to the alloys by improving fracture strength of cast components.

When the fracture strength, σ_f is exceeded by the internal stress of various different phase particles σ_p, the cracking of particles will occur. σ_f depends on various factors, such as the size, shape, distribution and volume fraction of the particles (Brechet *et al.* 1991). Particles with a larger size will fracture at a smaller σ_f. Fracture mechanics suggest that σ_f can be approximated by (Curry and Knott 1979, Lee *et al.* 1995):

$$\sigma_f = \sqrt{\pi E \gamma_s / D} \tag{6.4}$$

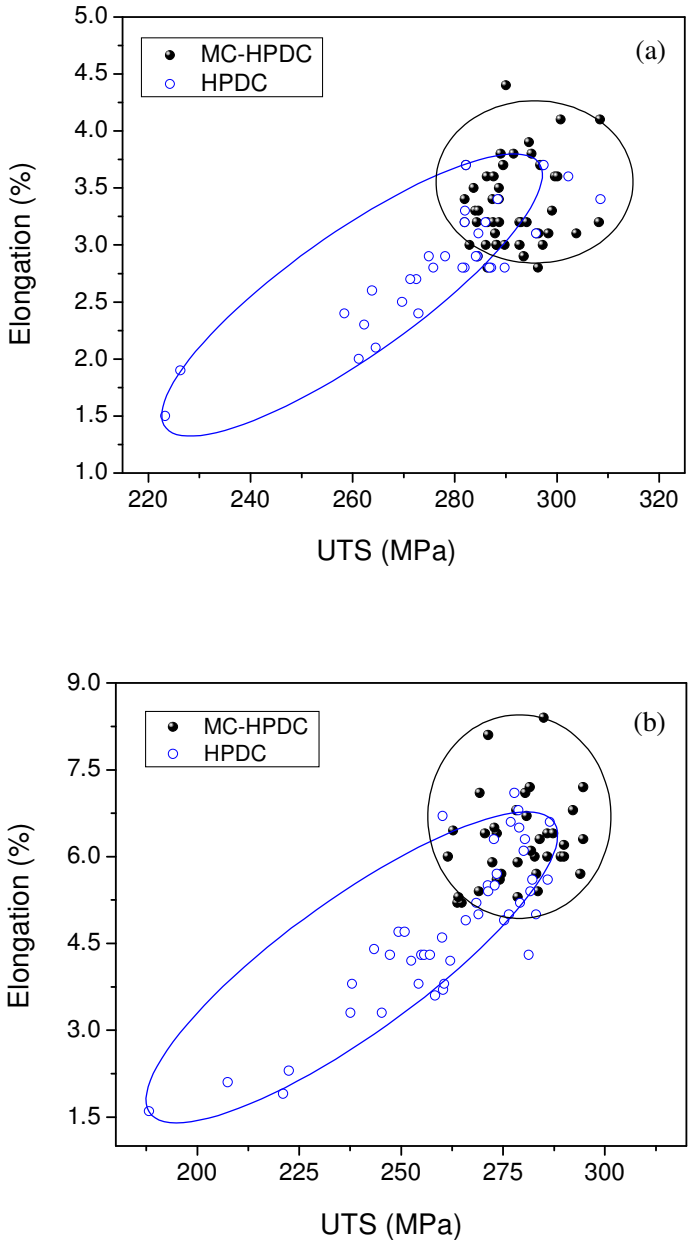

Fig. 6.10 Comparison of tensile properties of HPDC and MC-HPDC processed sample (a) Al-9.4Si and (b) Al-10.3Si alloys

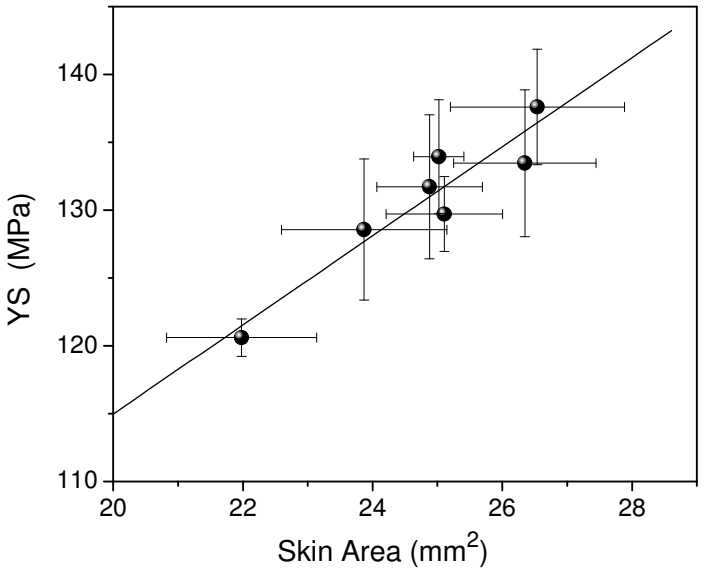

Fig. 6.11. Yield strength (YS) as a function of measured skin area for a specimen produced by the HPDC process. The solid line is a linear fit to the experimental data suggesting a direct correlation between microstructural improvement and mechanical properties.

where γ_s is the specific surface energy, D is the diameter of the particle and E is Young's modulus. For Al, γ_s is 1.77 J/m^2 (Dash and Makhlouf 2002) and, E is 70 GPa (Dash and Makhlouf 2002), and for Si γ_s is 1.0 J/m^2 (Cook 2006), and E is 161 GPa (Cook 2006). Eq. 6.4 suggests that a finer microstructure improves the mechanical properties such as fracture strength. Appendix V and Figs. 5.27a clearly indicates that average primary α–Al and Si particle size decreased under intensive shearing. By using Eq. 6.4 fracture strength σ_f calculated for Al-9.4%Si (LM24), Al-10.3%Si (Silafont) and Al-14%Si alloys in Appendix V. By comparison HPDC tensile samples with MC-HPDC tensile samples, a σ_f value of non-sheared samples is between 21-24 MPa m$^{1/2}$ for hypoeutectic alloys and between 13-17 MPa m$^{1/2}$ for hypereutectic alloy. While shows intensive sheared cast samples improved σ_f value about 20% (LM24), 17.8% (Silafont) and 16% (Al-14%Si) compared to the non-sheared samples.

6.4 Summary

- The Al–Sn–Cu system had an isolated ternary miscibility gap, generating three different monotectic invariant reaction types. It is also shown that these alloys offer a distinction between primary liquid demixing and primary crystallisation in the solidification path, with a corresponding impact on the solidification microstructure. A precise knowledge of the calculated phase equilibria is crucial to control this distinction by variation of the alloy composition. A calculated phase fraction chart was demonstrated to explain details of the microstructural formation in the monotectic four-phase reactions.

  Experimental results on high pressure die casting of the immiscible alloys with and without melt shearing have confirmed that intensive melt shearing can greatly assist the dispersion of the soft Sn phase without the occurrence of macro-demixing. Secondly, the effect of the solidification path on the dispersion of the soft Sn particles was investigated by gravity die-casting. It is found that with the immiscible alloys with the precipitation of the primary Al particles prior to the demixing reaction (such as for Al-20Sn-10Cu) it is much easier to obtain a fine and uniform dispersion compared with those alloys with a demixing reaction before the precipitation of the primary Al particles (such as for Al-45Sn-10Cu).

- Dramatic grain refinement of primary α-Al and Si grain size and/or particles over the entire cast specimen has been obtained in Al-Si alloys by employing intensive shearing combined with casting at the liquidus temperature. Intensive shearing at the liquidus temperature improved the distribution of the α-Al (Mn,Fe)Si intermetallic phase with a narrower size distribution and also significantly reduced the defect band size and porosity by improving sphericity and uniformity of the primary α-Al particles. The application of MC-HPDC process is a useful way in combating the detrimental effect of foreign particles on the mechanical properties.

Chapter 7
Conclusions

The overall goal of the thesis was to understand the influence of shearing on solidification process of different Al alloys such as Al-Sn-Cu immiscible alloys and hypereutectic and hypoeutetic Al-Si cast alloys. Melt conditioning by advanced shearing technology (MCAST) unit was used to implement intensive shearing of liquid metals. The conclusions drawn from this investigation are summarised as follows:

Rheomixing of Al-Sn-Cu immiscible alloys

- Using advanced computational thermodynamic techniques, two model immiscible alloys, Al-45Sn-10Cu and Al-20Sn-10Cu, were selected to investigate the feasibility of producing fine and uniformly distributed soft Sn particles in a relatively hard Al-Cu alloy matrix by way of a novel MCAST process.
  - Firstly, experimental results on high pressure die casting of the immiscible alloys with and without melt shearing have confirmed that intensive melt shearing can greatly assist the dispersion of the soft Sn phase without the occurrence of macro-demixing.
  - Secondly, the effect of the solidification path on the dispersion of the soft Sn particles was investigated by gravity die casting. It was found that immiscible alloys with the precipitation of the primary Al particles prior to the demixing reaction (such as Al-20Sn-10Cu) are much easier to obtain a fine and uniform dispersion compared with those alloys with a demixing reaction before the precipitation of the primary Al particles (such as Al-45Sn-10Cu).
  - Finally, the effect of shearing time, shearing speed of the MCAST process on the size and uniformity of the dispersed Sn phase were investigated. It was found that melt shearing at 200 rpm and 60 s is adequate to produce a fine and

uniform dispersion of the Sn phase, and that a higher shear rate and prolonged shearing time can only achieve minor further refinement.

- Growth of the minority Sn phase has been evaluated with different moulds providing different cooling rates. The liquid phases grew in different ways according to the processing conditions such as shearing, and cooling rate with different Sn concentrations.

Intensive shearing of Al-Si cast alloys

The morphology, defects and microstructural refinement of hypoeutectic and hypereutectic Al-Si cast alloys have been investigated under the dynamic intensive shearing condition at above the liquidus temperature and compared with those made using a conventional HPDC casting process. The following conclusions were obtained from the experimental results:

Hypoeutectic Al-Si alloy

- Intensive melt shearing provided significant grain refining of primary α-Al and uniform grain size over the entire casting specimen.
- Intensive shearing has improved the distribution of the α-Al(Mn,Fe)Si intermetallic phase with a narrow size distribution and their average size was reduced from 8 ± 4 μm to 5 ± 1 μm.
- Defect bands were observed to be present in both HPDC and MC-HPDC. However, intensive shearing distributes ESCs more uniformly, provides an ideal condition to nucleate primary α-Al with a spherical shape and significantly reduces the defect band size and porosity.
- The application of MC-HPDC is a useful way in combating the detrimental effect of foreign particles on mechanical properties and is expected to play a significant role in the recycling of Al alloys.

Hypereutectic Al-Si alloy

- The intensive shearing is observed to improve the sphericity and distribution of primary Si particles in the hypereutectic alloy and offered much improved tensile properties.

Chapter 8

Recommendation for further work

Rheomixing of Al-Sn-Cu immiscible alloys

- The rheomixing process of Al-Sn-Cu alloys can be further optimised with different amounts of alloying elements by using advanced computational thermodynamic techniques
- It would be useful to study the nucleation, growth, precipitation, coarsening process of the second phase of two promising alloys, Al-45Sn-10Cu and Al-20Sn-10Cu. These alloys can be processed by many different processing routes such as using different cooling rates, ultrasonic techniques etc and a useful comparative study made on the solidification and distribution of the Sn phase under different processing conditions.
- A combined study of experimental and fluid flow simulation would be useful to further the understanding of immiscible alloys solidification, drop migration and separation phenomena together with the relation of the shear stress with the drop /or particle formation in the final microstructure.
- Investigate the mechanical properties such as wear, fatigue, and corrosion for bearing materials and design special heat treatments to further enhance the mechanical properties.

Intensive shearing of Al-Si cast alloys

- Further experimental work needs to be carried out on more cast Al alloys to understand fully the experimental windows of the MCAST unit with different processing parameters.

- To understand fully the grain refining mechanism of alloys after the intense shearing of the liquid there is a need to developed further understandings of nucleation from experimental results (Crystallographic study by using transmission electron microscope (TEM)) with a theoretical understanding and computational simulation.

- MC-HPDC processed specimens exhibit a fine and uniform microstructure throughout the entire casting with minor defects. Based on these characteristics, it is anticipated that other mechanical properties such as fatigue, wear and corrosion resistance can be also studied.

References

A

Abramov V, Abramov O, Bulgakov V, Sommer F. (1998), Mater. Lett. 37: 27.

Abu-Dheir N, Khraisheh M, Saito K, Male A. (2005), Mater. Sci. Eng. A, 393A: 109.

Aluminum Association, (1987): Standard Test Procedure for Aluminum Alloy Grain Refiners: TP-1, (The Aluminium Association, Washington DC).

Apaydin N. (1982), J. Mater. Sci. Lett. 1: 39.

Ashok ST. and Rajan TV. (1996), Wear, 197: 105.

Auer S. and Frenkel D. (2001), Nature, London, 409: 1020.

Avalosse T, Rubin Y, Fondin L. (2000), Non-isothermal modelling of co-rotating and contra-rotating twin screw extruders Proc. ANTEC2000 Brookfield CT, vol 1, XLVI 19–23 (Orlando: USA, Society of Plastics Engineers).

B

Barlock JG, Mondolfo LF, Metallk Z. (1975), Mater. Sci. Eng. A, 66A: 605.

Bentley BJ. and Leal LG. (1986), J. Fluid Mechanics, 167: 241.

Biloni H. and Chalmers B. (1965), Trans. AIME, 233: 192.

Biloni H. and Chalmers B. (1968), J Mater. Sci., 3: 139.

Binder K. and Stauffer D. (1976), Adv. Phys. 25: 343.

Brechet Y, Embury JD, Tao S, Luo L. (1991), Acta Mater. 39: 1781.

Brown JR. (1999), Foseco Non-Ferrous Foundryman's Handbook, volume 11.

Burden MH. and Hunt JD. (1974), J. Cryst. Growth, 22: 109.

C

Campbell J. (1997), Castings, Butterworth-Heinemann, Oxford, 206.

Campbell J. (2003), "Castings", 2nd edition, Butterworth Heinemann, London

Campbell J. (2006), Mater. Sci. Tech. 22: 127.

Cao C, Lu X, Wei B. (1999), Adv. Space Res. 24: 1251.

Cao C, Wang N, Wei B. (2000), Science in China, Ser. A, 43: 1318.

Cao C, Wei B, Herlach D. (2002), J. Mater. Sci. Lett. 21: 341.

Cao CD, Herlach DM, Kolbe M, Görler GP, Wei B, (2003), Scripta Mater. 48: 5.

Cao P, Qian M, StJohnc DH. (2007), Scripta Mater. 56: 633.

Chalmers B. (1964), "Principles of solidification", John Wiley and Son, USA

Clift R, Grace JR, Weber ME. (1978). J. Fluid Mech. 6, 350.

Cook RF. (2006), J. Mater. Sci. 41: 841.

Crosley PB, Mondolfo LF. (1966). Mod. Cast. 49, 89.

Crossley FA. and Mondolfo LF. (1951), AIME Trans. 191: 1143.

Curiotto S, Pryds NH, Johnson E, Battezzati L. (2006), Metall. Mater. Trans. A, 37A: 23: 2361.

Curry DA. and Knott JF. (1979), Metar. Sci. 13: 341.

Curtis JT. and McIntosh RP. (1950), Ecology, 31: 434.

D

Dahle AK. and StJohn DH. (1999), Acta Mater. 47: 31.

Dahle AK, Lee YC, Nave MD, Schaffer PL, StJohn DH. (2001). J. Light Metals, 1: 61.

Dahle AK, Nogita K, Mcdonald SD, Dinnis C, Lu L. (2005), Mater. Sci. Eng. A, 413 414A: 243.

Dash M. and Makhlouf M. (2002), J. Light Metals. 2: 251.

Das A, Liu G, Fan Z. (2006), Mater. Sci. Eng. A, 419A: 349.

Das A and Kotadia HR. (2010), Mater. Chem.Phy. *in press*.

Davignon G, Serneels A, Verlinden B, Delaey L. (1996), Metall. Mater. Trans. A, 27A: 3357.

Davis JR, editor (1993). Aluminum and aluminum alloys. Ohio: ASM International.

Doehler H. (1910), ''Art of and Apparatus for Casting Fluid Metal,'' United States Patent 973, 483, United States Patent and Trademark Office, Washington, D.C., 25, October 1910.

Duwez P, Willens RH, Klement W. (1960). Continuous Series of Metastable Solid Solutions in Silver-Copper. J. Appl. Phys. 31: 1136.

E

Elliott R. (1984), "Eutectic solidification processing", Butterworths & Co., London, pp. 55-88, pp. 157-229.

Ershov GS. and Poznyak LA. (1985), " Microheterogeneity of metals and alloys (Rus.)", Metallurgy, Moscow, 1985, 214.

Eskin GI. (2001), Ultrasonic Sonochemistry, 8: 319.

F

Fan Z, Bevis MJ, Ji S, PCT Patent, WO 01/21343 A1, (1999).

Fan Z, Ji S, Zhang J. (2001), Mater. Sci. Tech. 17: 837.

Fan Z. (2002), Inter. Mater. Rev. 47, 49.

Fan Z, Wang Y, Xia M, Arumuganathar S. (2009a), Acta Mater. 57: 4891.

Fan Z, Wang Y, Zhang ZF, Xia M, Li HT, Xu J. et. al (2009b), Inter. J. Cast Met. Res. 22: 1.

Fang X. and Fan Z. (2006), Scripta Mater. 54: 789.

Fang X, Shao G, Liu YQ, Fan Z. (2007), Mater. Sci. Eng. A, 445–446A: 65.

Faraji M, Todd I, Jones H. (2005), J. Mater. Sci. 40:6363.

Fat-Halla N. (1987), J. Mater. Sci. 22: 1013.

Feng HK, Yu SR, Li YL, Gong LY. (2008), J. Mater. Processing Tech. 208: 330.

Flood SC. and Hunt JD. (1998), ASM Handbook, vol. 15, ASM, Materials Park.

Freti S, Bornand JD, and Buxmann K. (1982), Light Met. Age, 40:12-16.

G

Gall K, Yang N, Horstemeyer M, McDowell DL, Fan J. (2000), Fatigue Fract. Eng. Mater. Struct. 23: 159.

Gill R. (1997), "Modern analytical Geochemistry: An introduction to quantitative chemical analysis for earth, environmental and materials scientist, Wesley Longman Ltd. Harlow, England, 1997: 188.

Goodhew PJ, Humphreys FJ, Beanland R. (2001), "Electron microscopy and analysis", 3rd edition, Taylor and Francis.

Grosselle F, Timelli G, Bonollo F, Molina R. (2009) Metal. Sci. Tech. 27-2: 2.

Gourlay CM, Laukli HI, Dahle AK. (2004), Metall. Mater. Trans. A, 35, 2881.

Gourlay CM, Laukli HI, Dahle AK. (2007), Metall. Mater. Trans. A, 38A: 1833.

Green NR and Campbell J, (1993), Mater. Sci. Eng. A, 173: 261.

Greer AL, Bunn AM, Tronche A, Evans PV, Bristow DJ. (2000), Acta Mater. 48, 11: 2823.

Gupta AK, Saxena BK, Tiwari SN., Malhotra SL. (1992), J. Mate. Sci. 27: 853.

H

Hagiwara Y, Takashine Y, Tanaka M. (1997). Nuclear Engineering and Design,175: 49.

Hamilton DR. and Seidensticker RG. (1960), J. Appl. Phys. 31: 1165.

Harnby N, Edward MF, Nienow AW. (1985), "Mixing in the process industries", 2nd edition, Butterworths-Heinemann Ltd., Oxford.

He J, Zhao JZ, Ratke L. (2006). Acta Mater. 54, 1749.

Helenius R, Lohne O, Arnberg L, Laukli HI. (2005). Mater. Sci. Eng. A. 413-414A: 52.

Hernández FCR and Sokolowski JH. (2006), J. Alloys Comp. 426: 205.

Hutt J. and StJohn DH. (1998), Int. J. Cast Met. Res. 11: 13.

I

Ichikawa K. and Ishizuka S. (1987), Trans. Jpn. Inst. Met. 28: 145.

J

Ji S, Fan Z, Bevis MJ. (2001), Mater. Sci. Eng. A, 299A: 210.

Jian X, Xu H, Meek TT, Han Q. (2005), Mater. Lett. 59:190.

Jiang QC, Xu CL, Lu M, Wang HY (2005) Mater Lett. 59:624

Johnsson M, Bäckerud L, Sigworth G. (1993), Metall. Mater. Trans. A, 24A: 481.

K

Karnezis PA, Durrant G, Cantor B. (1998), Mater. Char. 40: 97.

Kim WT, Zhang DL, Cantor B. (1991), Mater. Sci. Eng. A, 134: 1133.

Kingsbury GR. (1992), "Friction and wear of sliding bearing materials", 10th edition. In: Olson D, editor. ASM handbook, vol. 18. Materials Park (OH): ASM International.

Kobayashi KF. and Hogan LM. (1985), J. Mater. Sci. 20: 1961.

Kocatepe K. and Burdett CF. (2000), J. Mater. Sci. 35: 3327.

Kohn A. and Philibert J. (1960), Mem. Sci. Rev. Met. 57: 291.

Kolbe M, Gao J. (2005), Mat. Sci. Eng. A, 413-414A, 509.

Kong CJ, Brown PD, Harris SJ, McCartney DG. (2005), Mater. Sci. Eng. A, 403A: 205.

Kotadia HR, Patel JB, Fan Z, Doernberg E, Schmid-Fetzer R. (2008), Solid State Phen. 141-143: 529.

Kotadia HR, Patel JB, Fan Z, Doernberg E, Schmid-Fetzer R. (2009a), Aluminium Alloys: Fabrication, Characterization and Applications II 2009, San Francisco, CA, 2009, W. Yin, S. K. Das, and Z. Long, ed., TMS, Warrendale, PA, 2009: 81-86.

Kotadia HR, Doernberg E, Patel JB., Fan Z, Schmid-Fetzer R. (2009), Metall. Mater. Trans. A, 40 (9): 2202.

Kotadia HR, Hari Babu N, Zhang H, Fan Z. (2010), Mater. Lett. 64 (6), 671.

Kuhn H. and Medlin D., ed. (2000), "Mechanical properties", ASM International, 8, Ohio.

Kurz W. and Fisher DJ. (1998), Fundamental of Solidification, Trans Tech, Zurich, Switzerland.

Kurzydlowski KJ. and Ralph B. (1995), "The quantitative description of the microstructures of materials", 1st edition, CRC Press, Florida.

Kyffin WJ, Rainforth WM, Jones H. (2001). J. Mater. Sci. 36: 2667.

L

Langbein D. ed. (1984), On the Separation of Alloys Exhibiting a Miscibility Gap. In: the Effect of Gravity on the Solidification of Immiscible Alloys. Proceedings of an RIT/ESA/SSC－Workshop, Jarva Krog, Sweden, Jan. 1984, ESA SP－219:3-8

Lappa M. (2004). "Fluids, Materials, and Microgravity-Numerical Techniques and insights into physics", Elsevier Ltd., Oxford.

Laukli HI, Graciotti A, Lohne O, Gjestland H, Sannes S. (2002), In 21st Die Casting Congr. & Tabletop Expo., NADCA, Rosemont, Ill., USA, T02-035.

Laukli HI. (2004). PhD. Thesis: High Pressure Die Casting of Aluminium and Magnesium Alloys- Grain Structure and Segregation Characteristics", Norwegian University of Science and Technology (NTNU), Norway.

Laukli HI, Gourlay CM, Dahle AK, Lohne O. (2005), Mater. Sci. Eng. A; 413-414A: 92.

Lee JC. (1984), The Formation of Liquid-Liquid Dispersion-Chemical and Engineering Aspects. Chameleon Press Ltd., London.

Lee FT, Major JF, Samuel FH. (1995), Fatigue Fract. Eng. Mater. Struct. 18, 385.

Lee YC, Dahle AK, StJohn DH. (2000), Metall. Mater. Trans. A, 31A, 2895.

Levich VG. (1962), "Physicochemical hydrodynamics", Englewood Cliffs (NJ), Prentice-Hall.

Li YW, Zhu XX, Xu ZT. (1998). Chinese Journal of Rare Metals. 22, 4: 305.

Liang D, Bayraktar Y, Jones H. (1995), Acta Metall. Mater. 43, 2, 579.

Lifshitz LM, Slyozov VV. (1961), J. Phys. Chem. Solids, 19, 35.

Lukas HL, Freis SG, Sundman B. (2007): Computational Thermodynamics-The Calphad Method, Cambridge University Press, Cambridge.

Loewenberg M., Hinch, EJ. (1996), J. fluid Mech. 321: 395.

Lu X, Kolbe M, Herlach D. (2003). Mat. Res. Soc. Symp. Proc. 754, 3.17.1–3.17.5.

M

Makhlouf MM. and Guthy HV. (2002), J. Light Metals, 1: 199.

Mason TG and Bibette J. (1997), Langmuir, 13,17: 4600.

Mason TG. (1999), Current option in colloid and interface science, 4: 231.

Maugis D. (1985), J. Mater. Sci. 20: 3041.

McDonald SD, Nogita K, Dahle AK. (2004), Acta Mater. 52, 4273.

Mirkovic D, Groebner J, Schmid-Fetzer R. (2008a), Mater. Sci. Eng. A, 487A: 456.

Mirkovic D, Groebner J, Schmid-Fetzer R. (2008b), Acta Mater. 56: 5214.

Mohan S, Agarwala V, Ray S. (1989a), Z. Metallkunde,79: 439.

Mohan S. (1989b), PhD. Thesis: Fabrication of Cast Al-Base Lead Bearing Alloys and their Wear Characteristics. University of Roorkee, Roorkee, India.

Mohan S, Agarwala V, Ray S. (1990), Wear. 140: 83.

Mohan S, Agarwala V, Ray S. (1991). Mater. Sci. Eng. A, 144A:215.

Mondolfo LF. (1976), "Aluminum Alloys: Structure and Properties", Butterworths, London.

Munitz A. and Abbaschian R. (1991), J. Mater. Sci. 26: 6458.

Munitz A. and Abbaschian R. (1996), Metall. Mater. Trans. A, 27A: 4049.

Murty BS, Kori SA, Chakraborty M. (2002), Inter. Mater. Rev. 47, 1: 3.

N

Nafisi S, Emadi D, Shehata MT, Ghomashchi R. (2006), Mater. Sci. Eng. A, 432A: 71.

P

PANDAT^{TM} - 7.0 (2000-2007) Software for Multiplecomponent Phase Diagram Calculation, Computherm LLC, 437 S. Yellowstone Dr., Suite 217, Madison, WI, 53719, USA.

Patel JB. (2005), "Semi-solid processing of aluminium alloys by Rheo-diecasting technology", Brunel University, West London, 2005.

Pathak JP, Tiwari SN, Malhotra SL, (1979), Metals. Tech. 6: 442.

Peng HX. and Fan Z. (2001), J. Mater. Sci. Lett., 20, 1769.

Polmear IJ. (1995), "Light alloys", 3rd edition, Butterworth-Heinemann, Oxford.

Prinz B. and Romero A. (1993), Immiscible liquid metals and organic (The proceeding of immiscible alloys, Physikzentrum, Bad Honnef 1992), DGM Informationsgesellschaft mbH by Ratke L. ed. 1993.

Pryds NH. and Huang X. (2000), Metall. Mater. Trans. A, 31A: 3155.

Q

Qian L, Toda H, Nishido S, Kobayashi T. (2006), Acta Mater. 54: 4881.

Quested TE. (2004a), Mater. Sci. Tech., 20: 1357.

Quested TE. (2004b), PhD. Thesis: Solidification of inoculated Aluminium alloys, Department of Material science and Engineering, University of Cambridge, Cambridge.

R

Ratke L. (Ed.) (1993), "Immiscible liquid metals and organic"(The proceeding of immiscible alloys, Physikzentrum, Bad Honnef 1992), DGM Informationsgesellschaft mbH. pp. 199-258, pp. 261-310.

Ratke L and Diefenbach S. (1995), Mater. Sci. Eng. R, 15R: 263.

Ratke L, Korekt G, Drees S. (1996), European Space Agency, ESOC: 247.

Rauwendaal C. (1994) "Polymer extrusion", 3rd edition, Hanser Publisher, New York.

Regel LL. (1989), Mater. Proc. Space. ed. R.Z. Sagdeev. Printed in the United State of America, 1, 67.

Robinson MB, Li D, Rathz TJ, Williams G. (1999), J. Mater. Sci. 34: 3747.

Rogers A. (1974), "Statistical analysis of spatial dispersion: The Quadrat method", 3rd edition, Pion, London.

S

Scardovelli R. and Zaleski S. (1999), Annu. Rev. Fluid Mech.31: 567.

Shamsuzzoha M. and Hogan LM. (1985), J. Crystal Growth, 72: 735.

Shima J, Leeb H, Haa HP, Choa YW, Yoonc E. (2001), J. Alloys Comp. 327: 270.

Siegel M. (1999), J. Appl. Math. 59: 1998.

Siggia ED. (1979), Phys. Rev. A, 20A: 595.

Singh M. and Kumar R. (1973), J. Mater. Sci. 8: 317.

Stefanescu DM. (1988a), "Casting", ASM Hand Book, volume 15.

Stefanescu DM, Dhindaw BK, Kacar SA, Moitra A. (1988b), Metall. Trans. A, 19A: 2847.

Stefanescu DM, Moitra A, Kacar AS, Dhindaw BK. (1990), Metall. Mater. Trans. A, 21A: 231.

Stone HA. (1994), Annu. Rev. Fluid Mech. 26: 65.

Street AC. (1986), "The Diecasting Book", 2nd edition, Portcullis Press Ltd., Surry, England.

T

Takahashi K, Weng J, Tien C. (1999), Micro. Thermo. Eng. 3:169.

Tanaka H. (1995), J. Chem. Phys. 103: 2361.

Tanaka H. (1996), J. Chem. Phys. 105: 1099.

Tang H. (2003a), PhD. Thesis: Numerical investigation of hydrodynamic behavior of immiscible alloys, Brunel University, West London, UK.

Tang H, Wrobel LC, Fan Z. (2003b), Model. Simul. Mater. Sci. Eng. 11: 771.

Tang H, Wrobel LC, Fan Z. (2004), Comp. Mater. Sci. 29: 103.

Tang H, Wrobel LC. (2005a), Inter. J. Eng. Sci. 43: 1234.

Tang H, Wrobel LC, Fan Z. (2005b), Appl. Phys. A, 81A: 549.

Tang H, Wrobel LC, Fan Z. (2006), Mater. Design, 27: 1065.

Taylor GI. (1932), Proc. R.Soc., London, Ser. A, 138: 41.

Taylor GI. (1934), Proc. R. Soc., London, Ser. A, 146: 501.

Tegze G, Pusztai T, Gr´an´asy L. (2005), Mater. Sci. Eng. A, 413–414A: 418.

Thiele WG. (1962), Aluminium (Ger), 38: 707-715, 780-786.

Tzimas E. and Zavaliangos A. (2000), J. Mater. Sci. 35, 21: 5319.

U

Uffelmann D, Ratke L, Feuerbacher B. (1996), European Space Agency, ESOC: 251.

Utracki LA and Shi ZH. (1992),: Polym. Eng. Sci. 32: 1824.

V

Vollmer M. and Weber A. (1925), Z. Phys. Chem., 119, 277.

W

Walter HU. (1986). Binary Systems with Miscibility Gap in the Liquid State. In "Materials Science in Space", Feuerbacher B, Hamacher H, Naumann RJ. eds., Sprinverlag Press, New York.

Wang L, Maklouf M, Apelian D. (1995), Int. Mater. Rev. 40: 221.

Wang H, StJohn DH, Davidson CJ, Couper MJ. (2000a), Aluminium Trans. 2: 57.

Wang H, Davidson CJ, StJohn DH. (2000b), Proceedings of Sixth International Conference on Semisolid Processing of Alloys and Composites, Edimet Spa, Brescia, Italy, 2000, pp. 149–154. Chiarmetta GL. and Rosseo M. eds.

Wang W, Bian X, Qin J, Syliusarenko SI. (2000c), Metall. Mater. Trans. A, 31A: 2163.

Wang N. and Wei B. (2003), Mater. Sci. Eng. A, 345A: 145.

Wagner C. (1961), Z. Electrochem. 65: 581.

Warren JA, Pusztai T, Kornyei L, Granasy L. (2009), Physical Review B. 79,014204.

Wei B, Herlach DM, Sommer F. (1993), Mater. Sci. Eng. A, 173: 355.

Weibull W. (1951), J. Appl. Mech. 18: 293-297.

Winkelman GB, Chen ZW, StJohn DH, Jahedi MZ. (2004), J. Mater. Sci. 39: 519.

Wu M, Ludwig A, Ratke L. (2003), Metall. Mater. Trans. A, 34A: 3009.

Wu M and Ludwing A. (2005), Mater. Sci. Eng. A, 413–414A: 192.

X

Xia K. and Tausig G. (1998), Mater. Sci. Eng. A, 246A: 1.

Xian X, Meek TT., Han Q. (2006), Scripta Mater. 54: 893.

Xu CL. and Jiang QC. (2006), Mater. Sci. Eng. A, 437A: 451.

Y

Yilmaz F. and Elliott R. (1989). J. Mater. Sci. 24: 2065.

Young NO, Goldstein JS, Block MJ. (1959), J. Fluid Mech. 6: 350.

Youssef YM, Dashwood RJ, Lee PD. (2005), Compos. Part A: Appl. Sci. Manuf. 36: 747.

Yuan L. (2001), PhD. Thesis: "Numerical simulation of the Liquid-Liquid phase separation and microstructure evolution of Al-In immiscible alloys during cooling", School of Materials Science and Engineering, Harbin Institute of Technology, Harbin, China

Yuan L, Yan-Xiang L, Jing-Jie G, Jun J, Yan-Qing S, Hong-Sheng D. (2002), Trans. Nonferrous Met. Soc. China, 12: 357.

Z

Zhang YC, Hao YY, Liu ZF,Chen GY. (1988), Mater. Sci. Eng. A, 98A: 381.

Zhou J. and Duszczyk J. (1990), J. Mater. Sci. 25: 4541.

Zhao JZ. and Ratke L. (2004). Scripta Mater. 50: 543.

Zhou X, Thompson GE, Skeldon P. (2008), Electrochimica Acta, 53: 5684.

Zuo M, Xiangfa L, Qianqian S. (2009), J. Mater. Sci. 44:1952.

Appendix I

Shear rate, $\dot{\gamma}$, is found in the gap between the tip of a screw flight and barrel surface, and is given by the following equation:

$$\dot{\gamma} = N\pi\left(\frac{D}{G} - 2\right) \tag{A1.1}$$

where N is the rotational speed of the screw, D is the outer diameter of the screw, and G is the gap between the screw flight and barrel surface.

rpm	$\dot{\gamma}$ (second^{-1})
1	1.77
10	17.79
100	177.93
200	355.86
300	533.8
400	711.73
500	889.66
600	1067.6
700	1245.53
800	1423.46
900	1601.4
1000	1779.33

Appendix II: Shrinkage Mould (Tatur Test)

Qualitative and quantitative measurements can be made to record the individual feeding characteristics of the test metal and to compare one alloy with another. This test is particularly good for comparing the effect of grain refinement, modification and gas content on porosity formation and distribution in a wide range of casting alloys. This information is taken from manual intruction by *N-TEC LIMITED*, England.

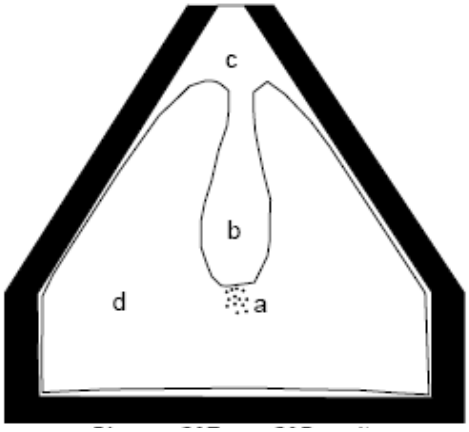

Diagram of cross section tatur test sample , three type of porosity, where a = volume of microshrinkage cavities; b = volume of macroshrinkage cavitation (pipe); c = volume of slumping and contraction; and d = actual casting volume.

t total volume of porosity = $a + b + c$ (A2.1)

Two further measurements are also required to fully evaluate the shrinkage of a Tatur test sample.

v volume of mould cavity (434ccs)

ρ absolute density of alloy

The test samples will show different amounts of porosity types a, b, and c depending on alloy composition; treatments such as modification, and the cleanliness of the metal.

Different metals will have different amounts of shrinkage when they transform from liquid to solid. Aluminium silicon casting alloys such as A356 would typically show ≈ 7% shrinkage while an Al-12%Si alloy would only have 3.5% shrinkage.

Volume of Pipe (*b*)

This is the first quantity to be measured. The measurement is made by carefully filling the pipe to the top of the sample with water, the volume of water added can be measured using either a measuring cylinder, or by the change in weight and assuming the density of water is 1 g/cc. This gives the volume *b*.

Volume of Microshrinkage Cavities (*a*)

This measurement requires an accurate measurement of the density of the solid Tatur test sample. First the weight of the sample in air is measured the then the weight with the sample suspended in water. The weight in water is less than the weight in air by the weight of the volume of water displaced. Water has a nominal density of 1 g/cc so the volume of the samples is the same as the difference between the weight in air and in water.

Weight of Sample In Air (W_{air})

The first measurement needed is the weight of the sample in air W_{air}. A typical aluminium Tatur test sample will weigh about ≈1100 grams. An electronic balance should be used that can give at least one decimal place of accuracy. The figure below shows a Tatur test sample being weighed, with a weight W_{air} of 1085.9 grams.

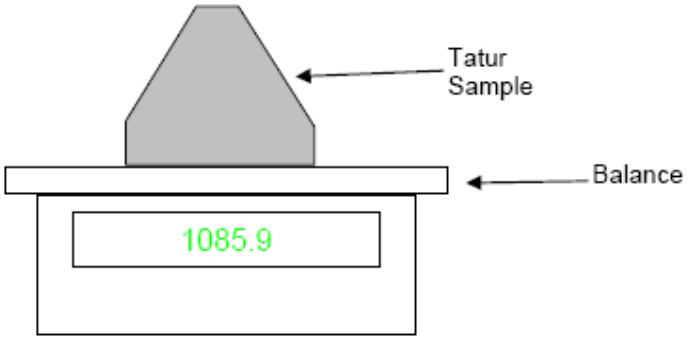

Sample weight in air (W_{air})

Weight of Sample In Water W_{water}

The second measurement required is of the weight of the sample suspended in water W_{water}, this is less than the weight in air by the weight of the volume of water displaced. The measurement technique will depend on the weighing balance available. The diagram

below shows a measurement in which the electronic balance allows weighing to be carried out by means of a rod extending below the balance. The sample is suspended from a cross piece attached to the rod extending from the balance, by means of a wire cradle. This cradle must be strong enough to support the sample but be lightweight and displace as small a volume as possible.

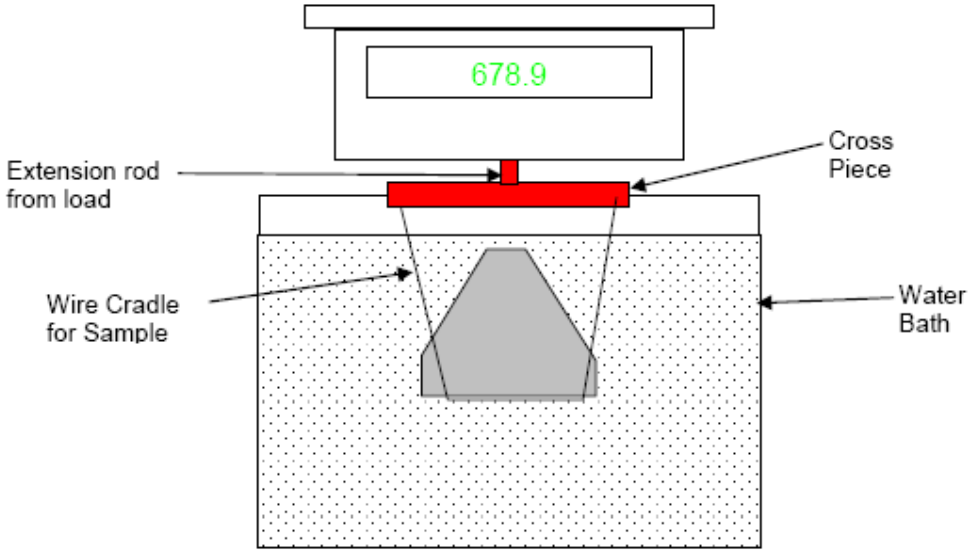

Sample being weighed in water (W_{water}), suspended below balance.

Whichever method is used the balance must first be tared with the wire cradle in place but with no sample present. This removes the buoyancy effect produced by the volume of water displaced by the wire and cradle. Went the balance has been tared the Tatur sample is carefully placed on the cradle and the weight taken. The weight may take a few seconds to stabilise, as putting the sample in place can cause ripples in the water bath which must be allowed to subside to produce a steady reading. Care must be taken that no air bubbles are trapped in the pipe of the test sample or attached to the outside of the sample. Any bubbles are removed by gently tapping the sample to release them. The volume of the water bath must be large enough so that the water level does not rise significantly when the Tatur sample is put into the bath. Increasing the water level will submerge more of the cradle and produce greater buoyancy uplift as more water is displaced. The weight measured when the sample is suspended in water might typically be 678.9 g. Assuming the density of water is 1 g/cc, the volume of casting(d), can be calculated as follows:

$$d = W_{air} - W_{water} = 1085.9 - 678 = 407\text{cc} \quad \text{(A2.2)}$$

The apparent density of the Tatur sample $\rho_{Apparent}$ is calculated as follows:

$$\rho_{\text{Apparent}} = \frac{W_{air}}{d} = \frac{1085.9}{407} = 2.66\ \text{g/cc} \quad \text{(A2.3)}$$

An accurate value of the actual density ρ_{Actual} is required to calculate a the volume of microshrinkage cavities. For Al-7.5Si type of alloy this is 2.685 g/cc.

The volume of metal in the Tatur test sample V_{Metal} is calculated from the weight of the sample in air and the actual density of the alloy:

$$V_{\text{metal}} = \frac{W_{air}}{\rho_{\text{Actual}}} = \frac{1085.9}{2.66} = 404.4\ \text{g/cc} \quad \text{(A2.4)}$$

The actual casting volume d has already been measured allowing the volume of microshrinkage cavities in the sample a to be calculated:

$$a = d - V_{Metal} = 407 - 404 = 3\ \text{cc} \quad \text{(A2.5)}$$

The volume of the mould cavity of the Tatur test *v*, is needed in order to calculate values of the porosity c and the total porosity *t*. The volume *v* will usually be supplied with the test mould, for the N-Tec mould this is between ≈ 400 to 500 cc. The Appendix contains details of how this may be measured if the value was not supplied. In the case given above the volume of the mould cavity was 434 cc.

The volume of slumping and contraction c can now be obtained by adding together a, V_{Metal} and *b* and subtracting the sum from the volume *v*:

$$c = v - (a - V_{Metal} + b) = 434 - (3 + 404 + 14.8) = 12.2\ \text{ccs} \quad \text{(A2.6)}$$

The total volume of shrinkage t is the sum of $a + b + c$ and from this the % shrinkage of the alloy can be calculated:

$$\%\ \text{Shrinkage} = \frac{(a+b+c)\times 100}{v} = \frac{(3+14.8+12.2)\times 100}{434} = 6.91\% \quad \text{(A2.7)}$$

Appendix III

The relationship between mean linear intercept and number of grains per unit volume (Greer 2000).

Throughout the present work, the grain diameter is quoted as the mean linear intercept $\bar{l}$. The fundamental quantity calculated by the model is the number of grains per unit volume of sample N_V. The relationship between N_V and $\bar{l}$ is not straightforward, and indeed depends on the grain-size distribution which has not been determined. An approximate relationship is derived, assuming an equiaxed grain structure with a grain-size distribution typical of a metal.

The grain shape is taken to be the tetrakaidecahedron. The size of a grain can be described by its calliper diameter *D*, defined as the mean perpendicular distance, averaged over all orientations, between two parallel tangent planes on the tetrakaidecahedron. It is assumed that the real grain structure has a range of values of *D*, *log-normally* distributed. The geometric-mean value $\overline{D_g}$ is then related to the mean linear intercept in this case by:

$$\overline{D_g} = 1.7756 \exp[-2.5(\ln \sigma)^2]\bar{l} \qquad \text{(A3.1)}$$

where $\ln \sigma$ is the standard deviation of the log-normal distribution. The grain-size distribution for a metallic microstructure undergoing grain growth is indeed log-normal, typically with $\ln \sigma = 0.23$. We assume, without specific justification, that such a distribution will also be a reasonable description for a refined, as-solidified grain structure. Substituting $\ln \sigma = 0.23$ in Eq. A3.1 gives:

$$\overline{D_g} = 1.558\bar{l} \qquad \text{(A3.2)}$$

The simple arithmetic mean D of a log-normal distribution is given by:

$$\overline{D} = \overline{D_g} \exp[0.5(\ln \sigma)^2] = 1.027\overline{D_g} \qquad \text{(A3.3)}$$

with the assumed value of ln σ. Furthermore, the volume-weighted arithmetic mean $\overline{D}_V$ is given by:

$$\overline{D}_V = \overline{D}\exp[(\ln\sigma)^2] = 1.054\overline{D} \tag{A3.4}$$

again taking ln σ = 0.23. Combining Eq. A3.2, A3.3 and A3.4, we have

$$\overline{D}_V = 1.686\bar{l} \tag{A3.5}$$

From the expression for the volume of a tetrakaidecahedron in terms of its calliper diameter, it follows that for a grain-size distribution described by $\overline{D}_V$, N_V the number of grains per unit volume is given by:

$$N_V = \frac{27}{8\sqrt{2}\overline{D}_V{}^3} = \frac{2.386}{\overline{D}_V{}^3} \tag{A3.6}$$

Substituting from Eq. A3.5 we obtain the relationship which is used throughout the present work:

$$N_V = \frac{0.5}{\bar{l}^3} \tag{A3.7}$$

Appendix IV

The Weibull distribution (Weibull 1951, Green and Campbell 1993)

To describe data that are skewed about their mean value, the Weibull distribution [3] is often used. This can be summarized in the two-parameter form as:

$$F_W = 1 - \exp\left[-\left(\frac{x}{\sigma}\right)^{\lambda}\right] \qquad \text{(A4.1)}$$

where, F_W is the fraction of specimens failed at or below a given value of x, e.g. a measured ultimate tensile strength (UTS), σ is a characteristic value of x at which 62.8% of the population of specimens have failed, and λ is the Weibull modulus. Rearranging the equation, it is possible to obtain the value λ from a plot of $\ln\{\ln[1/(1-F_W)]\}$ *vs.* $\ln(x)$. This produces a straight line plot of slope λ and intercept $-m/n(\sigma)$. The greater the value of λ, the narrower the range of the data.

The UTS data obtained from each casting method has been analysed using each of the statistical distributions described above and their 'goodness of fit' to each is described by the regression coefficient. Prior to plotting the data, each of the ranked positions of the UTS values of each sample of specimens (1 = worst) was converted to the failure probability of a population using the relation that, for the j^{th} item in the ranked data of a total number of specimens n_t, the probability of failure F is given by

$$F_j = \frac{j - 0.3}{n_i + 0.4} \qquad \text{(A4.2)}$$

The coefficients give the best fit for each of the distributions for all the castings.

Appendix V

Fracture strength

$$\sigma_f = \sqrt{\pi E \gamma_s / D} \quad \text{(A5.1)}$$

where γ_s is the specific surface energy, D is the diameter of the particle and E is Young's modulus. For Al, γ_s is 1.77 J/m^2 (Dash and Makhlouf 2002) and, E is 70 GPa (Dash and Makhlouf 2002), and for Si γ_s is 1.0 J/m^2 (Cook 2006), and E is 161 GPa (Cook 2006).

Phase	Processing temperature (°C)	Average Particle size (μm)		σ_f (MPa m$^{1/2}$)	
		HPDC	MC-HPDC	HPDC	MC-HPDC
α–Al(Al-9.5Si,LM24)	600	8.3	5.7	21.21	25.60
	615	8.3	5.4	21.21	26.30
	635	7.0	5.3	23.10	26.55
	650	7.5	5.4	22.32	26.30
α–Al(Al-10.3SiSilafont)	590	8.0	7.0	21.61	23.10
	600	7.5	6.2	22.32	24.54
	610	8.2	5.8	21.34	25.38
	620	7.9	5.3	21.74	26.55
	630	6.7	5.4	23.61	26.30
	640	6.8	5.2	23.44	26.80
	650	6.5	5.1	23.97	27.06
Primary Si(Al-14Si)	595	13.2	10.5	16.82	18.86
	600	12.7	12.6	17.15	17.22
	610	13.4	13.5	16.69	16.63
	620	15.3	12.2	15.62	17.50
	630	16.3	12.2	15.14	17.50
	640	16.0	12.1	15.28	17.57
	650	17.1	12.1	14.78	17.57